The Dissertation Committee for Hyun Woo Kim Certifies that this is the approved version of the following dissertation:

Structure and Properties of Amorphous Metallic Alloys: A First Principles Study

Committee:

_____

John G. Ekerdt, Supervisor

_____

Gyeong S. Hwang, Supervisor

_____

Charles B. Mullins

_____

Brian A. Korgel

_____

Sanjay K. Banerjee

Structure and Properties of Amorphous Metallic Alloys:

A First Principles Study

By

Hyun Woo Kim, B.S.; M.S. Ch. E

Dissertation

Presented to the Faculty of the Graduate School of

The University of Texas at Austin

in Partial Fulfillment

of the Requirements

for the Degree of

Doctor of Philosophy

The University of Texas at Austin

December 2010

Dedication

This dissertation is dedicated to my lovely family; my parents, Insub Kim and Minja Choi; my wife Leah and my daughter Min Ju Kim and son Minkyoon Daniel Kim.

Acknowledgements

I would foremost like to thank my advisors, Prof. John G. Ekerdt and Prof. Gyeong S. Hwang, whose support and passion have made the completion of this work possible. Dr. Ekerdt, through his leadership and modesty, has motivated and encouraged me through my thesis work. Dr. Hwang, through his enthusiastic passion for seeking new knowledge, has made my staying in UT very fruitful and enjoyable. I am truly grateful for their generosity in sharing their knowledge and insights with me. I would also like to acknowledge all of my colleagues who have aided me for completing my research. With their kind help, I could have accomplished my research. I am grateful to Hwang group people, Dr. Soohwan Lee, Dr. Sangheon Lee, Dr. Robert J. Bondi, Kyeong Eun Kwon, Eunsu Paek, Chia-Yun Chou, John A. Stephens, Hyung Chul Ham, and Youngjin Lee for their sharing their knowledge. I am thankful to Ekerdt group people, Dr. Jinhong Shin, Dr. Luke B. Henderson, Dr. Kelly M. Tom, Dr. Navneethakrishnan Salivati, Dr. Wyatt Winkenwerder, Dr. Ryan Fitzpatrick, Dr. Tuo Wang, Daniel Bost, Tyler Elko-Hansen for their helpful advices. I am thankful to people who visited our lab, shared their expertise and inspired me, Prof. Min Chan Kim, Prof. Do Young Yoon, and Prof. Tae Sik Cho. I would like to acknowledge Prof. Sang Jin Park for his helpful advices.

I am also especially thankful to Prof. Chang Kyun Choi for his permanent advice overall my life.

I would like to acknowledge my committee members that have guided me with their warm hearts and wonderful knowledge: Dr. Charles B. Mullins, Dr. Sanjay K. Banerjee, and Dr. Brian A. Korgel.

I am especially grateful to KCC presidents, Sang Young Chung, Mong Jin Chung, and Mong Ik Chung for their kind assistance overall my work. I would like to acknowledge to KCC vice president Won Ho Lee, KCC vice president Jung Gil Lee, KCC vice president Dae Yik Lee, Dr. Jong Oh Byun, Dr. Seung Yeop Choi, Mr. Myoung Ho Kim, Dr. Kyoung Hoon Kang, for their warmth advices. I would also like to thank Suk Jong Hyun, Jung Han Lee, Sung Ho Min, Yoon Bae Kim for their endurable interests.

I am especially thankful to my friend, Daniel Evans, whose advice always cheered me up whenever I struggled. I will never forget it.

I cannot thank enough to my parents, my sisters, parents in low, sisters in low, and brother in low. Their endless support and great love made me strong and confident.

Most of all, I thank my wife, Leah, whose deepest understanding, patience, motivation and love made this possible.

Structure and Properties of Amorphous Metallic Alloys:

A First Principles Study

Publication No._____

Hyun Woo Kim, Ph.D.
The University of Texas at Austin, 2010

Supervisors: John G. Ekerdt and Gyeong S. Hwang

Utilization of amorphous metallic alloy has received much attention for use in numerous microelectronic and electrochemical devices since they provide unique electrical, thermal conductivity, and magnetic properties. To develop these functional properties, it is essential to understand the amorphous structure and the property relationships. First principles calculations provide insight into the structure, thermodynamic stability, electronic and magnetic properties of amorphous alloys.

For Ru- and Co-based alloys, the thermodynamic stability was examined by calculating the mixing energy along with those of crystalline counterparts. The amorphous RuP, CoP, RuB, and CoB alloys, become energetically more favorable than their crystalline counterparts at moderate P(B) content. The atomistic structures have well-defined local structures depending on the atomic size ratio and electronic interactions between constituent elements. Their local ordering is attributed to strong p-d hybridization, which contributes to stabilizing the Ru(Co)-P(B) alloys. Surface segregation of P(B) and interfacial adhesion with copper were also studied.

Li-X (X: Si, Ge, and Sn) were examined when 1 or 2 Li atoms are inserted into the interstitial sites. Li insertion in the tetrahedral site, which is the most preferable site in the diamond matrix, causes outward displacement and charge localization around the X neighbors, thereby weakening of the covalent bonds leading to destabilization of the host matrix. We present the energetics, structure, electronic and mechanical properties of crystalline and amorphous Li-X (X: Si, Ge, Sn, and Si+Sn) alloys. Our calculations show that the incorporation of Li leads to disintegration of the tetrahedrally-bonded X network into small clusters of various shapes. Electronic structure analysis highlights that the charge transfer leads to weakening or breaking of X bonds with the growing splitting between s and p states, and consequently the Li-X alloys softens with increasing Li content.

Table of Contents

List of Tables

List of Figures

Chapter 1:
Introduction

1.1 Amorphous Alloy

An amorphous solid has a disordered atomic-scale structure. Generally, amorphous solids can be obtained during very rapid cooling from the liquid. However, there are several methods besides extremely rapid cooling (on the order of 10^6 K/s), including physical vapor deposition [1], solid-state reaction [2], ion irradiation [3], melt spinning [4], mechanical alloying [5], and electrochemically driven solid state amorphization [6]. The alloys contain atoms of significantly different sizes, leading to low free volume in the liquid state. It is possible to achieve formation of an amorphous structure even during slower cooling. In this case the alloy has to be made of three or more components, leading to complex crystal units with higher potential energy and a lower chance of formation. The first reported amorphous alloy was $Au_{75}Su_{25}$ produced by Klement et al. in 1960 [7]. Subsequent research has yielded multicomponent alloys based on lanthanum [8], magnesium [9], zirconium [10], palladium [11], iron [12], copper, and titanium, with critical cooling rates between 1 K/s to 100 K/s, comparable to oxide glasses. The best glass-forming alloys are based on zirconium and palladium, but alloys based on iron, titanium, copper, magnesium, and other metals are also known [13].

The disordered amorphous structure gives them unique properties, the most distinctive of which is the glass transition. A crystal will melt at a specific temperature when heated. A glass will not melt: instead, it gradually softens, changing from solid to liquid over a range of temperatures. This can be very useful for processing glasses into complex shapes. The material structure also results in low shrinkage during cooling and resistance to plastic deformation. The absence of grain boundaries leads to better resistance to wear and corrosion. Considerable interest in amorphous alloys also exists in many applications including: lightweight cars, aircraft turbine blades in corrosive environments, magnetic devices, and microelectronic devices.

1.2 The Formability of Amorphous Alloy

One important question about amorphous alloys is with what compositions do bulk alloys form. It has been known that heat of formation and atomic size difference are the key parameters for the formation of amorphous alloys [14].

The stability of an alloy material can be obtained by the optimization of the Gibbs free energy, $G(x,T)$, which allow for the calculation of the alloy's equilibrium properties for any concentration, x, and temperature, T. The determination of $G(x,T)$, however, is not an easy task: we have to deal with a many-body problem and therefore, approximations have to be made, which must be tested carefully with respect to their validity.

Generally, empirical and theoretical investigations are used to approach the phase stability, alloy formation, and geometric structure. The empirical model for predicting solid solution formation is the set of Hume-Rothery rules [15]. Hume-Rothery studied solid solutions of binary systems in the early 1930's and he proposed three factors controlling the extent of solid solubility, namely atomic size, electronegativity and the number of valence electrons of the two elements. Another semi-empirical approach to alloy formation is Miedema's atomic cell model [16]. He proposed an approach to calculating enthalpies in various binary systems for both the liquid and solid state. In the late 1980's, this approach was first used to predict the composition range in binary transition-metal amorphous alloys. In the 2000's, Inoue et al [17] suggested that the atomic radius of the components has to be significantly different (over 12%), to achieve high packing density and low free volume and the combination of components should have a negative heat of mixing, thereby inhibiting crystal nucleation. Schwarz and Johnson [18] first reported the amorphization by interdiffusion between crystalline metallic layers in the La-Au system and claimed that a large negative mixing energy and a large size difference between the constituent metals are necessary for solid-state amorphization (SSA).

Theoretical investigations based on quantum mechanics are very useful in understanding material properties. Specifically, DFT (density function theory)

calculations, which are called ‘first principles calculations’ in the sense that no empirical parameters are necessary for a given crystalline lattice, are the most accurate and efficient techniques for describing atomic energies and configurations. One application of these is to supplement phase diagram information, by energetics of the both stable and metastable phases [19, 20]. This is particularly useful for ternary systems where experimental information is limited. This has also been used to study local structures and dynamics in liquid metals and alloys [21, 22].

In order to solve problems connected to alloy formation, phase stability and geometric structure, we will employ i) the formation energy (or mixing energy) for evaluating the formability of an amorphous alloy, ii) Voronoi tessellation method and pair distribution function for analyzing the short and medium range ordering in an amorphous structure, and iii) the empirical model, for instance, the Egami’s model [23], which correlates the minimum concentration required to make a disordered structure with atomic volume ratio in a binary system.

In addition, dynamic properties are also predicted by an *ab initio* MD simulation, and where possible, experimental results are also presented for comparison to verify my results.

Quantum-mechanical approaches based on density functional theory (DFT) not only allow us to establish a realistic description of an amorphous structure, but also to develop a detailed understanding of the origin of short and medium range order often seen in amorphous alloy structures.

In this research, DFT calculations are utilized to understand the formability of an amorphous alloy, phase stability, and structural properties for amorphous alloys in the fields of metal barriers [24-29] and the anode in the lithium ion battery (LIB) [6] along with experimental comparisons.

1.3 Applications of amorphous alloys

1.3.1 Meal barrier or seed layer in microelectronic devices

The amorphous Ru- and Co-based alloys can be used as a metal barrier or seed layer in microelectronic devices. Ruthenium has been considered for a number of microelectronic applications including serving as a Cu diffusion barrier and Cu seed layer due to its low resistivity (~7 μΩ cm), chemical stability, and low solubility with Cu [24]. However, thin Ru films are polycrystalline and are structured with columns, which impose limitations on their use as a copper diffusion barrier. Fast copper diffusion occurs more frequently through grain boundaries than in the bulk [25]. To improve barrier properties, controlling the microstructure of the Ru film is essential: changing it from polycrystalline or columnar to amorphous by employing chemical alloying elements such as P and B in the CVD process [25, 26]. Phosphorus plays an important role in creating an amorphous RuP film. It was observed that films containing ~17% of P remain amorphous upon annealing to 635 K. It has also been shown that 5 nm thick amorphous RuP films function as Cu diffusion barriers [26]. First principles calculations can provide many valuable insights into the bulk structural and electronic properties of RuP alloys as well as interfacial interactions between the RuP alloy and the substrate (SiO_2), and the RuP alloy and copper.

In addition, as another barrier material, cobalt-based alloy are considered as an excellent Cu diffusion barrier due to its insolubility with Cu and low resistivity (~6 μΩ cm). Although cobalt or cobalt alloys such as Co-Mo and Co-P are capable to use as a copper diffusion barrier [26-28], structural and electronic properties of the Co alloys have not been investigated.

The overall objective of this work is to develop a quantitatively understanding of the microstructure of metal alloys: that is, how the metal alloys are stabilized in the alloy system, and how the local structures affect the alloy formability.

In addition to the bulk alloys properties, the interface chemistry will be presented and show how the interface chemistry affects adhesion between Ru(P)-Cu and Ru(P)- *a*-SiO_2.

1.3.2 Li-X (X: Si, Ge, Sn) anode materials in Lithium ion battery.

The second research focus is on the semiconductor based anode material in the lithium ion battery (LIB). This is because the formation of amorphous materials by an electrochemically-driven solid-state amorphization (SSA) reaction can be observed at the anode side [6].

Silicon-based materials have recently emerged as a promising candidate for anodes in lithium-ion batteries because they exhibit a higher energy-storage capacity than the conventional graphite anode. Silicon (Si) has a theoretical lithium (Li) capacity of $Li_{4.4}Si \approx 4200$ mAh/g, which is more than ten times greater than that of graphite (372 mAh/g) [29-31]. Moreover, Si is safer, less expensive, and far more abundant than graphite. However, the practical use of Si as an anode material is hampered by its low intrinsic electrical conductivity and poor cycling performance [32-35] In particular, the volume changes up to 400% during lithiation and delithiation can cause severe cracking and pulverization of the Si electrode, and consequent capacity fading arising from the loss of electrical contacts. Considerable efforts have been made to overcome these problems, for instance, through structural modifications, such as amorphous phases [36, 37], nanoparticles [38, 39], nanowires [40] and alloying with active/inactive elements, such as silicon-tin [41] and silicon-metal [42-46] composites. In addition, first principles calculations have recently been applied to investigate fundamental aspects of the structural changes and lithiation behavior of Si-based materials, yet many still remain unclear.

Recent studies [47-52] have provided evidence for the formation of various stable lithium silicide crystalline phases, such as, $Li_{12}Si_7$, Li_7Si_3, $Li_{13}Si_4$, $Li_{15}Si_4$ and $Li_{22}Si_5$ during high-temperature lithiation. However, room-temperature Si lithiation frequently leads to amorphous lithium silicides (*a*-Li-Si) [6]. It is therefore necessary to better understand the nature of amorphous Li-Si alloys, with comparisons to their crystalline counterparts. Very recently some theoretical efforts have been undertaken to understand the structure and properties of amorphous lithium silicides [53, 54]. Nonetheless, our

understanding regarding the nature and properties of Li-Si alloys as well as Ge-Li, Sn-Li, and Si-Sn-Li alloys is still limited.

The objective of this work is to develop a quantitatively understanding of the microstructure of Li-Si (Ge, Sn) alloys: that is, how the Li atoms behave in the diamond host matrix and how the local structures affect the electrochemical performance. The fundamental findings assist in understanding the nature of Li-Si (Ge, Sn) alloys further, and the present work can also provide a framework for the study of various lithiated alloys.

1.4 Objective and Outline

This work develops a fundamental understanding of amorphous alloys using first principles density functional theory calculations. In investing the amorphous alloy properties, first principles calculations have proven to be quite successful.

Ruthenium (Ru) has been considered as an effective metal barrier and seed layer in the copper (Cu)-based interconnect, and silicon-based materials have recently emerged as a promising candidate for anodes in lithium-ion batteries (LIB). The objectives of this research are: i) to present a detailed atomic-level understanding of how Ru- and Co-based amorphous alloys are stabilized depending on the atomic size ratio between two constituents and different chemistry of the alloying component (here phosphorus (P)/boron (B) in Ru (and Co); and, ii) to elucidate the structural and electronic properties of Si(Ge, Sn)-based Li alloys depending on the Li content.

In the first part of this dissertation, the influence of P or B, which differ in atomic size and chemistry, on the amorphous phase stability is investigated. Different atomic size ratio and chemistry lead to different types of short-range order as well as the nature of the medium-range order. To gain an understanding of the nature, forming ability and properties of amorphous Ru-P and Ru-B alloys, research focused on geometric and electronic structure analysis. The amorphous Ru-based alloy structure is thought to be mediated by substituting P and B alloying components with different atomic size. The total energy difference between a pseudo-crystalline and an amorphous alloy is used to

explore a series of open questions as to how amount of P or B are required to create an amorphous structure. The mixing enthalpy is regarded as an indicator of alloy stability; hence, the stability and forming ability of an amorphous alloy can be evaluated by the mixing enthalpies of both crystalline compounds and amorphous alloys at a selected composition of P or B atoms. The Voronoi tessellation method [55, 56] and pair distribution functions (PDF) are used to elucidate the short-to medium range details and local nearest-neighbor coordination. Density of state (DOS) is also used to understand the electronic properties of different amorphous alloys with P or B.

Furthermore, the surface and interface property prediction of amorphous alloys will be covered as well. The surface segregation behavior at the *a*-Ru-P and *a*-Ru-B surfaces is investigated using *ab initio* molecular dynamics simulations within density functional theory. In this research, atomistic details of the segregation by elements (P and B) are explored.

The interfacial interaction between RuP and Cu, by calculating the adhesion energy (the ideal work of separation) is also studied. Chemically different elements (P or B) influence the adhesive interaction at the interface between alloy and Cu layer. This is addressed by investigating the adhesion energy between interfacial layers and electronic properties around the interface.

In the second part of this dissertation, the influence of Li content on the amorphous phase's stability is investigated in terms of thermodynamic and kinetic points of view. The silicon matrix is easily destroyed by Li insertion. Over a limited composition and film thickness Si can remain amorphous during lithiation/delithiation. While experiments have made much progress in understanding the behavior of Li in Si(Ge, Sn), a detailed understanding of how Li interacts with Si(Ge, Sn) is lacking. This work, therefore, provides detailed understanding of the phenomena. In addition, compared with binary alloys; which are prone to form intermetallic compounds, a ternary system reduces this chance, and in turn stabilizes an amorphous structure. This is also addressed by investigating the atomic-level structure and properties for ternary systems including Si and Sn in the Si-Sn-Li alloy system.

This dissertation is organized as follows:

In chapter 2, I present the basis for density functional theory (DFT) and various techniques we used within DFT for extracting the fundamental data we need.

In chapter 3, I present the structure and electronic properties for the bulk Ru-P, Ru-B alloys.

In chapter 4, the surface segregation of P and B on the Ru-P and Ru-B alloy surfaces, respectively, is presented.

In chapter 5, the interface interaction between RuP-Cu will be presented.

In chapter 6, the interface interaction between Ru-*a*-SiO_2 will be presented.

In chapter 7, I present the structural and electronic properties for the CoP and CoB bulk alloys with the same scheme as Ru-P (Ru-B) alloys.

In chapter 8, the nature of 1 or 2 Li in Si is explored.

In chapter 9, the structure and properties of Li-Si alloys is presented.

In chapter 10, I present the structure and properties of Li-Si, Li-Ge, and Li-Sn alloys.

In chapter 11, I present the structure and properties for ternary *a*-Li-Si-Sn alloys.

In chapter 12, I summarize the contributions of this thesis on furthering an understanding of the structure and chemistry of amorphous metallic alloys.

Chapter 2:
Theoretical Background

2.1 Introduction to Density Functional Theory

For the past 40 years density functional theory (DFT) has been widely used for energy, structures, and properties of many solid-state and molecular systems. The theoretical focus of DFT is the electron density, ρ, rather than the wavefunction, ψ; the Hohenberg-Kohn [57] theorem states that the ground-state properties of a substance are uniquely determined by the electron density and the ground-state energy is a functional of the electron density. The ground-state energy of an n-electron molecule is represented as

$$E(\rho) = E_K + E_{P;e,N} + E_{P;e,e} + E_{XC}[\rho] \qquad (2\text{-}1)$$

where E_K is the total electron kinetic energy, $E_{p;e,N}$ the electron-nucleus potential energy, $E_{p;e,e}$ the electron-electron potential energy, and $E_{XC}[\rho]$ the exchange-correlation energy, which takes into account all the effects due to spin. The orbital used to construct the electron density from

$$\rho(r) = \sum_{i=1}^{n} |\psi_i(r)|^2 \qquad (2\text{-}2)$$

is calculated from the Kohn-Sham equations [58], which is defined as

$$[-\frac{\hbar^2}{2m_e}\nabla_1^2 - \sum_{j=1}^{N}\frac{Z_j e^2}{4\pi\varepsilon_0 r_{j1}} + \int\frac{\rho(r_2)e^2}{4\pi\varepsilon_0 r_{12}} + V_{XC}(r_1)]\psi_i(r_1) = \varepsilon_i\psi_i(r_1) \qquad (2\text{-}3)$$

where first term in the Hamiltonian operator is the kinetic energy, the second term is the electron-nucleus attraction, the third term is the electron-electron repulsion, and the fourth term is the exchange-correlation potential, which is defined as

$$V_{XC}[\rho] = \frac{\delta E_{XC}[\rho]}{\delta\rho} \qquad (2\text{-}4)$$

Thus Kohn-Sham equations are solved iteratively and self-consistently: first, guessing the electron density; second, calculating the exchange-correlation potential by assuming an approximate form of the dependence of the exchange-correlation energy on the electron density, and next, solving the Kohn-Sham equations to obtain an initial set of

orbitals. This set of orbitals is used to obtain a better approximation to the electron density in Equation (2-2) and the process is repeated until the density and the exchange-correlation energy are constant to within some tolerance.

There are general forms to obtain the $E_{XC}[\rho]$: first, the local density approximation (LDA), which is given by

$$E_{XC}[\rho] = \int \rho(r)\varepsilon_{XC}[\rho(r)]dr \qquad (2\text{-}5)$$

where $\varepsilon_{XC}[\rho(r)]$ is the exchange-correlation energy per electron for a uniform electron gas of density of ρ: the electron energy at each point in the system is the same as that of a uniform gas of the same density [59]

The exchange correlation potential is then given by

$$V_{XC}^{LDA}[\rho] = \frac{\partial E_{XC}^{LDA}[\rho]}{\partial \rho} = \varepsilon_{XC}(\rho) + \rho(r)\frac{\partial \varepsilon_{XC}(\rho)}{\partial \rho} \qquad (2\text{-}6)$$

It is common to split ε_{XC} into exchange and correlation potentials,

$$\varepsilon_{XC} = \varepsilon_x(\rho) + \varepsilon_c(\rho) \qquad (2\text{-}7)$$

The exchange potential is given by the Dirac functional:

$$\varepsilon_X[\rho] = -\frac{3}{4}\left(\frac{3}{\pi}\right)^{\frac{1}{3}}\rho(r) \qquad (2\text{-}8)$$

The value of $\varepsilon_C(\rho)$ has been determined by Quantum Monte Carlo calculations [60].

Second, the generalized gradient approximation (GGA) suggested by Purdue and Yue [61, 62], which is given by

$$E_{XC}[\rho] = \int \rho(r)\varepsilon_{XC}[\rho(r), \nabla\rho(r)]dr \qquad (2\text{-}9)$$

This leads to an energy functional that depends on both the density and its gradient. The Kohn-Sham equations have the same structure as the Hartree-Fock equations with the non-local exchange potential replaced by the local exchange-correlation potential $V_{XC.}$

In comparison with LDA, GGA method tends to improve the total energies, structural difference, and energy barriers [63].

2.2 Pseudopotential and the projector augmented-wave method

Density functional theory calculation employs a plane-wave basis set and the pseudopotential (PP) approximation. Physical properties of solids are strongly correlated with the valence electrons to a greater degree than that of the tightly bound core electrons. The most common pseudopotentials used in DFT are the ultrasoft pseudopotential (US-PP) introduced by Vanderbilt [64]. Vanderbilt's pseudopotential approximation is now adapted quite widely and especially for the 3d transition-metals saving in computation time, and improvements in the accuracy can be significant. But the success of the method is partly hampered by the rather difficult construction of the pseudopotentials, i.e., too many parameters (several cutoff radii) must be chosen and therefore tests are required in order to obtain an accurate and highly transferable PP. To overcome these disadvantages, Blöchl has further developed the US-PP concept by combining ideas from pseudopotential and linearized augmented-plane-wave methods (LAPW) into the projector augmented-wave (PAW) method [65].

Blöchl introduced a linear transformation from the pseudo soft (PS) to the all electron (AE) wave function and derived the PAW total energy functional in a consistent manner applying this transformation to the PS functional. The construction of PAW datasets is easier because the pseudization of the augmentation charges is avoided, i.e., the PAW method works directly with the full AE wave functions and AE potentials. Therefore the PAW method has two main advantages: a) it is possible to obtain the true "all electron" wavefunction, b) the convergence is comparable to an ultrapseudopotential one.

For reference, the all electron eigenvalues of an atom is determined using the Schrödinger equation, as is given by

$$(-\frac{\hbar^2}{2m}\nabla^2 + V)\Psi_{AEl} = C_l \Psi_{AEl} \quad (2\text{-}10)$$

where Ψ_{AEl} is the wavefunction for the all-electron system with angular component *l*. The resulting valence eigenvalues are substituted back into the Schrödinger equation, but with a parameterized pseudowavefunction of the form:

$$\Psi_{psi} = \sum i = 1^{n} \alpha_i j_l \qquad (2\text{-}11)$$

where j_l are spherical Bessel functions.

In my work, first principles calculations are performed based on (spin polarized, if necessary) DFT within the generalized gradient approximation (GGA), as implemented in VASP (Vienna *Ab initio* Simulation Package, ver. 4.62) [21, 66, 67]. Vanderbilt type US-PPs or PAW method is used in different system

2.3 *Ab initio* molecular dynamic simulation

A major breakthrough for the realistic sumulation of materials using electronic structure calculations was achieved by Car and Parrinello [68] A possible strategy for combining electronic structure with molecular dynamics is the following: for a given set of initial nuclear positions $R_{1,}...,R_N$, minimize the energy functional to obtain the ground state density $n_0(r)$ and corresponding orbitals $\psi_1^{(0)}(r),...,\psi_n^{(0)}(r)$. Given these quantities, the forces between the nuclei are given by the Hellman-Feynman theorem:

$$F_J = -\frac{\partial}{\partial R_J} E[\{\psi^{(0)}\}],\{R\}] \qquad (2\text{-}12)$$

The forces are then fed into a numerical integration procedure together with a set of initial velocities for the nuclei, and a step of molecular dynamics (MD) is carried out, yielding a new set of positions and velocities. At the new nuclear positions, the energy functional is minimized again and a new set of forces is obtained and used to perform

another step of MD propagation. This procedure is repeated until an entire trajectory has been generated.

This dynamical procedure is constructed in such a way that if the orbitals are initially chosen corresponding to the ground state density at the initial nuclear configuration, they will remain approximately in the ground state as the nuclear configuration evolves in time. In the original formulation of the Car-Parrinello scheme, the orbitals are expanded in a plane wave basis,

$$\psi_i(r) = \sum_g c_g^i e^{ig \bullet r} \qquad (2\text{-}13)$$

where c_g^i are the expansion coefficients. (This form of the plane wave expansion is actually a special case of a more general plane-wave expansion, in which the orbitals are assumed to be Blöchl functions, $\psi_{i,k}(r)$. Here, the choice $k = (0,0,0)$, the so called *gamma point* has been made.) The fictitious adiabatic dynamics is then formulated for the coefficients by introducing a set of velocities $v_{cg}^i = c_g^{-i}$ and an associated mass parameter u (having units of energy × (time)^2).

Further development of *ab initio* total energy algorithms allowed efficient simulations using *ab initio* molecular dynamics on the Born-Oppenheimer surface. Here, for each time step first the electronic ground state is determined and atomic forces are calculated, then the Newtonian equations of motion are solved [69].

In my research, the Nose-Hoover thermostat (NVT) for constant temperature and velocity rescaling method in the molecular dynamics simulations are performed to investigate the atomic rearrangement and kinetic properties. For all *ab initio* molecular dynamic (AIMD) calculations, the NVT ensemble is used.

2.4 Nudged elastic band method

To find the transition (saddle point) pathway, the nudged elastic band method (NEBM) [70-72] is widely used. In order to implement NEBM we first determined the final and initial state of the system and determined the eight configurations between the final and initial states. Once all configurations are determined, the path is then optimized by moving the atom within the respective image so as to minimize the forces. However, each image is under the constraint that the images are only allowed to move orthogonal to the moving pathway. The images are kept on a smooth continuous pathway by adding a spring force, which attracts neighboring images to each other, and the minimum energy pathway is determined. A recent improved NEBM called climbing NEBM results in improved convergence to the true saddle point by allowing the highest energy images to be exposed to the total true force. For the analysis of the Li mobility in the Li-Si alloy system the climbing NEBM method is used.

2.5 Output from the calculations

2.5.1 Lattice parameter, bulk modulus, and the cohesive energy

The lattice constant is usually determined by calculating the total energy of the bulk system at several values of the lattice constant and performing a fit to the resulting points by using the Murnaghan equation [73], which yields a bulk modulus. In our calculations, uniform tensile and compressive stresses were normally imposed on the alloys to achieve ±10 % volume variation.

$$E(V) = E_0 + (\frac{BV}{B^{'}})[\frac{(V_0/V)^{B^{'}}}{(B^{'}-1)} + 1] - \frac{V_0 B}{(B^{'}-1)} \qquad (2\text{-}14)$$

where E and E_o refer to the total energies of a given system at volume V and V_o (equilibrium), respectively, B is the bulk modulus, and B' is the pressure derivative of the bulk modulus.

2.5.2 Formation energy (mixing energy)

The formation energy (or the enthalpy of mixing) is regarded as an indicator of an alloy stability; hence, the stability of an amorphous alloy can be described by calculating the formation enthalpy given by:

$$\Delta E_f = \frac{1}{(m+n)}[E(A_m B_m) - mE_A - nE_B] \quad (2\text{-}15)$$

where $E(A_mB_n)$ is the total energy per atom of the alloy examined, x is the number fraction of B in the alloy, and E_A and E_B are the total energies per atom of pure A and B atoms, respectively. It is defined as the energy gain or loss per atom with respect to the bulk constituents at their equilibrium lattice constants. A sign of positive ΔE_f stands for phase separation, while a negative sign of ΔE_f means ordering or mixing. The formation energy concept also holds for random alloy structure. Then, ΔE_{mix} is called the mixing enthalpy per atom and is given by

$$\Delta E_{mix} = \frac{1}{N}[E(A_{1-x}B_x) - (1-x)E_A - xE_B] \quad (2\text{-}16)$$

with N being the total number of atoms in the disordered alloy.

2.5.3 Density of States

The density of states (DOS) describes how many electronic states are located inside an infinitesimally small region dE around a given energy E. The local density of states (LDOS) also can provide useful information for determining the properties of the bonding mechanism between the host and guest atoms or solute and solvent atoms in the alloy system. From the analysis of the LDOS decomposed at each atom and the angular momentum channels l,m are presented.

2.5.4 Charge density

DFT calculations provide the ground state charge density in a system, where charge distribution describes if the electrons are evenly distributed as in a metal system,

or highly concentrated around anionic species as in ionic system. Even more interesting is the charge density difference between charge densities of two species. The charge density difference ($\Delta\rho$) is calculated by subtracting the charge densities of A atoms and the B atoms from the total charge density of the A-B atoms with no atomic displacement for the binary system, i.e., $\Delta\rho = \rho(\text{A/B}) - \rho(\text{A}) - \rho(\text{B})$. This charge density difference can be used to understand the bonding mechanism and charge transfer.

2.5.5 Mean square displacement

Mean square displacement (MSD) of atoms can be computed by its definition

$$MSD = <| R(t) - R(0) |^2> \qquad (2\text{-}17)$$

where <...> denotes the average over all the atoms, and $R(t)$ is the atomic position at time t. The MSD contains information on the atomic diffusivity. If the system is solid, MDS saturates to a finite value, while if the system is liquid, MSD grows linearly proportional to time. The self-diffusion constant (D) of an atom is calculated based on the Einstein relation:

$$D = \frac{<| R(t) - R(0) |^2>}{6t} \qquad (2\text{-}18)$$

Chapter 3:

First principles investigations of bulk properties of amorphous Ru-P (ruthenium-phosphorus) and Ru-B (ruthenium-boron) alloys.

3.1 Introduction

Metallic glasses have been studied extensively because of their scientific interest and technological importance. Unlike a well defined crystalline structure, the atomic short and medium range order in amorphous alloys remains unclear. For instance, a metal-metalloid glass, in which the chemical short-range order is strong, is not well defined by Bernal's dense random packing of hard spheres [74]. The forming ability of amorphous alloy is strongly related to the short and medium range ordering, which is governed by the atomic size ratio and different chemistry. The details of how the atoms are packed in amorphous alloys and how the short and medium range ordering are related to the forming ability of amorphous alloys are far less understood.

Ruthenium has been considered as an effective metal barrier and seed layer in Cu-based interconnects [24]. To improve barrier properties, controlling the microstructure of the Ru film is essential: changing it from polycrystalline or columnar to amorphous by employing a chemical alloying element, phosphorus (P), in the CVD process [25, 26]. Phosphorus plays an important role in creating an amorphous RuP film. Films containing ~17% of P are observed to remain amorphous upon annealing to 635 K. It has also been shown that 5 nm thick amorphous RuP films function as Cu diffusion barriers [26]. *Ab initio* molecular dynamics calculations [25] showed that Ru-P alloy with 20% P can result in an amorphous structure exhibiting the topological and strong short-range order. To investigate the structure and stability of the amorphous Ru-P alloy, we first develop the amorphous Ru-P alloy models with varying P content. Then, we analyze the short range order as well as medium range order and calculate the energetic and chemical bonding properties.

Generally, the atomic size ratio and negative formation energy are considered to be the main parameters to promote the properties of amorphous alloys. To gain

quantitative understanding on the effects of the atomic size ratio (λ) and different chemistry on the forming ability of amorphous alloys we employed boron (B), which is different in atomic size and chemistry with P, in creating amorphous Ru alloy as an alternative to *a*-Ru-P alloys. In a different environment, we will elucidate how the short and medium range order affect the forming ability and alloy properties.

In this chapter, we use well established methods based on first principles density-functional theory calculation to predict the 3D amorphous alloy structures and bonding properties of Ru-P and Ru-B alloys. In particular, we examine different types of short range order as well as the nature of the medium range order found in $Ru_{80}P_{20}$ and $Ru_{87}B_{13}$ alloys.

Analyzing the details of the structure changes in the different alloy system, we find that icosahedra dominate the medium range ordering in both systems, while the short range ordering is primarily governed by the atomic size ratio. Overall comparison of our results with previous experimental modeling [75] and available theoretical studies [76] shows reasonable agreement for our models. Our findings provide realistic characterization of glassy structures but also a detail understanding of the origin of short and medium-range ordering of amorphous alloys.

3.2 Method

All atomic structures and properties reported herein were calculated using the plane-wave-basis pseudopotential method with the generalized gradient approximation (GGA) [63] to density functional theory (DFT) [57] using the well established Vienna *ab initio* Simulation Package (VASP) [21]. A plane-wave basis set for valence electron states and Vanderbilt ultrasoft pseudopotentials for core-electron interactions were employed. A plane-wave cutoff energy of 300 eV is used and the Brillouin zone integration was performed using one k-point (at Gamma) for the molecular dynamical simulation and 2×2×2 k-points for the geometric optimization step. For the construction of model alloys, Ru-P and Ru-B structures used in our analysis, we begin by randomizing 72-Ru atoms in a periodic supercell and then replace a given fraction of Ru with P or B.

Next, the alloy was melted at high temperature (3500 K) for 3 picoseconds (ps) with a time step of 1 femtosecond (fs), using *ab initio* molecular dynamic simulation (AIMD) within a Born-Oppenheimer frame work, and then quenched to 500 K at a rate of 1.5 K/fs, followed by static structural optimization. Here the temperature was controlled using velocity rescaling. The structures of crystalline Ru-P and Ru-B, as well as ruthenium, phosphorus and boron, are summarized in Table 3.1.

For further structural and electronic property analysis, the $Ru_{80}P_{20}$ and $Ru_{87}B_{13}$ alloy structures were modeled using 144-atoms (consisting of 115 Ru and 29 P atoms in $Ru_{80}P_{20}$, 125Ru and 19 B in $Ru_{87}B_{13}$) in a periodic supercell volume of 2 nm^3 at 0 K. While no simulation study has been reported for the Ru-P and Ru-B system, our $Ni_{80}P_{20}$ structure obtained using the same procedure shows excellent agreement with that from previous extensive *ab initio* MD simulations [76]. This confirms the soundness of our approach.

Table 3.1. Equilibrium lattice parameters for crystalline Ru-P and Ru-B alloys obtained from US-GGA calculations.

Phase	Space group	Lattice constants (Å)	Volume ($Å^3$)	K-Points	#Ru	#P(B)	Ref.
Ru	P6-3/mmc(194)	a=2.732, c=4.290, γ=120	27.65	96	2		
P	P2/c (13)	a=9.274,b=9.260, c=24.159, β=105.74	2009.85	4		84	
B	R-3m(166)	a=10.738,b=11.385,c=26.249	1062.56	4		141	
Ru_2P	Pnma(62)	a=5.595(5.902),b=3.968(3.859),c=7.181(6.896)	159.43	64	8	4	a
RuP	Pnma(62)	a=5.553(5.52),b=3.197(3.168),c=6.197(6.12)	110.01	216	4	4	b
RuP_2	Pmmn(59)	a=5.140(5.117),b=4.526(5.893),c=3.923(2.871)	91.26	216	2	4	c
$Ru_{23}B_6$	Fm-3m(225)	a=11.319	362.68	216	23	6	
Ru_3B	I-4(82)	a=9.17, c=4.59	195.19	105	12	4	
Ru_7B_3	Cmc2-1(36)	a=7.519,c=4.749, γ=120	233.65	216	14	6	
$Ru_{11}B_8$	Pbam(55)	a=11.673,b=11.940,c=2.886	399.45	27	22	16	
RuB	Amm2(38)	a=2.877,c=2.867, γ=120	81.10	216	1	1	
Ru_2B_3	Cmcm(63)	a=2.924,c=12.833, γ=120	95.70	216	4	6	
RuB_2	Pmmn(59)	a=4.675,b=2.879,c=4.051	81.10	216	2	4	c

a: Ref.[77], b: Ref. [78], c: Ref. [79].

3.3 Results and Discussion

3.3.1 Stability of amorphous RuP and RuB alloys

To examine the relative stability of amorphous versus ordered RuP and RuB alloys, we first calculated the total energy with varying composition ratios of P and B atoms particularly in the P(B) low content region (below 30 at. % of P and 20 at. % of B), where the transition from a more stable crystalline to amorphous phase was found. The result is summarized in Fig. 3.1, which demonstrates that the RuP (RuB) amorphous phase becomes energetically more favorable than its ordered counterpart when the P (B) content is above 20 (10) at. %. Here, the ordered alloys were calculated by replacing Ru with P or B, starting with the hexagonal close packed structure of pure Ru (with a lattice constant of 2.73 Å). Both ordered and amorphous alloys were modeled using a 72-atom supercell, and the atomic positions and the supercell volume were optimized to minimize the total energy.

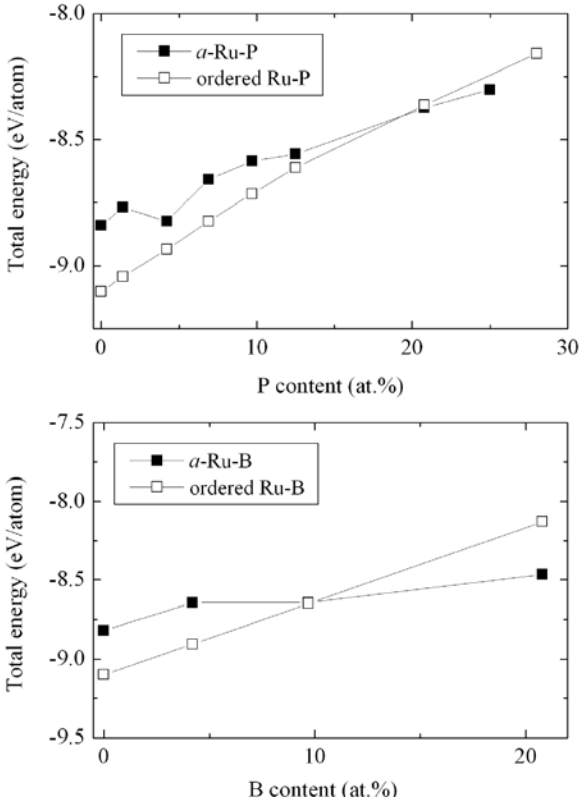

Figure 3.1. Variation in the mixing enthalpy for amorphous and crystalline Ru-P and Ru-B alloys as a function of P(B) content (at. %). The values for amorphous alloys are averaged based on 3 different 64-atom supercells.

Fig. 3.2 shows the predicted volume change exhibiting a distinctive nonlinear trend for the Ru-P alloy but a linear decrease for Ru-B alloy. The Ru-P alloy volume becomes a minimum at 20%, yielding the highest packing density, while the Ru-B alloy volume decrease, leads to increased packing density as B content increases. This is largely due to the large atomic size difference between Ru and B atoms. As expected, the crystalline phase is slightly denser than the amorphous alloy of corresponding composition. The smaller atomic size of B than P atom decreases the composition limit to form an amorphous structure.

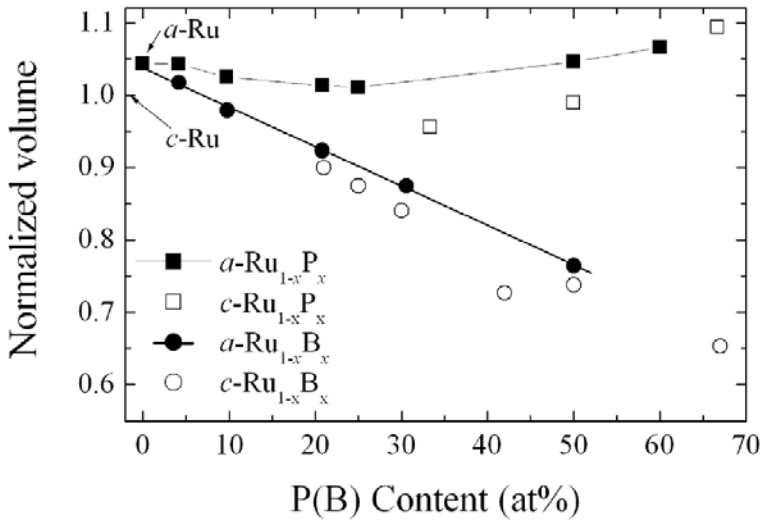

Figure 3.2. Variation in volume for *a*-RuP and *a*-RuB as a function of P(B) content.

For the sake of comparison, we also evaluated the crystalline-to-amorphous transition using the following universal correlation between glass formability and atomic volume ratio in a binary alloy [23]:

$$C_{min} = 0.1/|\gamma^3 - 1| \quad (3\text{-}1)$$

where C_{min} is the minimum concentration of solute element needed to produce the amorphous phase and γ ($=R_b/R_a$) is the radius ratio of the solute (R_b) to the solvent (R_a). The elastic model has been widely adopted in predicting the structural instability of a crystalline binary alloy (as a function of solute concentration) due to the size difference

between solvent and solute atoms. Taking 1.338 Å [80], 1.06 Å [81], and 0.82 Å [82] for Ru, P, and B atomic radii, the required minimum concentrations for P (in an amorphous Ru-P alloy) and B (in an amorphous Ru-B alloy) are estimated to be 19.5 at. % and 11.5 at. %, respectively, which is in good agreement with our DFT calculation results. These results unambiguously demonstrate that the amorphization of binary alloys is mainly driven by the elastic strain contribution arising from the atomic size difference between Ru and P (B) atoms.

Fig. 3.3 shows a variation in the mixing enthalpy for amorphous and crystalline Ru-P(B) alloys as a function of the Ru:P(B) composition ratio, with respect to crystalline Ru (*c*-Ru) and crystalline P(B)(*c*-P(*c*-B)). The mixing enthalpy per atom (ΔE_{mix}) is given by:

$$\Delta E_{mix} = E(alloy) - (1 - x)E_{Ru} - xE_{P(B)}$$

where *E(alloy)* is the total energy per atom of the Ru-P alloy examined, *x* is the number fraction of P(B), and E_{Ru} and $E_{\mathrm{P(B)}}$ are the total energies per atom of crystalline *hcp* Ru and P(B) (*c*-Ru, *c*-P or *c*-B), respectively.

The results indicate that the Ru-P alloy forms the most favorable structure when the P content is around 40-60 at. %, with an energy gain of ~ 0.3 eV/atom, while the mixing enthalpy for the Ru-B alloy gradually decreases with increasing B content and exhibits a minimum value of ~ -0.2 eV/atom at 50 at. %. For the Ru-P alloy, the large negative mixing enthalpies suggest that P atom can easily be incorporated into the amorphous Ru matrix from the P content of 20 at. %. This characteristic was also noticed in the previous study of amorphous RuP thin film, in which the measured P content for the amorphous film determined by X-ray photoelectron spectroscopy (XPS) shows approximately 13~28 at. % [26]. It is also noted that the mixing enthalpy become positive when the P content is small, which might indicate the presence of a barrier for incorporation of P into pure Ru atoms.

For crystalline phases, a distinct mixing enthalpy minimum is found at 50 at. % P, and on average the total energies are ~ 0.3 eV/atom lower than their amorphous counterparts; hence *a*-Ru-P alloys may undergo recrystallization at elevated temperatures,

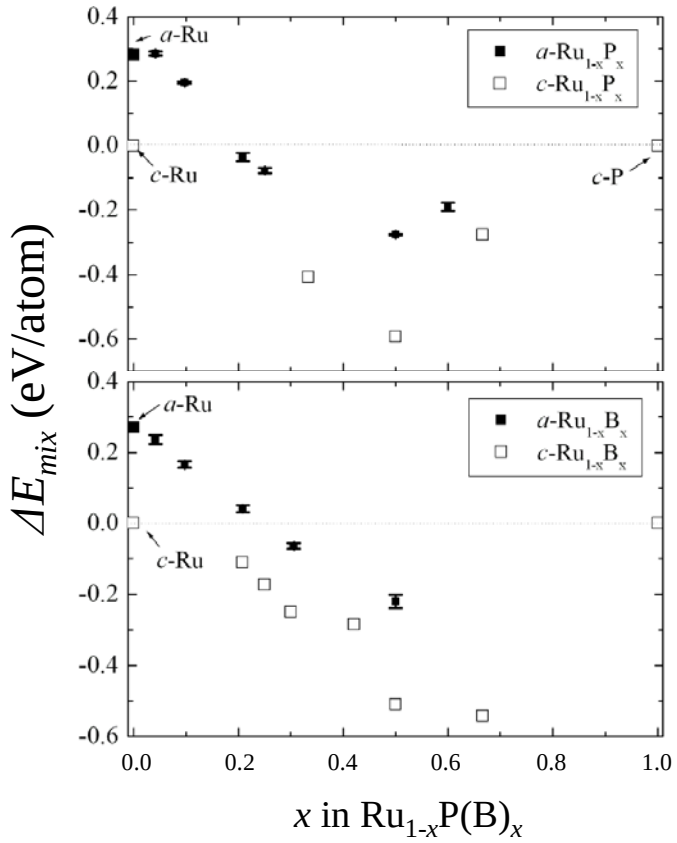

Figure 3.3. Variation of the mixing energy of amorphous Ru-P alloys(a) and amorphous Ru-B alloys(b) in terms of the P(B) content, with respective to crystalline Ru and P(B) structures.

as evidenced by previous experiments, that showed 30 nm thick ~ 15 % alloy remained amorphous upon annealing at 635 K for 3 hr but crystallized upon annealing at 775 or 975 K [26]. The sizable energy gain of the *c*-RuP, relative to the $Ru_{80}P_{20}$ structure, suggests that the Ru-P alloys with a low P content (~ 20 at. %) may undergo decomposition into *c*-Ru and *c*-RuP during high temperature thermal treatment.

Based on the thermodynamic point of view, the amorphous structure forming ability is predicted by the comparison of the mixing enthalpy and mixing enthalpy difference between crystalline and amorphous phases. The lower the mixing enthalpy, the higher the glass forming ability, and the lower the mixing enthalpy difference between crystalline and amorphous phase, the higher the glass forming ability. Based on this

correlation, the lower mixing enthalpy and lower mixing enthalpy difference for Ru-P alloy than Ru-B alloy may enhance the glass forming ability.

3.3.2 Structures

To gain understanding of the structural stability and electronic structure relationship between constituent atoms, we explored the atomic distribution and electronic properties of selected $Ru_{80}P_{20}$ and $Ru_{87}B_{13}$ alloys.

We looked at the structural property of amorphous $Ru_{80}P_{20}$ and $Ru_{87}B_{13}$ alloys. Figure 3.4 shows a set of the partial pair distribution functions from our simulations, together with corresponding crystalline structures for comparison. The amorphous structures were characterized using the pair distribution function (PDF, $g(r)$), which is defined as [83]

$$g(r) = \frac{V}{N}\frac{n(r)}{4\pi r^2 \Delta r}$$

where $n(r)$ represents particles in a shell within the region $r \pm \Delta r/2$, where Δr is the shell thickness; N denotes the number of particles in the model volume V.

The pair distribution function $g(r)$ was computed using 3 different 144-atom supercells for good statistics. No sharp second-neighbor peak is present, which confirms the amorphous nature (i.e., a lack of long-range order) of the Ru-P and Ru-B alloys. The first peak in $g_{Ru\text{-}Ru}$ (r) of *a*-$Ru_{80}P_{20}$ is around 2.7 Å, which nearly corresponds to the bond distance of amorphous Ru (2.7 Å), while the first peak of $g_{Ru\text{-}Ru}(r)$ in *a*-$Ru_{87}B_{13}$ is 2.6 Å, which indicates that the *a*-$Ru_{87}B_{13}$ is more closely packed than *a*-$Ru_{80}P_{20}$ even at lower B content than P content.

For the partial pair distribution functions for P(B), the statistics for the $g_{P\text{-}P}(r)$ and $g_{B\text{-}B}(r)$ are not good compared with the crystalline counterparts with CN = 0; the small intensity of a partial peak and a calculated coordination number of 0.85 (at cut-off of 3.27 Å) and 0.44 (at cut-off of 3.03 Å) for P and B, respectively, describe the existence of dimers (P_2 and B_2). The partial pair distribution functions between Ru and P(B), $g_{Ru\text{-}P}(r)$ and $g_{Ru\text{-}B}(r)$, are also shown in Fig. 3.4. The first peaks in *a*-$Ru_{80}P_{20}$ and *a*-$Ru_{87}B_{13}$ are at

2.4 Å and 2.3 Å, respectively, and yields high intensity. This suggests the strong intermixing between the Ru and P(B) atoms, namely, a strong chemical short-range order. This result is similar to the model proposed by Lee et al. for the Au-Si alloy, which shows strong short-range order with the negative mixing enthalpy. [84]

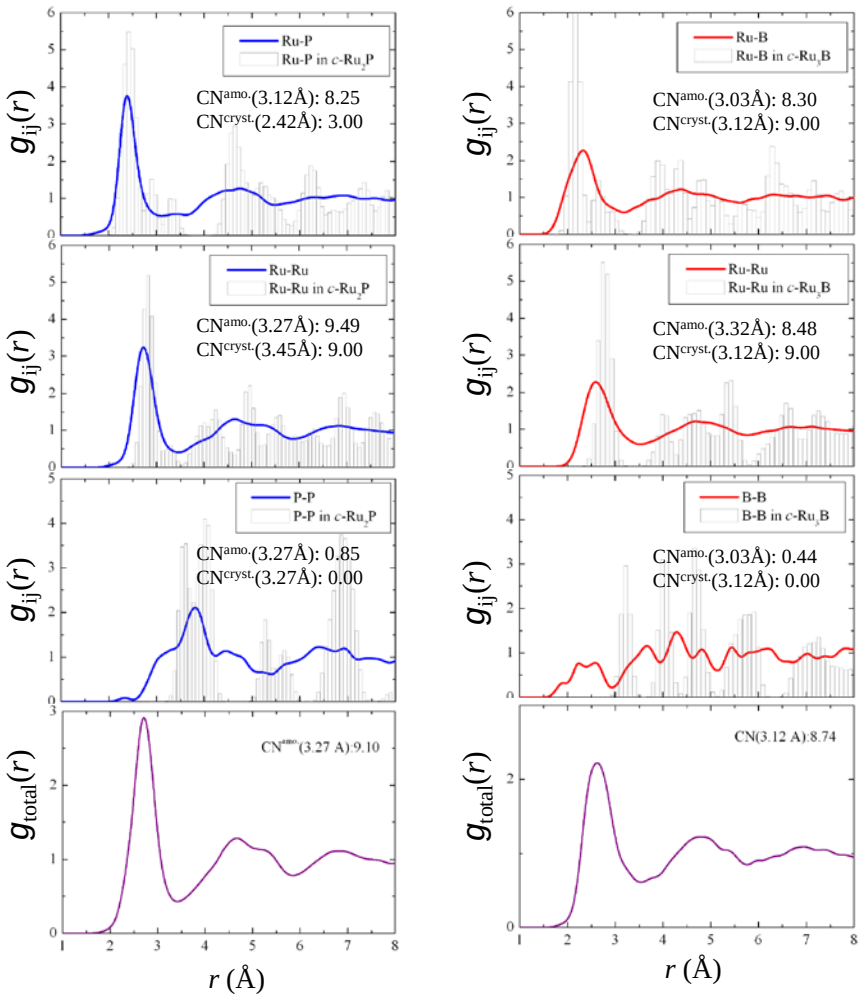

Figure 3.4. Partial pair distribution function, g(r), of the *a*-$Ru_{80}P_{20}$ (a) and *a*-$Ru_{87}B_{13}$ (b) alloys at the ground state.

For the total pair distribution function, the *a*-$Ru_{80}P_{20}$ and *a*-$Ru_{87}B_{13}$ alloys show distinct amorphous character as evidenced by the split second peak, where the average coordination number of Ru around P and B are 9.10 and 8.74, respectively.

From these features of $g(r)$, we can estimate that the structures of the amorphous alloys are governed by a chemical ordering effect due to the chemical interaction between the Ru and the P(B) atoms. More insight into the structural changes is gained by analyzing the structures and characterizing the local environment surrounding P(B) atom by Ru atoms. As displayed in Table 3.2, we calculated the first-neighbor coordination number (CN) of the Ru atoms around P and B at selected $Ru_{80}P_{20}$ and $Ru_{87}B_{13}$ alloys as a function of the normalized cutoff radius, r^*. With increasing r^*, the average coordination number increases.

Table 3.2. Average coordination number of P and B atoms as a function of cutoff radius. Here, the cutoff radius (r^*) is normalized with respect to 2.4 Å, which was the average nearest neighbor Ru-P distance in the RuP alloy considered. The upper insets show the simulated structures of Ru, *a*-$Ru_{80}P_{20,}$ and *a*-$Ru_{87}B_{13}$ alloys in the amorphous state. The large, green balls represent Ru atoms; small, purple balls represent P atoms; and small, red balls represent B atoms.

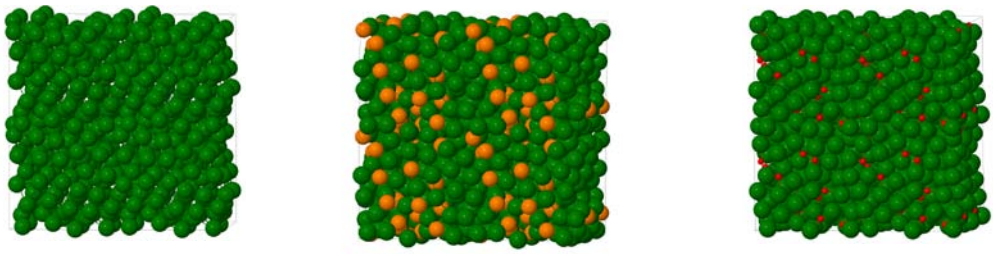

a-Ru *a*-$Ru_{80}P_{20}$ *a*-$Ru_{87}B_{13}$

Alloy	Basis Atom	Average coordination number				
		r^* = 1.1	r^* = 1.2	r^* = 1.3	r^* = 1.4	r^* = 1.5
a-Ru	Ru	5.0	8.6	10.9	12.2	12.5
a-$Ru_{80}P_{20}$	P	3.6	9.1	11.8	12.7	13.6
a-$Ru_{87}B_{13}$	B	4.3	9.4	10.9	12.1	13.2

These results also show that pure Ru is less closely packed than the alloys. This finding is attributed to the relatively smaller size of P or B atoms comparing to the Ru atoms. The CN of $Ru_{80}P_{20}$ is somewhat lower than that of $Ru_{87}B_{13}$ within the nearest neighbor distance ($r^* < 1.2$). However, when r^* is large (>1.3), the CN of the $Ru_{80}P_{20}$ is

somewhat greater than that of the $Ru_{87}B_{13}$. The radius of B is smaller than that of P; therefore the average CN of Ru around the B atoms within the nearest neighbor distance is lower than that of Ru around the P atoms.

3.3.3 Voronoi analysis

Disordered atomic configurations are used to explore the short and medium range details by using the tessellation method [55, 56], which characterizes the local atomic environment. The RuP or RuB alloy with a moderate P or B content results in a glassy structure exhibiting a distinct topological and chemical short-range order. The type of coordination polyhedron around a P(B) atom can be specified using the Voronoi index <*i*3,*i*4,*i*5,*i*6,…>, where *i*n indicates the number of n-edged faces of the Voronoi polyhedron and Σ*i*n is the total CN, to designate and differentiate the type of coordination polyhedron surrounding the center of solute atoms. For *a*-$Ru_{80}P_{20}$ structure (Fig. 3.5a), the solute coordination polyhedra form the TTP (tri-capped trigonal prism packing), which corresponds to a Voronoi index of <0,3,6,0> ; mono-capped square Archimedean antiprism (slightly distorted from the TTP), which corresponds to a Voronoi index of <0,5,4,0>; and CN (coordination number) 10 polyhedra, which has a Voronoi index of <0,4,6,0>. For *a*-$Ru_{87}B_{13}$ structure (Figure 5-5b), the solute coordination polyhedra form the CN8 Kasper polyhedron, with a Voronoi index of <0,4,4,0>, and CN9 TTP (tri-capped trigonal prism packing), which corresponds to a Voronoi index of <0,3,6,0>. The dominant polyhedra of the solute in alloys are shown in Table 3.3.

Voronoi analysis indicates that the average CN is 9.3 for the RuP alloy, and 8.4 for the RuB alloy, which corresponds to the average CN calculated from the integration of PDF first peak.

It is well known that the preference polyhedra and CN are governed by the effective atomic size ratio, λ between solvent and solute atoms [76]. For instance, an earlier study shows that with decreasing λ, the preferred polyhedra changes from the Frank-Kasper type (for λ >1.2) to the icosahedral type (λ =0.902), and then to the BASP type (λ =0.835), and then to the TTP type (λ = 0.732). Considering the dominant CN of 9,

we can expect that the polyhedron with a Voronoi index of <0,3,6,0>, TTP phase found in the RuP alloy is similar to that found in $Ni_{81}B_{19}$, while the polyhedron, <0,4,4,0> found in the RuB alloy, which has the CN of 8, is also a part of polyhedra found in NiB alloy. While no simulation study has been reported for RuP and RuB, we also calculated the $Ni_{80}P_{20}$ and $Ni_{80}B_{20}$ as part of the verification of RuP and RuB. The dominant polyhedra found in the $Ni_{80}P_{20}$ and $Ni_{80}B_{20}$ alloys in my present work are [<0,2,8,0> , <04,6,0> , <0,2,8,1>] and [<0,3,6,0> , <04,4,0> , <0,2,8,0>], respectively. In addition, the average CN of the P and B atoms is 10.5 and 9.1 for NiP and NiB, respectively. These are very similar to previous findings [76], that show the dominant polyhedra in $Ni_{80}P_{20}$ and $Ni_{80}B_{20}$ are <0,2,8,0> and <0,3,6,0>, respectively. Therefore, it is evident that our approach to elucidate the short range order and coordination number for RuP and RuB is sound in predicting the glass properties as well.

Table 3.3. The dominant polyhedra of the solute atoms in the metallic alloy. The values are the fraction of solute atoms in the metallic alloys and only the polyhedra relevant to our work are shown.

	Voronoi index					
	<0,4,4,0>	<0,3,6,0>	<0,5,4,0>	<0,2,8,0>	<0,4,6,0>	<0,2,8,1>
a-$Ru_{80}P_{20}$	0.05	0.24	0.24	-	0.24	-
a-$Ru_{87}B_{13}$	0.6	0.4	-	-	-	-
a-$Ni_{80}P_{20}$	-	-	-	0.7	0.1	0.1
a-$Ni_{80}B_{20}$	0.21	0.43	0.07	0.21	-	-

As is also shown in Fig. 3.5, the formation of ‘quasi-equivalent’ P-centered Ru clusters arising from topological and chemical short-range order is also likely to lead to the medium- range order in the binary alloy. In fact, the short-to-medium range order is seen in other metallic glasses, particularly in transition metal-metalloid and transition metal-transition metal systems where the chemical short-range-order is significant [75, 85, 86].

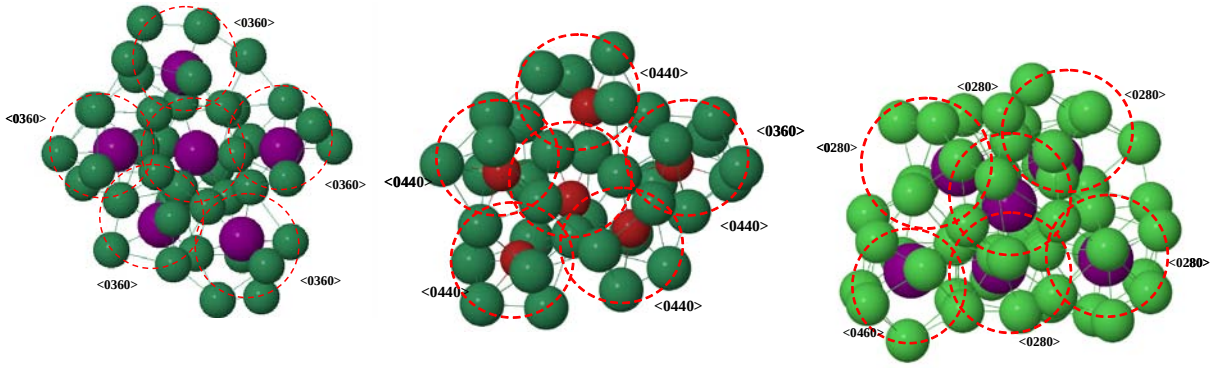

(a) (b) (c)

Figure 3.5. The packing of the solute atoms-centered clusters with an icosahedral ordering of the $Ru_{80}P_{20}$(a), $Ru_{87}B_{13}$(b) and $Ni_{80}B_{20}$(c) alloys. Inner five dark atoms represent P in (a), B in (b) and (c).

In $Ni_{80}P_{20}$ [76], the P atom-centered clusters (Fig 3.5c) are packed with the icosahedral order, which is very similar to the topological configuration with the *ab initio* MD (AIMD) simulation. In the same manner, RuP has shown the icosahedra type regardless of the type of short-range order. These results indicate that the medium-range order found in the metal-metalloid binary alloy has the icosahedral ordering, which has the most stable packing in metallic glasses.

3.3.4 Electronic properties

To incorporate the chemical effect in Ru-P and Ru-B alloys, electronic interaction analysis between Ru and P(B) atoms is performed. Here, we explore the nature of those bonds in terms of their electronic structures. Bulk bonding is dominated by the strong covalent bonding between the Ru d-orbital and the P p-orbital. The p-d bonding is most clearly seen in the electronic density of states (DOS). The Fermi level is used as the reference energy state. In the partial DOS in Fig. 3.6 (a), the peaks of occupied state densities between -7.0 ~ -4 eV mainly originate from the P 3p and Ru_4d intermixing, resulting in high degree of Ru 4d and P 3p hybridization. It is apparent that the strong p-d hybridization mainly contributes to stabilizing the RuP alloy structure. It is also noticed

that the DOS of P atom accumulated at the Fermi level indicates that the RuP alloy is metallic.

The calculated DOS for the RuB as shown in Fig. 3.6 (b) shows no gap at the Fermi level, indicating that the RuB alloy is also metallic. In the energy range between -2 eV and -7 eV, we can also see a hybridization of Ru 3d with B 2p states. However, its intensity of intermixing is relatively lower than that of RuP, implying that the Ru and B tend to be less attractive. Those electronic interactions are expected to be negative in the mixing enthalpy for both RuP and RuB alloys.

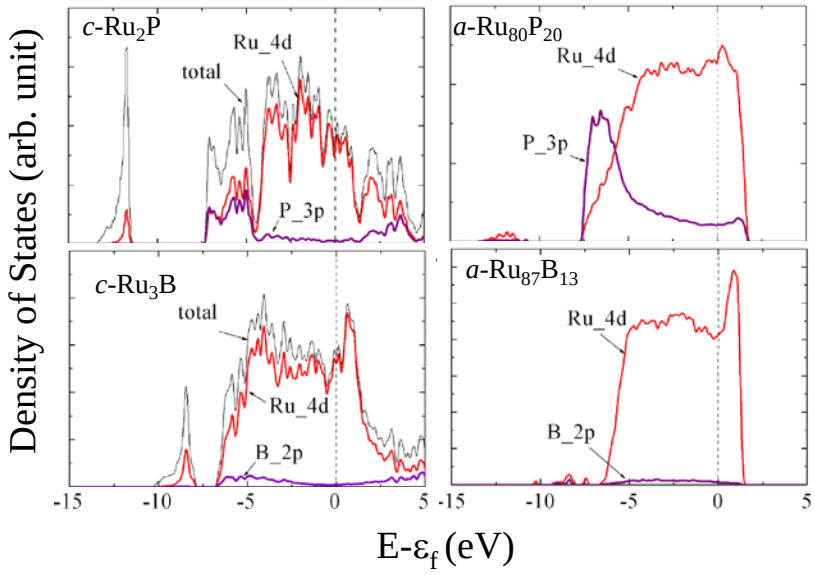

Figure 3.6. Total and local DOS of $Ru_{80}P_{20}$ and $Ru_{87}B_{13}$ along with crystalline phases.

3.4 Summary

Our *ab initio* molecular dynamics (AIMD) study shows that Ru-P and Ru-B alloys with moderate P(B) content can result in glassy structure exhibiting the topological and strong chemical short and medium range order. Amorphous phases above ~20 at. % of P and ~ 10 at. % of B are energetically more favorable in the P(B) low content region than the crystalline counterparts for for Ru-P and Ru-B alloys, respectively. In the region where the crystalline phases of Ru-P and Ru-B alloys exist, the sizable energy gain of

crystalline phases are more favorable than the amorphous phases, however amorphous phases tend to remain due to the negative mixing energy.

In the $Ru_{80}P_{20}$ structure, the P-centered polyhedra prefer the TTP phase with Voronoi index <0,3,6,0>, while in the $Ru_{87}B_{13}$, the B-centered polyhedra prefer the <0,4,4,0>. In addition, the Ru-P and Ru-B systems show the icosahedral medium range ordering arising from packing the 'qusai-equivalent' P-centered (B-centered) clusters in three dimensional spaces. Our findings provide insight into the nature of local packing in Ru-P and Ru-B amorphous structures arising from the significant hybridization between Ru 3d and P 3p (B 2p).

Chapter 4:
The nature and Origin of P(B) Surface segregation in Amorphous RuP and RuB alloys

4.1 Introduction

The surface enrichment of a solute in binary alloy system is known as surface segregation and the energy cost of transferring a solute atom from the bulk to the surface is called surface segregation energy [87]. The surface segregation energy can be easily calculated by the total energy difference between the total energy of alloy having a solute in the bulk and in the surface. However, it is not clear how the surface segregation affects behavior of P or B in amorphous Ru alloys, and the atomic details of the segregation, structure and mechanism remain for the highly concentrated Ru-P and Ru-B alloys.

In this chapter, we use density function theory based *ab initio* molecular dynamics (AIMD) to determine the surface properties of an amorphous Ru-P and Ru-B alloys.

4.2 Method

AIMD and static structural optimization were performed using the planewave program VASP (Vienna *Ab initio* simulation package) [21, 66, 67]. We used the generalized gradient approximation (GGA) derived by Perdew and Wang (PW91) [65] to density functional theory (DFT). Vanderbilt-type ultrasoft pseudopotentials [6] were employed to describe the ion-electron interaction with valence configurations of $4d^7 5s^1$ for Ru, $3s^2 3p^3$ for P and $2s^2 2p$ for B. Outer electron wave functions were expanded using a planewave basis set with a kinetic energy cutoff of 300 eV. The Briliouin zone integration was performed using one k-point (at Gamma). All atoms were fully relaxed using the conjugate gradient method until residual forces on constituent atoms become smaller than 5×10^{-2} eV/Å.

For models, we prepared a roughly 23 Å-thick slabs of amorphous $Ru_{80}P_{20}$ with 115 Ru and 29 P and $Ru_{85}B_{15}$ with 122 Ru and 22 B. The initial slab structures were created by inserting a vacuum layer (10 Å) into the bulk *a*-$Ru_{80}P_{20}$ and *a*-$Ru_{85}B_{15}$ that

was generated using combined modified embedded atom method (MEAM) and AIMD simulations [84], followed by AIMD annealing and quenching for surface relaxation. Initial content of P and B were distributed uniformly throughout the slab.

AIMD simulation was performed in the canonical ensemble with varying temperature. All atoms were allowed to rearrange at 2000 K for 2 ps and subsequently quenched to 300 K with a rate of 1.6 K/fs, followed by relaxation at 300 K for 1 ps, and followed by geometric optimization at 0 K.

4.3 Results and discussion

4.3.1 Surface segregation energy

The difference in the total energies of the system with the impurity in a surface layer and in the bulk is used to calculate the surface segregation energy as is defined by;

$$E\_segr = E\_surface - E\_bulk \quad (4\text{-}1)$$

where *E_surface* and *E_bulk* are the total energies of the model with the impurity in a surface and in the bulk, respectively. The negative segregation energy indicates the segregation of the impurity (solute) towards the surface of the host, and the positive segregation energy means the antisegregation of the impurity where impurity prefers to remain in the interior of the host. A database of surface segregation energies in transition metal alloys has been established by Christensen et al. [87, 88]. Using the first principles total-energy calculations based on density-functional calculations, we calculated the surface segregation energy of P and B in amorphous Ru-P and Ru-B alloys.

The calculated segregation energy of the P and B atoms in the RuP and RuB alloys exhibit -3.2 eV and 1.0 eV, respectively. According to the criteria in the reference [87, 88] the P has strong segregation energy and tends to segregate at the surface, while the B atoms with a strong antisegregation energy, tend to stay in the bulk.

The segregation energy is obtained for single impurities at closed packed surfaces, however, the segregation energy at other surfaces for example, different composition and surface direction, may be quite different.

To see the behavior of P or B atom in an amorphous Ru-P(B) alloy surface, we performed the *ab initio* molecular dynamic simulation in the canonical ensemble.

4.3.2 Surface segregation in the RuP and RuB alloys

Fig. 4.1 shows the variation in the P and B content along the direction perpendicular to the slab (z direction in the model slab structure). This result indicates that the P atom undergoes surface segregation while being depleted at the slab center. The side-view snapshot before and after the atomic rearrangements also clearly demonstrate the surface enrichment of P atoms as shown in Fig. 4.2.

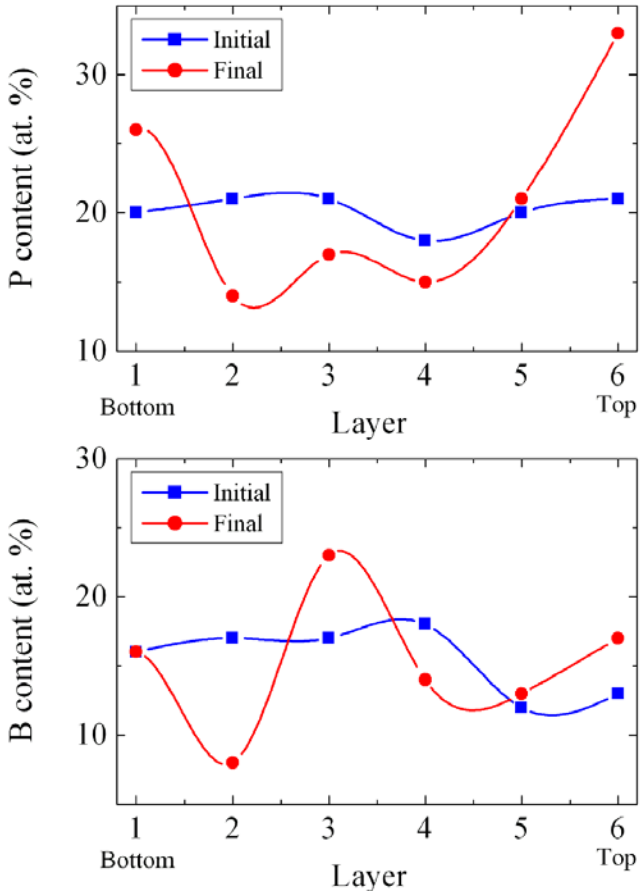

Figure 4.1. Initial and steady state RuP and RuB alloy structures in the presence of the flat surface for the results of MD simulation, which illustrate changes of the atomic distribution of P atom near the surface starting from the well distributed P 20 at. %, B 16 at. % at the initial stage.

This result is in good agreement with the XPS depth profiles that showed a large enrichment of P atoms at the surface of the film (~ 30 at. %) compared to the bulk content (~ 20 at. %) at 575 K [25]. However, the B does not show the same trend in content distribution, instead, B enrichment appeared around the third subsurface layer during thermal treatment, meaning that the surface segregation is not likely to occur. This result is consistent with the negative mixing enthalpy of amorphous Ru-B alloys that shows the negative mixing enthalpy at around 40 ~ 50 at. %. More details on the RuB alloy properties will be presented elsewhere.

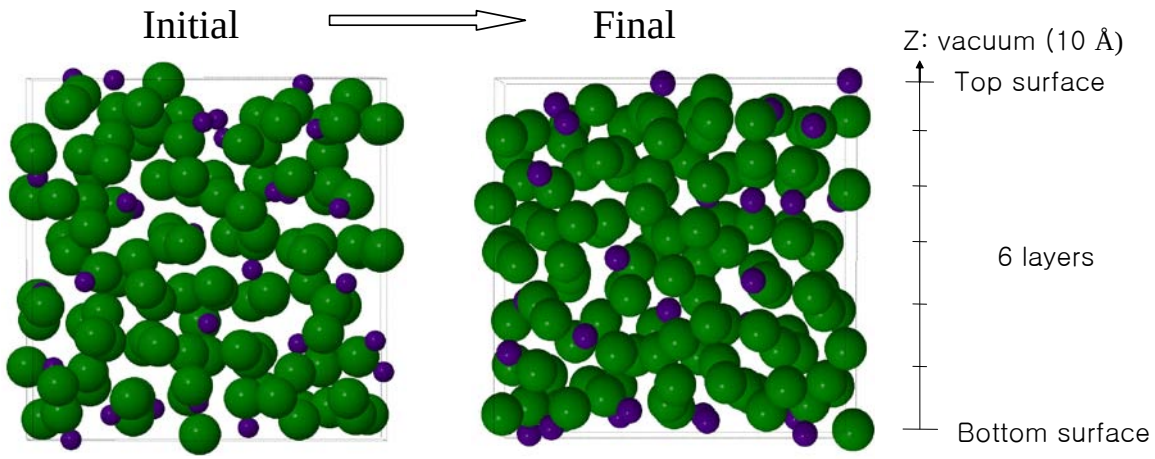

Figure 4.2. Side view of the thin *a*-$Ru_{80}P_{20}$ slab (a) before and (b) after P surface segregation. Initially, 115 Ru and 29 P atoms were almost uniformly distributed in the 23 Å thick slab. The big green and small purple balls represent Ru and P atoms, respectively.

4.3.3 Electronic structure

To gain an understanding of the surface segregation/antisegregation cause for the *a*-$Ru_{80}P_{20}$ and *a*-$Ru_{85}B_{15}$ slab alloys, we examined how the P (B) affects the surface electronic structure of these alloys. To understand the possible correlation of the electronic structure change and the surface segregation, we calculated changes in the partial density of states (PDOS) of Ru and P(B) atoms with varying Ru/P(B) distributions across the slab thickness.

Fig. 4.3a shows the Ru 4d states in the near-surface and center regions of an amorphous Ru (*a*-Ru) slab. The main changes in the Ru 4d state at the surface relative to center are the narrowing of the d band due to the reduced coordination of the surface atoms and the depletion of the peak position 5.5 eV below the Fermi level. In addition, the DOS has an overall metallic character. However, it appears that there is a minimum at the Fermi level. This accounts for the electronic conductivity barrier. Here the Fermi level is used as the reference energy state, which is set to be zero. Fig. 4.3b presents the Ru 4d DOS for the surface and center of the *a*-$Ru_{80}P_{20}$ alloy slab. Ru atoms in the surface layer showed important features with the segregated P compared with the clean surface; the surface states -6 eV below the Fermi level is a region of increased charge as P atoms are enriched at the surface. The shift of the surface 4d features to higher binding energies indicates increased stabilization of the surface structure, thereby lowering the total energy. On the other hand, the depletion of P atoms (~ 10 at. %) in the center region makes the charge move into the higher binding energy region from the peak state (~ 5.5 eV), suggesting that the P atoms in the bulk tend to be stabilized without decomposition into *a*-Ru and the nearby stable compounds.

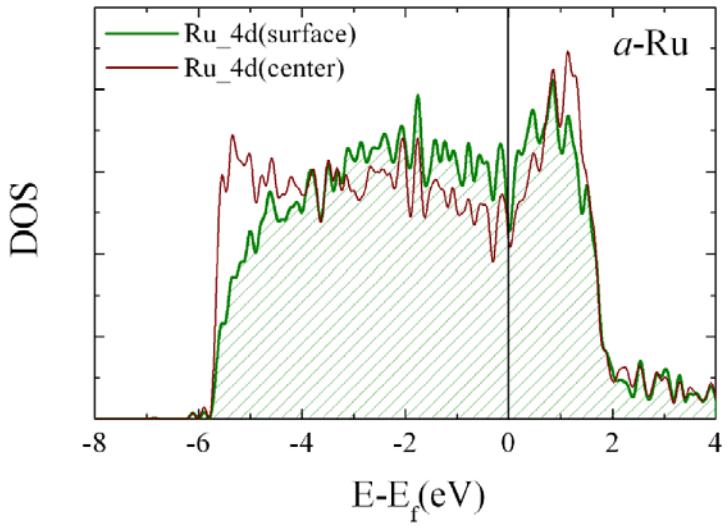

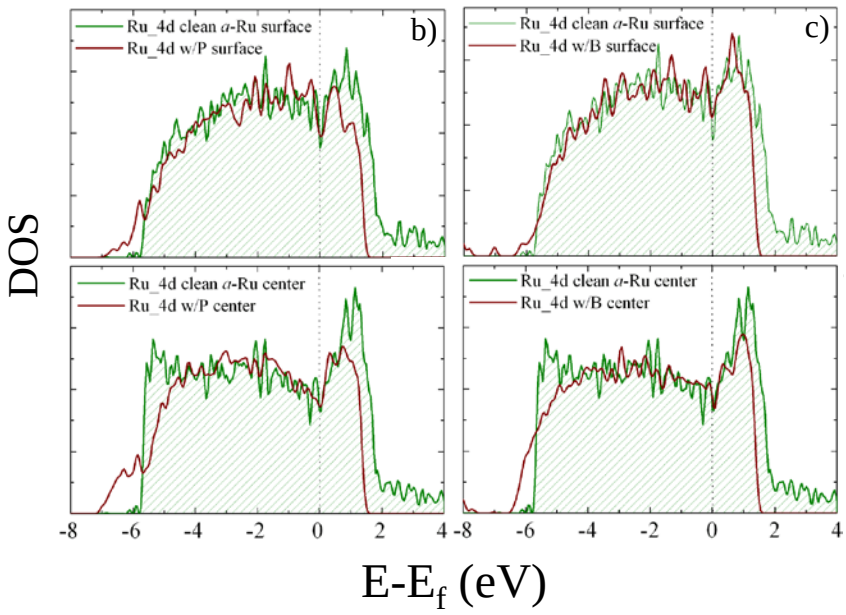

Figure 4.3. Density of states (DOS) of the surface and center layers of the (a) *a*-Ru slab structure, b) *a*-$Ru_{80}P_{20}$ alloy slab, and c) *a*-$Ru_{85}B_{15}$ alloy slab. The dotted line indicates the Fermi level.

Fig. 4.3c shows the 4d DOS of Ru in the surface and center regions of the *a*-$Ru_{85}B_{15}$ slab, together with a clean *a*-Ru slab. The most distinctive features relative to the result of the Ru-P slab alloy is that the change in the 4d state of Ru at the surface seems not to be significant. This result suggests that the effect of compositional change of B atoms across the slab is not likely to be preferred. However, the effect of B in the center region is quite similar with that of P in the Ru-P alloy, which tends to be stabilized with high binding energy.

Our results demonstrates that the P atoms have a tendency to remain at the surface while the B atoms preferred to remain in the center region with high binding energies relative to a clean surface and pure center.

4.4 Summary

Using AIMD and static calculation within the density function theory, we identified the surface segregation and its related electronic property changes of Ru-P and

Ru-B alloy slabs. For a thin $Ru_{80}P_{20}$ layer which initially has a uniform P distributions at 20 at. % across the slab layers, our AIMD results clearly showed a large enrichment of P atoms at the surface of the film (~ 30 at. %) compared to the bulk content (~ 10 at. %). However, the B does not likely to enrich at surface, indicating that the surface segregation is not likely to occur. By analyzing the electronic structure we also elucidated that surface electronic structure change into high binding energy make the P atoms remain at the surface, while the increased binding energy of B atom in the center region of *a*-$Ru_{85}B_{15}$ alloy slab make the B atoms remain in the bulk.

Chapter 5:
Investigations of Ruthenium - Copper and RuP alloy - Copper Interfaces

5.1 Introduction

In microelectronics devices, copper is widely used as an interconnect to enhance operating speed and reliability. While Cu provides several advantages over the Al metal, such as lower resistivity and higher electromigration resistance, a diffusion barrier is needed since Cu readily diffuses into silicon to act as an impurity or to form a silicide. Currently, Ta or TaN is deposited on an interlayer dielectric to serve as the Cu diffusion barrier. However, Ta or the TaN may not be extendable to the 32 nm generation of devices and beyond to ultra-thin (< 3 nm) devices. In addition, Ta or TaN films have poor interfacial adhesion to the copper film. These defects have motivated studies on new barrier layer materials, such as WN, TiSiN, and Ru. Ruthenium has been considered for a number of microelectronic applications including serving as a Cu diffusion barrier and Cu seed layer due to its low resistivity (~7 μΩ cm), chemical stability, and low solubility with Cu [89]. However, ruthenium films, which are structured with columns, impose some barrier limitations on the diffusion. Fast copper diffusion occurs more frequently through grain boundaries than in the bulk [90]. To improve barrier properties, we control the microstructure of Ru film changing it from polycrystalline or columnar to amorphous by employing the *cis*-$RuH_2(PCH_3)_4$ precursor in the CVD process [91]. This precursor with phosphorus plays an important role in making amorphous RuP film. We find that this film remains amorphous upon annealing to 635 K; thus, there is no diffusion of Cu into the Si substrate.

Cu adhesion strength on the metal surface is also of particular interest. Based on our experiments, we estimate that the adhesion strengths are in the order of CVD RuP > PVD Ta > PVD TaN [92]. However, indirectly assessing adhesion strength using low/energy ion scattering spectroscopy (LEISS) and X-ray photoelectron spectroscopy (XPS) may require more accurate calculations or experiments. In addition, understanding

of the electronic properties of the interfaces is typically incomplete because of the complexity of the phases between the two interfaces.

This work focuses on understanding how the interface chemistry and morphology affect adhesion. We theoretically calculate the ideal work of separation for Cu(111)/Ru(0001), Cu(111)/*a*-Ru, and Cu(111)/*a*-RuP. We explore the relation between the energetics and the details of the atomic and electronic structures of the Cu/Ru, Cu/RuP since microscopically; adhesion is related to the strength of the electronic bond between atoms at the interface with different phases and the P impurity.

5.2 Calculation Method

Static optimization and ab-initio molecular dynamic were performed using the well-established planewave program VASP (Vienna *ab-initio* Simulation Package). [21, 66] We used the generalized gradient approximation (GGA) derived by Perdew and Wang (PW91) to density functional theory (DFT). Vanderbilit-type ultra pseudopotentials were employed to describe the ion-electron interaction with valence configurations of $4d^7 5s^1$ for Ru, $3d^{10} 4s^1$ for Cu, and $3s^2 3p^3$ for P. Outer electron wave functions were expanded using a plane-wave basis set with a kinetic energy cutoff of 300 eV. The Brillouin zone integration was performed using a Monkhorst-Pack $9 \times 9 \times 1$ k-points mesh for the interface structure and $3 \times 3 \times 3$ for crystalline and amorphous structures. All atoms were fully relaxed using conjugate gradient method until residual forces on constituent atoms become smaller than 5×10^{-2} eV/Å.

For the crystalline-crystalline interface model, the lattice parameters of bulk ruthenium and copper obtained in the GGA [61] from calculated energy-volume curves [Murnaghan equation of state [73] are *a*(Ru) = 2.73 Å and *c/a* (Ru) = 1.57 [*a*(Ru)(exp) = 2.71 Å, c/a = 1.58 [93]] and *a*(Cu) = 3.64 Å [*a*(Cu)(exp) = 3.61 Å [93]. The interface system of the Cu film on the Ru substrate is modeled by periodic boundary conditions for all directions, where Ru film is composed of five atomic (0001) layers (stacking in A-B-A-B-A), and the Cu film is composed of seven atomic (111) layers (stacking in A'-B'-C'-A'-B'-C'-A').

Fig. 5.1a displays a top view of the interface cells of Cu(111)/Ru(0001) containing one layer of Cu and three layers of Ru, superimposed and aligned in which the close-packed Cu(111) planes are parallel to the close-packed Ru(0001) planes, and the closed-packed directions of Cu(1-10) are parallel to the close-packed direction in Ru(10-10). The translations considered here are (1) top positions, where Cu atom is situated above a Ru atom (this is expected to be the least stable configuration), 2) Cu on a FCC position, and (3) Cu on a HCP position as shown in Fig. 5.1b. Accommodating the lattice misfit at the plane of *x* and *y* axis requires strain of the softer Cu(111) slab than the harder Ru(0001) slab and also results in axial compressive strain of Cu(111). The optimized slab distance was determined by calculating the total energy of the slab structure at several values of the distances as shown in Fig. 5.2. The minimum of the total energy can be used to determine the slab distance.

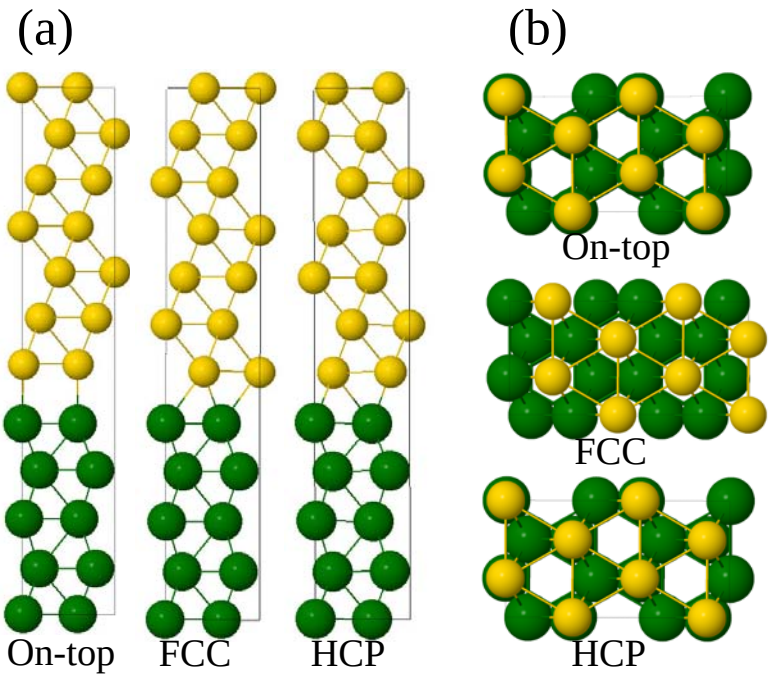

Figure 5.1 The Cu(111)/Ru(0001) for the thin film model structures(a) and monolayer (b).

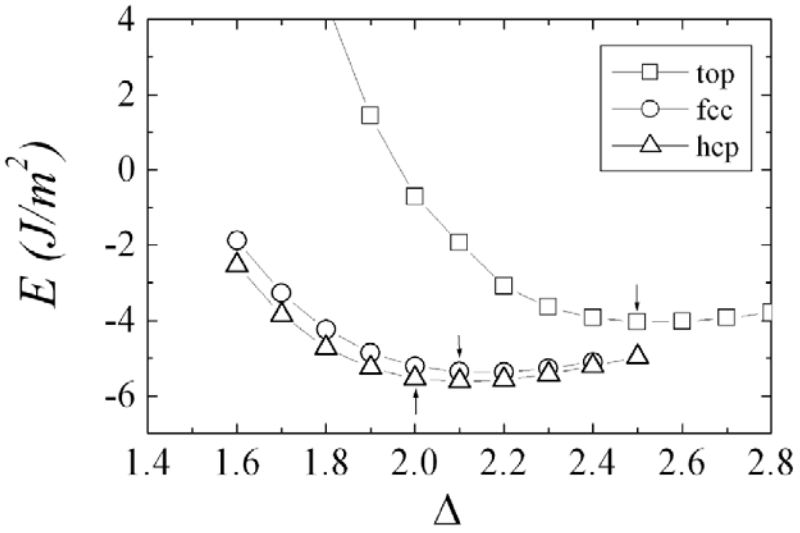

Figure 5.2. The interfacial binding energies (the negative W_{sp}) for a thin Ru(0001) film on a Cu(111) substrate.

For the crystalline-amorphous interface model, we prepared an amorphous Ru (hereafter *a*-Ru) with 56 atoms and crystalline Cu (111) with 48 atoms. A small *a*-Ru supercell, which can be matched with Cu slab in the direction of Cu(1-10) and Cu(11-2), is truncated from the 144-supercell from the previous work [92]. Five different samples of *a*-Ru containing 56 atoms in a periodic supercell volume of 0.8 nm^3, were generated by melting at 3,500 K for 2 ps with a time step of 1 fs, and then quenching to 300 K at a rate of 1.5 K/fs using *ab initio* MD (AIMD) simulation within a Born-Oppenheimer framework, followed by static structural optimization. The crystalline Cu(111) includes 48 atoms (4 layers) that are matched with the optimized amorphous Ru slab by calculation of the minimum energy in terms of the distance between two slabs. After matching two slabs, AIMD simulation also was performed at 1000 K for 1ps, followed by 300 K for 1ps to explore the bonding properties at the interface between crystalline Cu and amorphous Ru.

To further evaluate the effect of P content in the interface Cu(111)/*a*-Ru(P), we constructed different *a*-RuP supercell, which have different content of P in a *a*-Ru cell, by replacing Ru with P, followed by MD annealing at 3500 K for 4 ps, and then rapidly

quenched at a rate of 1.5 K/fs. Finally, we refined the quenched structures with careful volume optimization and matched with the Cu(111) slab. Therefore, the supercells explored in this study are Cu(111)/Ru(0001), Cu(111)/*a*-Ru, and Cu(111)/*a*-RuP with 16.7 at. % P, 33 at. %, and 45 at. %, as shown in Fig. 5.3.

The adhesion strength of the interfaces is quantitatively established by calculating the ideal work of separation, W_{sp}, which is defined as the reversible work needed to separate the interface into two free surfaces, was employed as follows [94, 95]:

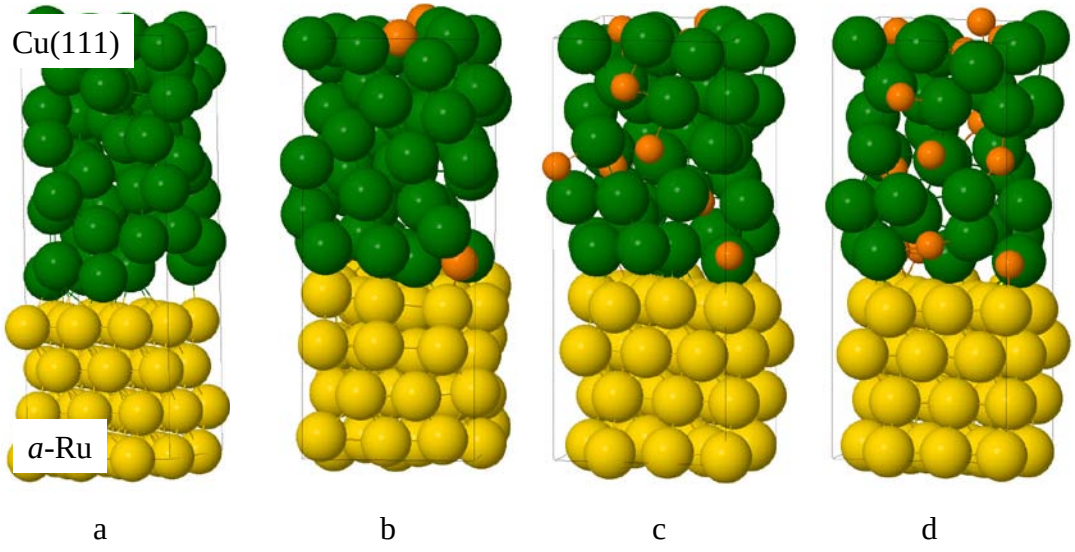

Figure 5.3. Cu(111)/*a*-Ru (a) interface model structures and Cu(111)/*a*-RuP (b,c,d) with different P content (25 at. %, 27 at. %, and 36 at. %) at the interface, respectively. The gold color represents Cu, purple represents P and dark green represents Ru atoms. Large grey (yellow) and dark grey (green) balls represent Cu and Ru atoms, respectively, and small black (orange) balls indicate P atoms.

$$W_{sp} = (E_1 + E_2 - E_{12})/2A \quad (5\text{-}1)$$

where E_{12} is the total energy of the combined supercell considered; E_1 and E_2 represent the total energies calculated by fixing one pure material part as indicated, while the other side is replaced by a vacuum, and A is the total combined interface area within the

supercell model. It is known that the energy needed in cleavage experimental will always exceed W_{sp}, but the greater W_{sp}, the greater the energy needed to cleave the interface [96], so it is considered as a useful quantity to measure the mechanical stability and chemical bonding at the interface. W_{sp} is obtained by rigidly ('unrelaxed' in this work) separating the thin film or monolayer from the substrate without allowing for further relaxation of the cleaved sublattices. The unrelaxed W_{sp} is optimized with respect to the interfacial distance (Δ) by calculating W_{sp} as a function of 'Δ'. For comparison, a calculation of relaxed W_{sp} in this work is performed for the most stable interface so that the effect of relaxation can be estimated.

It is noted that the work of separation, W_{sp}, does not give the relative thermodynamic phase stability in terms of the interface free enthalpies including chemical reactions, diffusion, and surface segregation. The surface stability of a thin film is described by the energy balance as is given by [97]

$$\delta = \gamma_f + \gamma_i - \gamma_s \quad (5\text{-}2)$$

where γ_f and γ_s are the free surface energies of film and substrate, respectively, and γ_i is the film/substrate interface energy. Thin-film growth by the formation of three-dimensional (3D) crystals, known as the Volmer-Weber growth mode, is obtained when $\delta > 0$. The layer-by-layer growth, known as the Frank-van-der-Merwe (FM) mode and the mixed or Stranski-Kranstanov (SK) growth mode are obtained when $\delta \leq 0$. This is also the condition for complete wetting and coverage of the substrate by the film.

To evaluate the thermodynamical stability of the thin film and ML of Cu on Ru substrate, we calculate the interface energy calculated using (5-2) for the film and monolayer. The interface energy is defined as the total energy difference per interface area between a configuration that includes an interface and one in which the same number of atoms are in their respective bulk environments. The thermodynamical quantities that need to be determined are Gibbs' free energy of the interface, and the chemical potentials of fcc Cu and hcp Ru. In the current study, both are approximately by the total energies at zero temperature, which are readily obtained from the *ab initio*

calculations. Under these assumptions and in the case of periodic slab geometry, the excess interface energy can be expressed as

$$\gamma = (E - \gamma_i = (E - \sum n\ u_i) / 2A = \sigma_1 + \sigma_2 - W_{sp,} \qquad (5\text{-}3)$$

where E is the total energy of the supercell system, and n_i and μ_i are the number of atoms and chemical potential of species i and σ_1, σ_2 are surface energies of the two slabs.

For the interface models the Cu is strained in order to make the Cu(111) planes commensurate to the Ru(0001) planes; this form of γ includes the strain energy contribution, which scales with the number of atomic layers of Cu. An alternative approach is to substitute for μ the energy μ' of a Cu atom in a bulk configuration strained in exactly the same manner as in the interface model. As a same consequence, same strain energy is contained in the two terms in the numerator of (5-3) and will therefore cancel. The resulting strain-free excess energy γ' only includes the energies resulting from purely chemical contributions or bonding contributions.

5.3 Results and Discussion

5.3.1 Bulk and Surface

The surface energies were calculated by either keeping atoms in their ideal bulk positions ("unrelaxed" energy) or allowing all atoms to relax ("relaxed" energy), with the exception of the central layer (two central layers). The lattice constant of Ru (relatively more rigid than Cu) is fixed at the equilibrium bulk value obtained with the relevant GGA functional method. However, due to the lattice misfit between Cu(111) and Ru(0001), the Cu lattice parameter is expanded by 5.8 % relative to the calculated equilibrium lattice parameter of Cu, a = 3.64 Å. Therefore, the Cu(111) model is strained laterally by e|| (0.06, 0.06) in the [1-10] and [11-2] directions; as a result, it will contract normally to the interface. This resulted in a reduced Cu interplanar separation in the (111) direction of the commensurate FCC lattice by almost 10 %, $d_{111} = 0.9 \times d^0_{111}$. From our first principles calculations, the free surface energy of a relaxed Ru(0001) surface is γ = 2.546 J/m^2 (unrelaxed Ru(0001) surface energy is calculated to be 2.606 J/m^2), compared

with the experimental value of 3.043, 3.050 J/m^2 [98] and other theoretical values of 3.928 J/m^2 [20], 3.0~ 4.3 J/m^2 [99].

The relaxed surface energy of Cu(111) is calculated to be γ = 1.301 J/m^2 (unrelaxed γ = 1.302 J/m^2), compared with the experimental value of 1.79 J/m^2 [22], and a theoretical value of 1.952 J/m^2 [98]. For a fcc Cu film at the commensurate interface, which is under lateral tensile and axial compressive strains, the relaxed surface energy of the strained Cu(111) is calculated to be γ = 1.300 J/m^2 (unrelaxed γ = 1.302 J/m^2).

For the amorphous Ru slab optimized to fit the Cu slab, which is regarded as a relaxed slab, the lattice parameters of Cu surface commensurate with *a*-Ru surface maintain its equilibrium states in this system. The surface energy of *a*-Ru is calculated to be γ = 2.5 ± 0.3 J/m^2. The optimized distance between slabs, interface interlayer separation is shown in Table 1. The Cu(111)/*a*-Ru has the shortest interlayer distance, while the top position of Cu has the longest interlayer distance.

5.3.2 Ideal work of separation (W_{sp})

We investigated how the ideal work of separation in the different interfaces between Cu and Ru changes with two variables, different interface morphology (crystalline and amorphous) and amorphous phases with different phosphorus content. The resulting ideal work of separation for all strained Cu(111) films on unstrained Ru(0001) and unstrained Cu(111) and strained *a*-Ru(P) substrate is summarized in Table 5.1. For all crystalline interfaces considered, the most stable interface configurations are obtained when the Cu atoms are on hcp sites positions. The on-top sites of the fcc Cu, on the other hand, have more than 1.2 J/m^2 lower W_{sp} than the other interfacial translations. The optimum Δ of the crystalline-crystalline interface is somewhat closer than the amorphous-crystalline interface, while the optimum Δ of Cu(111)/*a*-RuP shows longer distance than the distance of crystalline-crystalline interface, indicating that the doped P at the interface decrease the adhesion strength between Cu and Ru. These results suggest that P terminates strong Cu-Ru bonds at the interface, which is corresponding to the increase of separation distance. From the Cu(111)/Ru(0001) contact angle value reported

[100], the adhesion energy is determined to be 2.94 J/m^2, assuming the surface energy of Cu is 1.38 J/m^2. Calculations show that bonding strength of the crystalline interface has the highest value in the Cu(111) on the hcp site of Ru(0001), while the on-top site translation has the lowest value in W_{sp}, which is not likely to form. It is also noted that the relaxation effect is significant in the Cu(111) at hcp site of Ru(0001) compared with the top and fcc site placement for the crystalline-crystalline interface system. This result illustrates that the atomic position of Cu is strongly allowed to relax when placed on the hcp site of the Ru(0001) surface.

Next, to assess the effect of the P content on adhesion strength between Cu and Ru, we calculated the total energies by varying the P content at the interface of the Cu/RuP. The resulting ideal work of separation (W_{sp}) and separation distance (Δ) are given in Table 5.1. As the P content increases and the separation distance increases, the ideal work of separation decreases, as a result of the fact that the P atom at the interface significantly proscribes the Cu-Ru bonding.

Table 5.1. The calculated ideal work of separation. Experimental values are calculated using the contact angle method [101, 102]. W_{sp}(unrelaxed) is calculated with respected to rigidly cleaved interface, while W_{sp}(relaxed) is calculated with respected the relaxed Cu and Ru free surfaces with the same strain as in the interface. Δ for the amorphous/crystalline is an averaged interface distance.

	Δ (Å)	W_{sp} (J/m^2)		Exp.(J/m^2)
		Unrelaxed	Relaxed	
Cu(111)/Ru(0001) - on Top	2.56	4.30	4.24	2.94
Cu(111)/Ru(0001) - on FCC	2.19	5.60	5.43	
Cu(111)/Ru(0001) - on HCP	2.10	6.06	5.78	
Cu(111)/*a*-Ru	1.90	3.03	2.67	
Cu(111)/*a*-RuP(25 at.%)	2.11	2.60	2.35	
Cu(111)/*a*-RuP(27 at. %)	2.34	2.52	2.23	
Cu(111)/*a*-RuP(36 at. %)	2.37	2.37	1.91	

The relaxation effect is also seen in this system, showing that the atomic position and the energetics of the crystalline Cu change with relaxation much large than that of amorphous Ru. Therefore, the mechanical bonding strength is in the order of Cu(111)/*a*-RuP(44 %) < Cu(111)/*a*-RuP(35 %) < Cu(111)/*a*-RuP(16.7 %) < Cu(111)/*a*-Ru. < Cu(111)/Ru(0001).

5.3.3 Themodynamical stability

To investigate the thermodynamical stability of the Cu film on the Ru substrate, we calculate the excess interfacial energies using Eqn. 5-3 for the thin film and monolayer, which are summarized in Table 5.2. Note that the in the case of ML of Cu on the Ru substrate, the excess interfacial energy calculated from (5-3) contains the excess energies due to the free surface of the monolayer to vacuum and due to the interface between the monolayer and substrate, $\gamma_{ML} = \gamma_f + \gamma_i$. Results show that ML of Cu on the Ru substrate is stable for all but the on-top translation site since the excess interfacial energy does not exceed the free surface of Ru(0001), $\gamma_s = 2.5$ J/m^2, resulting in δ (5-2) < 0, which describes complete wetting. This is consistent with experimental data [103]. The thin film is also stable due to the negative interfacial energy, meaning that the film is well wetted to the Ru substrate. Our results for the interface energies show that the Cu/Ru system has noticeably lower interface energy than the free surface of the Ru substrate. The combination of low interface energy and high work of separation, giving a high wettability of Cu to the Ru, should lead to continuous thin film of Cu on the Ru substrate. This result is comparable with the result of Cu/Ta(110) that shows a monolayer of Cu on Ta(110) is stable thermodynamically, while the Cu film dewets on Ta(110) forming three-dimensional islands on top of the Cu monolayer [104].

5.3.4 Electronic properties

The results discussed above show that the Cu/Ru and Cu/RuP adhesion is mainly due to the strong electronic bonds between the Cu and Ru or P atom. Here we explore the nature of those bonds using the projected partial DOS (Fig. 5.4) for the Cu(111)/*c*-Ru_2P

interface. Compared to the middle layer of atoms, interface atoms have some interesting features in the projected partial DOS of the interface system.

Table 5.2. The excess interface energies at equilibrium separation for the interface of Cu on the Ru(0001) surface. Primed quantities refer to excess energies calculated with respect to strained bulk Cu.

System	Thin film		Monolayer	
	γ	γ'	γ	γ'
Top	0.31	-0.15	3.10	2.97
FCC	- 0.65	-0.98	2.06	1.93
HCP	- 0.85	-1.18	1.98	1.85

First, the Cu-d and Ru-d PDOS are significantly intermixed from -6 eV to E_f, which results in high adhesive energy between Ru and Cu atoms. Second, in contrast, a small amount of electrons of the Cu-d orbital intermix with the electrons of the P 3p orbital, indicating no significant intermixing between Cu 3d and P 3p. Third, the P 3p and Ru 4d orbital between the interface and bulk are significantly shifted up, while the Cu 3d orbital is shifted down, displaying that the interaction between two interfaces somewhat increases. However, the existence of P at the interface reduces the chance to interact between Ru and Cu, thus, the adhesion strength may be decreased. Such a significant rearrangement of the electronic structure results in a strong interaction between the Cu and RuP layers.

To examine the degree to which changes in bonding properties are confined to the interface, and to observe the effect of P in charge transfer in detail, we calculate the charge density difference along the z direction,

$$\Delta\rho(z) = \rho_{IF}(z) - [\rho_{RuP}(z) + \rho_{Cu}(z)], \quad (5\text{-}4)$$

where $\rho_{IF}(z)$, $\rho_{rup}(z)$, and $\rho_{Cu}(z)$ are the charge densities of the Cu/*a*-RuP interface, the Cu layers, and *a*-RuP substrate, respectively, averaged over the *xy* plane.

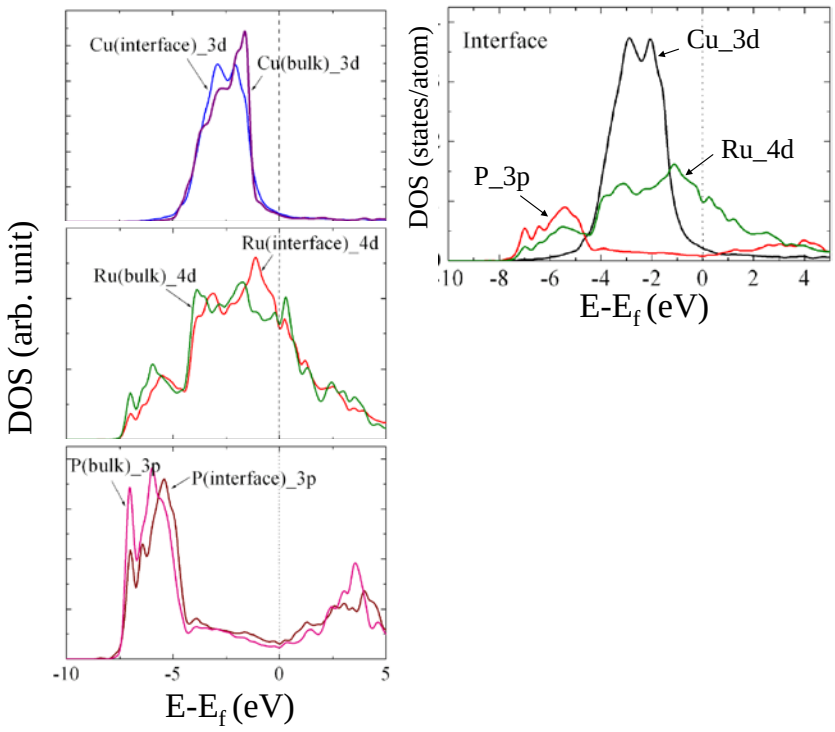

Figure 5.4. The calculated density of states (DOS) for the Cu(111)/*c*-Ru_2P.

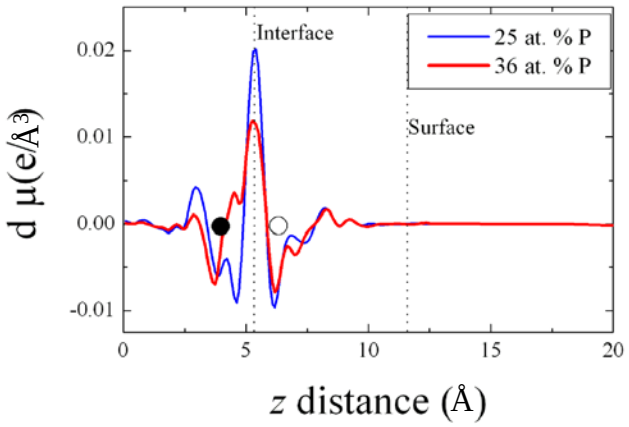

Figure 5.5. Planar-averages change in electron density of RuP-Cu at 33 at. % and 44 at. % of P as a function of the depth *z* from the substrate surface. The positions of each atom are designated by solid circles for Cu atoms; open circles for RuP atoms.

The intensity of the charge density difference at 25 at. % of P is lower than that at 36 at. % P as shown in Fig. 5.5. This result demonstrates that the charge transfer is

prohibited by the P atom at the interface due to the weak interaction between Cu and P atoms. At both cases, electron gains occur at the interface, while the electron loss can be seen around the surface layer of RuP and Cu.

5.4 Summary

A theoretical method has been developed and applied to explain the variation in adhesion strength between the Cu (111) and different phases of Ru substrates (crystalline and amorphous Ru and P-doped *a*-Ru). This approach provides a basis for a fundamental understanding of mechanical stability and adhesion properties of interfaces in Cu interconnect applications. This method is also useful for engineering better interfaces by selective investigation of heterogeneous and/or doped interfaces that would otherwise be expensive and time-consuming to do experimentally.

Chapter 6:
Interface investigations for Ruthenium and amorphous SiO_2

6.1 Introduction

Ruthenium has been considered for a number of microelectronic applications including serving as a Cu diffusion barrier and Cu seed layer [25, 26, 105]. Here, the issue is the interactions between the barrier metal and the oxide substrate. In particular, the Ru and amorphous SiO_2 (hereafter referred to as *a*-SiO_2) interfacial structure and electronic properties are of fundamental interest. However, little is understood about the atomic level interactions at such interfaces.

Previous first-principles work on the metals/SiO_2 [106, 107] used α-cristobalite or β-cristobalite as the model for *a*-SiO_2 because of the difficulty in making *a*-SiO_2 and because their local structures are similar to the amorphous SiO_2. However, matching lattice constants in two crystalline slabs is not simple due to high strain when two slabs meet. In addition, using the crystalline structures results in artificial configurations at the interface. Therefore it is realistic to create the model using the *a*-SiO_2 because this technique might reduce the strain energy arising from lattice mismatch and achieve the real interfacial configuration.

In this work, we investigate the interfacial structure combining Monte Carlo and density functional theory calculations. Using the continuous random network (CRN) model [108, 109], we first generate the *a*-SiO_2 within the periodic supercell matched with Ru slabs and finally optimize the interfacial structures using the *ab initio* calculation. We find that optimum interfacial structure is obtained at the number of non-bridging oxygen, 6, which is consistent with experiment [110]. We also find that the adhesive energy of the most stable Ru/*a*-SiO_2 is found to exist between Ru and *a*-SiO_2 with an adhesive energy of approximately 4.242 J/m^2. This finding is related to the strength of the local electronic bond between Ru and non-bridging oxygen at the interface. Local density of states and charge density difference demonstrate that the interfacial Ru-O bonds are strongly hybridized at the Ru 3d and O 2p orbital. Our calculations allow us to elucidate the role

of local electronic interaction in binding metal film to glass, but also the disordered interfacial configuration.

6.2 Computational Method

Amorphous SiO_2 is generated within the boundary of the crystalline Ru structure using the MC method. To model Ru/*a*-SiO_2, we use a 10 Å vacuum layer, which keeps the interactions between the surfaces in neighboring supercells minimal. We finally anneal the interfacial structural using *ab initio* molecular dynamics (AIMD) within the Born-Oppenheimer framework, followed by static structural optimization. Most of the interfaces are well reconstructed within a time scale of 5 picoseconds at 1,000 K. We generated four representative interfaces corresponding to the possible terminations of bulk *a*-SiO_2, namely those with non-bridging oxygen (NBO) and bridging oxygen (BO) at the interface as shown in Fig. 6.1. Table 6.1 gives the most probable numbers of non-bridging and bridging oxygen, which can be used for evaluating structural and electronic properties at different phases.

The calculations reported herein were performed on the basis of density functional theory (DFT) within the generalized gradient approximation (GGA-PW91) [65], as implemented in the Vienna *Ab initio* Simulation Package (VASP) [21, 66]. The projector augmented wave (PAW) method with a planewave basis set was employed to describe the interaction between ion cores and valence electrons. The PAW method is, in principle, an all-electron frozen-core approach that considers exact valence wave functions. Valence configurations employed are: $5s^1 4d^7$ for Ru, $3s^2 3p^2$ for Si and $2s^2 2p^4$ for O. An energy cutoff of 300 eV was applied for the planewave expansion of the electronic eigenfunctions. During geometry optimization, all atoms were fully relaxed using the conjugate gradient method until residual forces on constituent atoms become smaller than 5×10^{-2} eV/ Å. A (2×2×1) k-point mesh in the scheme of Monkhorst-Pack was used for the Brillouin zone sampling [111] for all slab structures.

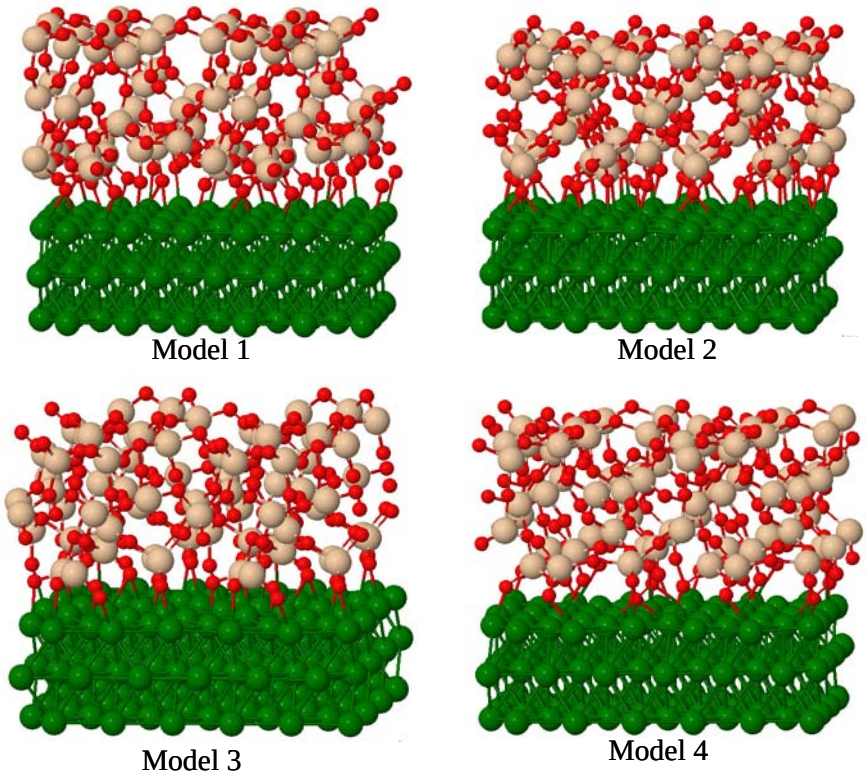

Figure 6.1. Four relaxed structures of the Ru/*a*-SiO_2 interfaces. The large balls are Ru atoms, the middle sized balls are Si atoms, and the smallest balls are oxygen atoms.

6.3 Results and Discussion

6.3.1 Interface geometry

We consider the situation in which Ru is deposited on top of an amorphous SiO_2 surface. The structural possibilities for constructing a Ru/*a*-SiO_2 interface are immense. The key objective is to match lattice vectors in the interface plane of each film so that the overall strain is small when the interface is formed. Amorphous SiO_2 created through Monte-Carlo (MC) simulation can be easily matched with the well-defined crystalline Ru (0001) surface.

The number of bonds for each interface is based on the number of matches with the 12 Ru atoms. Experiment [110] shows that in the fully hydroxylated state of the *a*-SiO_2 , approximately one OH group corresponding to one Si atom at the surface is the most probable terminated phase at the surface. The bond-angle distortion of the *a*-SiO_2 at

the interface as shown in Table 6.1, shows a little deviation from the bulk *a*-SiO_2 , which is because it has more flexibility than the Ru layer. To confirm this result, we compared the *a*-SiO_2 slab stability by calculating the total energy of the un-relaxed and relaxed *a*-SiO_2. At the highest number of NBO, 7, the *a*-SiO_2 slab has the highest energy difference between the un-relaxed and relaxed states, indicating that high strain energy decreases the total energy of this model, which leads to the unstable configuration. The preferable configuration is dependent on the number of Si atoms at the interface because NBO is fully covered when one NBO corresponds to one Si atom. For four models, the number of Si at the interface is 5 or 6 atoms, which is consistent with the experimental result that indicates that the most probable OH group numbers is equivalent to the number of Si atom at the interface. To evaluate the partially terminated NBO, we select another configuration with 4 NBO, as shown in Model 3.

As shown in Table 6.1, the interfacial bond lengths are comparable to the values found in other calculations. The significant reconstruction at the interface is not observed in these models, but Model 1 is similar to the reference data [106], which means its structure is the most stable interface structure. The probable maximum number of NBO in my model is 4 due to the same number of Si atoms at the interface. Therefore Model 1 may be the most stable interface structure without much strain energy of the *a*-SiO_2 slab even though Model 4 has the highest number of NBO, which leads to high adhesion energy.

Table 6.1. Interfacial bond numbers and average bond length and angle of a relaxed Ru(0001)/ *a*-SiO_2

	No. of NBO(BO)	Ru-O(Å)	Si-O(Å)		O-O(Å)		O-Si-O(º)	
			present	exp[112]	present	ref.[113]	present	ref.[113]
Model 1	6(1)	2.079	1.619	1.61	2.992	3.00	108.3	109±6
Model 2	7(2)	2.126	1.579		2.589		110.4	
Model 3	4(3)	2.129	1.570		2.759		112.6	
Model 4	5(2)	2.143	1.636		2.566		101.9	

The shortest O-Ru distances across the interface for the structures in Fig. 6.1 are approximately 2.0~2.13 Å, as shown in Table 6.1. For comparison, the smallest bulk cation-cation lengths are *d* (Ru-Ru) = 2.73 Å in the Ru structure and *d* (Si-O) = 1.61 Å in the *a*-SiO_2 bulk structure. We also see that the Ru atom closest to the interface generally induces some distortion. This finding suggests a strong hybridization may have formed. To further investigate the bonding, we display the density of state and charge density difference in Section 6.3.3.

6.3.2 Adhesion energy

We calculate the adhesion energy for the four representative Ru/*a*-SiO_2 interface models. We explore the variation in adhesion energy as a function of the number of NBO. Before calculating the adhesion energy, we calculate the adsorption energy of non-bridging oxygen, which has 3.9 eV/atom on top of the Ru atom, suggesting that the binding energy is strong. In addition, the adsorption energy between the bridging oxygen and Ru is 0.5 eV/atom. Comparing the adsorption energy of NBO-Ru, the adsorption energy of bridging oxygen to Ru is very low, indicating that the bridging oxygen involves in adhesion with Ru atom to a small degree. Therefore, the adhesion energy increases upon increasing the number of NBO at the interface, as shown in Table 6.2.

The adhesion energy variation for *a*-SiO_2 forced into registry with the Ru atoms is significantly larger than that of Ru atoms. In reality, only partial registry at the *a*-SiO_2 /Ru interface is likely to be present due to the lattice mismatch between Ru and *a*-SiO_2. Our calculations suggest that high registry is expected with high adhesion energy but leads to high strain of the *a*-SiO_2, which may reduce the total energy of the interface model. The calculated adhesion energies and the strain energies of the *a*-SiO_2 and Ru are listed in Table 6.2.

Table 6.2. Adhesion energy for Ru/*a*-SiO_2 and strain energies of the *a*-SiO_2 and the Ru layers.

	E_{adh}	Strained of *a*-SiO_2	Strained of Ru
	J/m^2	J/m^2	J/m^2
Model 1	4.242	1.070	0.052
Model 2	4.624	1.465	0.009
Model 3	3.138	0.669	0.004
Model 4	4.047	1.139	0.011

We calculate adhesion energy that is needed to form the interfaces with Ru and *a*-SiO_2 surfaces by subtracting the energies calculated for the Ru and *a*-SiO_2 slabs, as described below:

$$E_{adh} = (E_{Ru/a-SiO_2} - E_{Ru} - E_{a-SiO_2})/A \quad (6\text{-}1)$$

where A is interface area; $E_{Ru/a-SiO_2}$ is the total energy of the total system; E_{Ru} and E_{a-SiO_2} are the total energies of the isolated Ru slab and *a*-SiO_2 slab, respectively. This adhesive energy includes not only the chemical bonding but also the interfacial strain contribution. The strain energy of *a*-SiO_2 is the difference between the energy of the isolated slab and the energy of the relaxed slab. Even though the *a*-SiO_2 slab is strained, arising from registry to the Ru layer, the adhesion energy has strong adhesive strength. The strain could deteriorate the adhesion in the crystalline system, but in the amorphous system, the strain could enhance the possibility of making NBO and registering with the Ru layer, which leads to a higher adhesive interface. The most probable interfacial geometry could be dependent on the number of NBO, which can stabilize the interface with low strain energy and high adhesive energy as shown in Model 2. We also verify the effect of the number of the NBO at the interface; just as the adhesion energies are exactly functions of the number of NBO. The highest number of NBO is 6, which is the most preferable model. However, depending on the interfacial geometry, two NBO with one Si bonding might occur because of the high adhesive energy between NBO and Ru even though the *a*-SiO_2 has small strain energy, as indicated in Model 2. For the lowest number of NBO,

shown in Model 3, the strain energy is lowest, which means that the slab does not need to register to Ru atoms to meet; instead, it remains in the preferable stable state like the state of the original *a*-SiO_2.

6.3.3. Electronic properties

To examine the charge transfer between the Ru and *a*-SiO_x layer, we calculate the charge density difference perpendicular to the slab structure. Fig. 6.2 shows the planar-averaged charge density difference for the four models. The charge density difference is evaluated by subtracting the sum of the isolated slab charge densities from the total interface charge density as is defined by;

$$\Delta\rho(z) = \rho_{IF}(z) - [\rho_{Ru}(z) + \rho_{SiOx}(z)], \quad (6\text{-}2)$$

where $\rho_{IF}(z)$, $\rho_{Ru}(z)$, and $\rho_{SiOx}(z)$ are the charge densities of the Ru/*a*-SiO_x interface, the Ru layers, and *a*-SiO_x substrate, respectively, averaged over the *xy* plane.

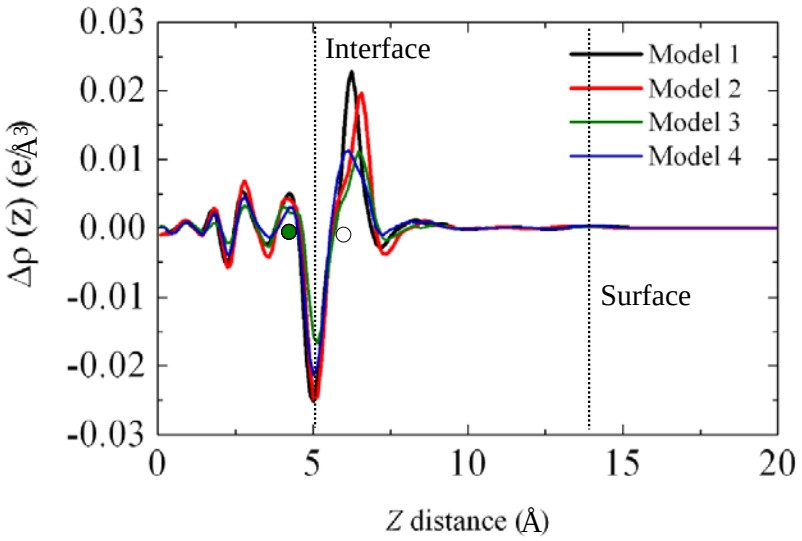

Figure 6.2. Planar-averaged charge density difference for the Ru/a-SiO_2 interface along a direction perpendicular to the interface. Solid circles give the location of the Ru atoms; open circles represent the oxygen atoms.

The charge density difference shows regions of charge depletion between the Ru layer and the oxygen layer with a charge of -0.017 ~ -0.025 e/Å^3, while the charge difference around the interfacial oxygen atoms gains a charge of +0.01 ~ +0.023 e/Å^3.

Table 6.3. Local charge transfer for the optimal O and Ru atoms at the interface compared with the middle layer of O and Ru atoms. The plus values indicate the electron loss, while the minus values indicate the electron gain.

	Interface	Middle layer		
	NBO (BO)	Ru	O	Ru
Model 1	-1.283 (-1.542)	0.277	-1.564	0.117
Model 2	-1.309 (-1.499)	0.248	-1.566	0.117
Model 3	-1.315 (-1.530)	0.200	-1.560	0.117
Model 4	-1.255 (-1.484)	0.285	-1.560	0.118

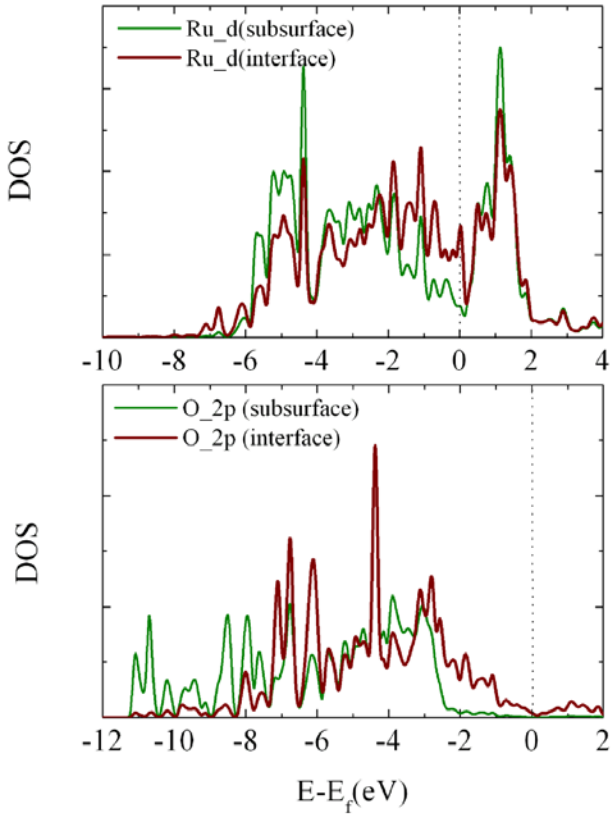

Figure 6.3. Site-projected, orbital-resolved local densities of states for Ru and O atoms at the Ru/*a*-SiO_2 interface.

The charge difference in Models 1 and 2 show significant charge transfer between Ru and NBO. The charge transfer in Models 3 and 4, which have 4 or 5 NBO at the interface, is not significant, suggesting that the charge transfer is strongly dependent on the number of NBO at the interface. The charge depletion represents the formation of an ionic bond between Ru and O atoms, which will be verified by subsequent analyses of the local electronic transfer by using the Bader method [72] and density of state analyses.
We perform a Bader analysis using the Bader code with high FFT grid in the VASP package. The first result made clear by our Bader analyses is that there is a net charge transfer from the Ru layer to the oxide

We find about 0.2 ~ 0.4 electrons (e)/atom transfer from the Ru layer to the oxide. Comparable to the middle oxygen, the NBO loses their electrons about 0.3e/atom. However, NBO continues to gain electrons at the interface. It is also interesting to note that the bridging oxygen at the surface lose their electrons with a charge of 0.02 ~ 0.08 e/atom, indicating BO affects the bonding between Ru and O at the interface, but the charge is very low. In addition, the second Ru layer affects the charge transfer at the bonding with aSiO_2 with a charge of 0.1 e/atom, which is also consistent with the result of charge density difference.

In order to further investigate the bonding, we display in Fig. 6.3 the site-projected local density of states (LDOS) for the interfacial Ru and O atoms. Figure 6-3 exhibits the Ru 3d and O 2p states. We see that the strong mixing occurs between O 2p and Ru 3d occupied states. Additionally the presence of corresponding antibonding states above the Fermi level suggests Ru-O covalent bonding. The strong mixing between Ru 3d and O 2p supports the idea that Ru-O bonding leads to strong adhesion between the Ru layer and *a*-SiO_2.

6.4 Summary

A theoretical method has been developed and applied to explain the variation in adhesion strength between the Ru(0001) and different content of NBO and BO of *a*-SiO2 substrate. This approach provides a basis for a fundamental understanding of mechanical

stability and adhesion properties of interfaces in barrier applications. This method is also useful for engineering better interfaces by selective investigations of heterogeneous and/or doped interfaces that would otherwise be expensive and time-consuming to do experimentally.

Chapter 7:

The Structure and Bulk Properties of Amorphous Co-P (cobalt - phosphorus) and Co-B (cobalt - boron) alloys

7.1 Introduction

Cobalt or cobalt-based alloys have been widely studied in the application of Cu IC, for example, Cu seed layer, barrier, and dielectric capping layer [114] because the Co or Co-based alloys provides several advantages such as high bonding strength with Cu, low bulk resistivity and low solubility in Cu. However, Co itself is a very poor barrier to Cu diffusion in the back-end fabrication process due to the existence of fact diffusion paths along the crystalline boundaries of Co films. Therefore, alloying the Co film is essential to overcome these disadvantages. Recently, Henderson et al., have grown the amorphous Co(P) film by chemical vapor deposition (CVD) and shows that films displayed good thermal stability, maintaining their amorphous nature [26-28].

Unlike the well defined crystalline structure, the atomic short and medium range order in amorphous alloys remains unclear. For instance, a metal-metalloid glass, in which the chemical short-range order is strong, is not well defined by Bernal's dense random packing of hard spheres [74]. The forming ability of amorphous alloy is strongly related to the short and medium range ordering, which is governed by the atomic size ratio and different chemistry. The details of how the atoms are packed in amorphous alloys and how the short and medium range ordering are related to the forming ability of amorphous alloys are far less understood.

To investigate the structure and stability of the amorphous Co-P alloy, we develop the amorphous Co-P alloy models with varying P content. Then, we analyze the short and medium range orders and calculate the energetic and chemical bonding properties.

Generally, the atomic size ratio and negative formation energy are considered to be the main parameters to promote the properties of amorphous alloys. To gain quantitative understanding the effect of atomic size ratio (λ) and different chemistry on the forming ability of amorphous alloy we employed boron (B), which is different in

atomic size and chemistry with P, in creating amorphous Co alloy as an alternative of *a*-Co-P alloy. In a different environment, we will elucidate how the short and medium range order affect the forming ability and alloy properties. Co or Co-based alloys are ferromagnetic. The magnetization of the ions, which is generated by the relative shift among the two spin populations, is due, to a large extent, to the *d* states. Thus, the same electrons which are responsible for the metallic behavior, also give rise to the magnetic properties of this material. Therefore, charactering the atomic arrangement in atomic scale disorder is strongly relying on electronic and magnetic properties.

In this chapter, we use well established methods based on first principles density-functional theory calculation to predict the 3D amorphous alloy structures and bonding properties of Co-P and Co-B alloys. In particular, we examine different types of short range orders and evaluate the electronic and magnetic properties amorphous $Co_{80}P_{20}$ and $Co_{86}B_{14}$ alloys.

Our findings provide realistic characterization of glassy structures but also a detail understanding of the origin of short range ordering of amorphous alloys.

7.2 Method

The calculations reported herein were performed on the basis of density functional theory (DFT) within the generalized gradient approximation (GGA-PW91 [65]), as implemented in the Vienna *Ab initio* Simulation Package (VASP) [21, 66, 106]. The projector augmented wave (PAW) method with a plane-wave basis set was employed to describe the interaction between ion cores and valence electrons. The PAW method is, in principle, an all-electron frozen-core approach that considers exact valence wave functions. Valence configurations employed are: $4s^2 3d7$ for Co, $3s^2 3p^3$ for P, and $3s^2 2p^1$ for B. A plane-wave cutoff energy of 300 eV is used and the Brillouin zone integration was performed using one k-point (at Gamma) for the molecular dynamical simulation and Co-P and Co-B structures used in our analysis, we begin by randomizing 72-Co atoms in a periodic supercell and then replaced a given fraction of Co with P or B. Next, the alloy was melted at high temperature (3,500 K) for 3 picoseconds (ps) with a time step of 1

femtosecond (fs), using *ab initio* molecular dynamic simulation (AIMD) within a Born-Oppenheimer frame work [115], and then quenched to 300 K at a rate of 1.5 K/fs, followed by static structural optimization. Here the temperature was controlled using velocity rescaling. The structures of crystalline Co-P and Co-B, as well as cobalt, phosphorus and boron, are summarized in Table 7.2 [116-121].

For further structural, electronic, and magnetic property analysis, the amorphous $Co_{80}P_{20}$ and $Co_{86}B_{14}$ alloy structures were modeled using 144-atoms (consisting of 115 Co and 29 P atoms in $Co_{80}P_{20}$, 124 Co and 20 B in $Co_{86}B_{14}$) in a periodic supercell volume of 1.6 nm^3 and 1.5 nm^3, respectively, at 0 K.

7.3 Results and Discussion

7.3.1 Bulk properties of the constituent system

The lattice constant is obtained by calculating the total energy for different unit cell volume. This method yields results identical to experimental values. Under ambient conditions, Co crystallizes in the hexagonal-close-packed (hcp) structure. Therefore, for further calculation, hcp Co structure will be used.

Table 7.1. Calculated equilibrium properties of Co both in hcp and fcc phase.

Phase		lattice constant a	c/a	Bulk modulus (GPa)	μ_B (per Co)
HCP	this work	2.52	1.63	196.1	1.77
(εCo)	exp.[a]	2.51	1.62	191.0	1.58
FCC	this work	3.58		206.0	1.64
(αCo)	exp.[b]	3.54		198.0	1.61

[a]: ref. [122], [b]:ref. [123-125]

7.3.2 Stability of amorphous CoP and CoB alloys

To examine the relative stability of amorphous versus ordered CoP and CoB alloys, we first calculated the total energy with varying composition ratios of P and B atoms particularly in the P(B) low content region (below 30 at. % of P and 20 at. % of B,

where the transition from a more stable crystalline to amorphous phase was found). The result, which is summarized in Fig. 7.1, demonstrates that the CoP (CoB) amorphous phase becomes energetically more favorable than its ordered counterpart when the P (B) content is above 20 (10) at. %. Here, the ordered alloys were calculated by replacing Co with P or B, starting with the hexagonal close packed structure of pure Co (with a lattice constant of 2.52 Å). Both ordered and amorphous alloys were modeled using a 72-atom supercell, and the atomic positions and the supercell volume were optimized to minimize the total energy.

Table 7.2. Calculated equilibrium properties of crystalline Co-P and Co-B compounds.

Phase	Space group	Lattice constants (Å)	Volume (Å^3)	#Co/P(B)	K-Points	Ref.
Co	P6-3/mmc(194)	a=2.495(2.507), c=4.037(4.070), γ=120	21.76	2/0	[15×15×15]	118
P	P2/c (13)	a=9.274,b=9.260, c=24.159, β=105.74	2009.85	0/84	[2×2×2]	
B	R-3m(166)	a=10.738,b=11.385,c=26.249	1062.56	0/141	[2×2×2]	
Co_2P	Pnma(62)	a=5.518(5.640),b=3.514(3.509),c=6.596(6.605)	127.89	8/4	[11×11×11]	120
CoP	Pnma(62)	a=5.076(5.065),b=3.275(3.276),c=5.556(5.579)	110.01	4/4	[11×11×11]	119
CoP_3	Im32(204)	a=7.735(7.707)	231.43	4/12	[11×11×11]	121
Co_3B	Pnma(62)	a=5.147(5.225),b=6.602(6.629),c=4.402(4.408)	149.55	12/4	[4×4×4]	116
Co_2B	I4/mcm(140)	a= 4.952 (5.016), c=4.241 (4.220)	106.18	8/4	[4×4×4]	117
CoB	Pbmn	a=5.166(5.253),b=3.060(3.043),c=3.914(3.956)	62.00	4/4	[4×4×4]	117

Fig. 7.2 shows the predicted volume change exhibiting a distinctive nonlinear trend for the Co-P alloy but a linear decrease for Co-B alloy. The Co-P alloy volume becomes a minimum at 25%, yielding the highest packing density, while the Co-B alloy volume decrease, leads to increased packing density as B content increases. This is largely due to the large atomic size difference between Co and B atoms. As expected, the crystalline phase is slightly denser than the amorphous alloy of corresponding composition. The smaller atomic size of B than P atom decreases the composition limit to form an amorphous structure.

For the sake of comparison, we also evaluated the crystalline-to-amorphous transition using the following universal correlation between glass formability and atomic volume ratio in a binary alloy [23]:

$$C_{min} = 0.1/|\gamma^3-1| \quad (7\text{-}1)$$

where C_{min} is the minimum concentration of solute element needed to produce the

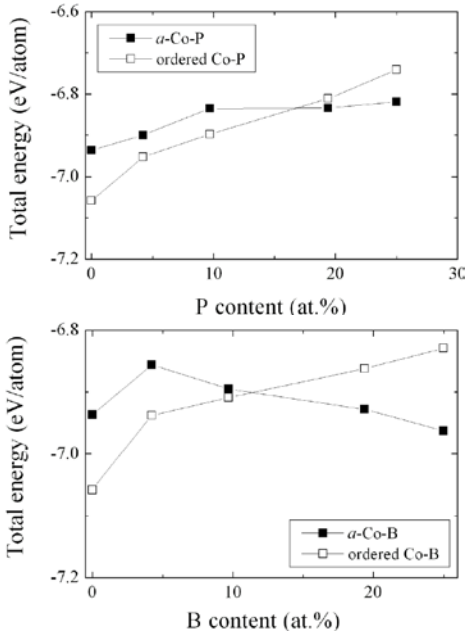

Figure 7.1. Variation in total energy for amorphous and crystalline Co-P and Co-B alloys as a function of P(B) content (at. %).

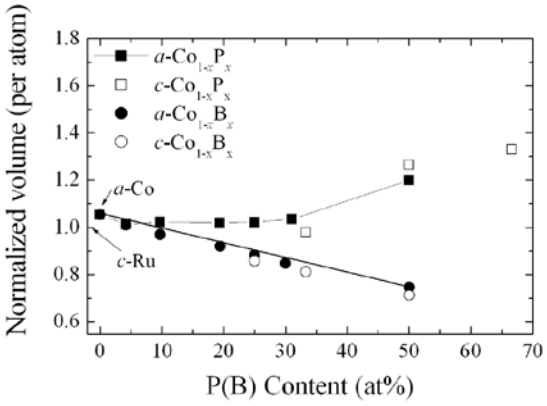

Figure 7.2. Variation in volume for *a*-CoP and *a*-CoB as a function of P(B) content (at%).

amorphous phase and γ (=R_b/R_a) is the radius ratio of the solute (R_b) to the solvent (R_a). The elastic model has been widely adopted in predicting the structural instability of a crystalline binary alloy (as a function of solute concentration) due to the size difference between solvent and solute atoms. Taking 1.251 Å [80], 1.06 Å [81], and 0.82 Å [82] for

Co, P, and B atomic radii, the required minimum concentrations for P (in an amorphous Co-P alloy) and B (in an amorphous Co-B alloy) are estimated to be 25.5 at. % and 13.9 at. %, respectively, which is somewhat closed to our DFT calculation results. These results unambiguously demonstrate that the amorphization of binary alloys is mainly driven by the elastic strain contribution arising from the atomic size difference between Co and P(B) atoms.

Fig. 7.3 shows a variation in the mixing enthalpy for amorphous and crystalline Co-P(B) alloys as a function of the Co:P(B) composition ratio, with respect to crystalline Co (*c*-Co) and crystalline P(B)(*c*-P(*c*-B)). The mixing enthalpy per atom (ΔE_{mix}) is given by:

$$\Delta E_{mix} = E(alloy) - (1 - x)E_{Co} - xE_{P(B)} \quad (7\text{-}2)$$

where *E(alloy)* is the total energy per atom of the Co-P alloy examined, *x* is the number fraction of P(B), and E_{Co} and $E_{P(B)}$ are the total energies per atom of crystalline *hcp* Co and P(B) (*c*-Co, *c*-P or *c*-B), respectively.

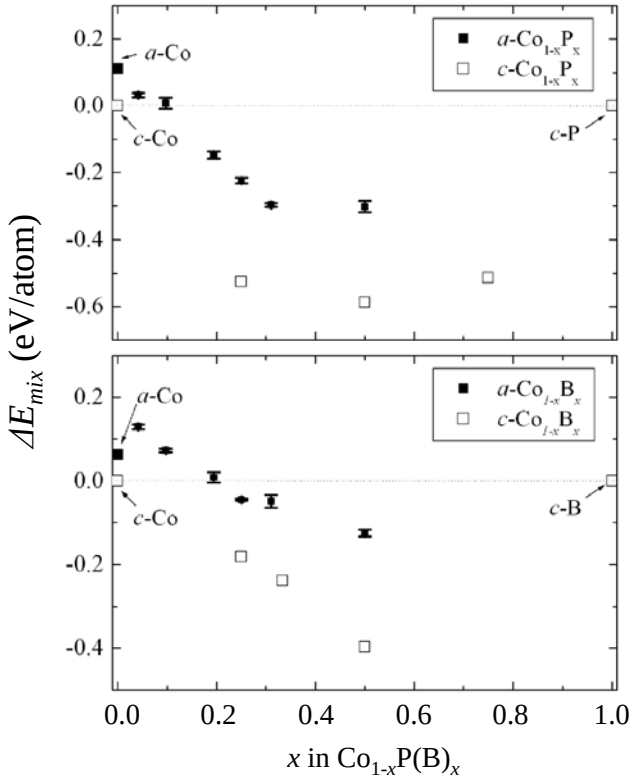

Figure 7.3. Variation of mixing enthalpy as a function of solute atoms.

The results indicate that the Co-P alloy forms the most favorable structure when the P content is around 40-60 at. %, with an energy gain of ~ - 0.3 eV/atom, while the mixing enthalpy for the Co-B alloy gradually decreases with increasing B content and exhibits a minimum value of ~ -0.2 eV/atom at 50 at. %. For the Co-P alloy, the large negative mixing enthalpies suggest that P atoms can easily be incorporated into the amorphous Co matrix above 20 at. % of P. This characteristic was also noticed in the previous study of amorphous CoP thin film, in which the measured P content for the amorphous film determined by X-ray photoelectron spectroscopy (XPS) shows approximately 13~28 at. % [26]. It is also noted that the mixing enthalpy become positive when the P content is small, which might indicate the presence of a barrier for incorporation of P into pure Co atoms.

For crystalline phases, a distinct mixing enthalpy minimum is found at 50 at.% P, and on average the total energies are ~ 0.3 eV/atom lower than their amorphous counterparts; hence *a*-Co-P alloys may undergo recrystallization at elevated temperatures, as evidenced by previous experiments, that showed 30 nm thick ~ 15 % alloy remained amorphous upon annealing at 635 K for 3 hr but crystallized upon annealing at 775 or 975 K [26] . The sizable energy gain of the *c*-CoP, relative to the $Co_{80}P_{20}$ structure, suggests that the Co-P alloys with a low P content (~ 20 at %) may undergo decomposition into *c*-Co and *c*-CoP during high temperature thermal treatment.

Based on the thermodynamic point of view, the amorphous structure forming ability is predicted by the comparison of the mixing enthalpy and mixing enthalpy difference between crystalline and amorphous phase. The lower the mixing enthalpy, the higher the glass forming ability, and the lower the mixing enthalpy difference between crystalline and amorphous phase, the higher the glass forming ability. Based on this correlation (3), the lower mixing enthalpy and lower mixing enthalpy difference for Co-P alloy than Co-B alloy may enhance the glass forming ability. This trend is consistent with both Co-P and Ru-P [126]. Higher annealing temperature of ~ 500 ^{0}C in CoP alloys to form crystallite than the temperature of ~ 350 ^{0}C in RuP alloys is strongly due to the lower resistance (ΔH^{inter}-ΔH^{amor}) to forming CoP alloy than RuP alloy.

$$\text{GFA } \alpha \frac{\Delta H^{amor}}{\Delta H^{inter} - \Delta H^{amor}} \quad (7\text{-}3)$$

7.3.3 Structure

To gain understanding of the structural stability and electronic structure relationship between constituent atoms, we explored the atomic distribution and electronic properties of selected $Co_{80}P_{20}$ and $Co_{86}B_{14}$ alloys.

We looked at the structural property of amorphous $Co_{80}P_{20}$ and $Co_{86}B_{14}$ alloys. Fig. 7.4 shows a set of the partial pair distribution functions from our simulations, together with corresponding crystalline structures for comparison. The amorphous structures were characterized using the pair distribution function (PDF, $g(r)$), which is defined as [26]

$$g(r) = \frac{V}{N} \frac{n(r)}{4\pi r^2 \Delta r} \quad (7\text{-}4)$$

where $n(r)$ represents particles in a shell within the region $r \pm \Delta r/2$, where Δr is the shell thickness; N denotes the number of particles in the model volume V.

The pair distribution function $g(r)$ was computed using a 144-atom supercell. No sharp second-neighbor peak is present, which confirms the amorphous nature (i.e., a lack of long-range order) of the Co-P and Co-B alloys.

Fig. 7.4a displays the calculated total X-ray PDF for *a*-$Co_{80}P_{20}$, which is almost identical to the crystalline Co_2P and are very similar to those obtained from the RDF from experimental X-ray scattering data for $Co_{78}P_{22}$ alloy [127]. Fig. 7.4b displays the calculated total X-ray PDF for *a*-$Co_{86}B_{14}$, which is also in good agreement with the crystalline Co_3B alloy, and compares it to experimental data of $Co_{81.5}B_{18.5}$ [128]. We can see that the calculated PDF is in good agreement with experimental data as well.

For the total pair distribution function, the *a*-$Co_{80}P_{20}$ and *a*-$Co_{86}B_{14}$ alloys show distinct amorphous character as an evidenced by the split second peak, where the average coordination number (CN) of Co around P and B are 9.31 and 9.35, respectively. For comparison, the CN of Co around P and B in *c*-Co_2P and *c*-Co_3B are both calculated to be 9 at cutoff radius of 3.1 Å. The first peaks in $g_{Co\text{-}Co}(r)$ of *a*-$Co_{80}P_{20}$ and *a*-$Ru_{86}B_{14}$ are

around 2.5 Å, which nearly corresponds to the lattice constant of HCP Co (2.52 Å). The partial pair distribution functions between Co and P(B), $g_{Co\text{-}P}(r)$ and $g_{Co\text{-}B}(r)$, are also shown in Fig. 7.3. The first peaks in *a*-$Co_{80}P_{20}$ and *a*-$Co_{86}B_{14}$ are 2.2 Å and 2.1 Å, respectively, and yield high intensity. This suggests the strong intermixing between the Co and P(B) atoms, namely, a strong chemical short-range order. For the partial pair distribution functions for P(B), the statistics for the $g_{P\text{-}P}(r)$ and $g_{B\text{-}B}(r)$ are not good comparing with the crystalline counterparts with CN = 0, but the small intensity of a partial peak and a calculated coordination number of 0.62 (at cutoff radius of 3.1 Å) and 0.40 (at cutoff radius of 3.1 Å) for P and B, respectively, describe the existence of dimers (P_2 and B_2). This result is similar to the model proposed in our previous result for the Ru-P and Ru-B alloys, which show strong short-range order with the negative mixing enthalpy [126].

From these features of $g(r)$, we can estimate that the structures of the amorphous alloys are governed by a chemical ordering effect due to the chemical interaction between the Co and the P(B) atoms.

(a)

(b)

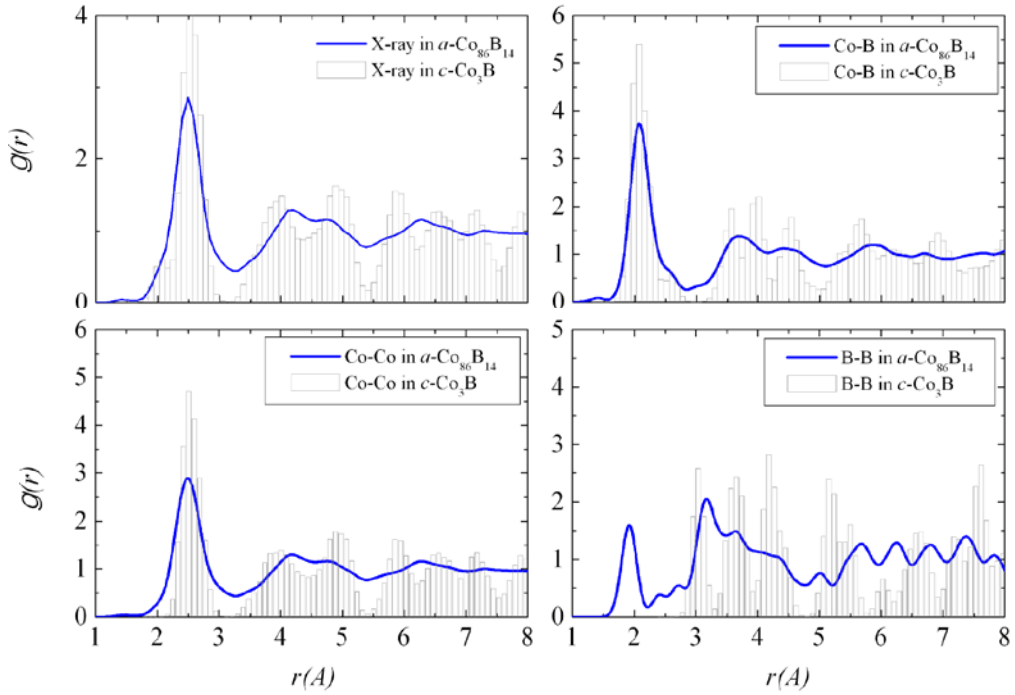

Figure 7.4. Partial pair distribution function, g(r), of the *a*-$Co_{80}P_{20}$ (a) and *a*-$Co_{86}B_{14}$ (b) alloys at the ground state.

7.3.4 Voronoi analysis

Disordered atomic configurations are used to explore the short and medium range details by using the tessellation method [55, 56], which characterizes the local atomic environment. The CoP or CoB alloy with a moderate P or B content results in a glassy structure exhibiting a distinct topological and chemical short-range order. The type of coordination polyhedron around a P(B) atom can be specified using the Voronoi index <*i*3,*i*4,*i*5,*i*6,…>, where *i*n indicates the number of n-edged faces of the Voronoi polyhedron and Σ*i*n is the total CN, to designate and differentiate the type of coordination polyhedron surrounding the center of solute atoms. For *a*-$Co_{80}P_{20}$ structure (Fig. 7.5a), the solute coordination polyhedra form the mono-capped square Archimedean antiprism (slightly distorted from the tri-capped trigonal prism packing (TTP)), which corresponds to a Voronoi index of <0,5,4,0>; and CN(Coordination number) 10 polyhedra, which is a

Voronoi index of <0,4,6,0>. For *a*-$Co_{86}B_{14}$ structure (Figure 5b), the solute coordination polyhedra form the TTP (tri-capped trigonal prism packing), which corresponds to a Voronoi index of <0,3,6,0> and the CN 10 polyhedra with Voronoi index of <0,2,8,0>.

Voronoi analysis indicates that the average coordination number is 9.8 for the $Co_{80}P_{20}$ alloy, and 9.3 for the $Co_{86}B_{14}$ alloy, which corresponds to the average CN calculated from the integration of PDF first peak.

It is well known that the preference polyhedra and CN are governed by the effective atomic size ratio, λ between solvent and solute atoms [76]. For instance, an earlier study shows that with decreasing λ, the preferred polyhedra changes from the Frank-Kasper type (for λ >1.2) to the icosahedral type (λ =0.902), and then to the BASP type (λ =0.835), and then to the TTP type (λ = 0.732). Considering the dominant CN of 10 in the $Co_{80}P_{20}$ alloy, we can expect that the polyhedron with a Voronoi index of <0,4,6,0> is similar to that found in $Ni_{80}P_{20}$, while the polyhedron, <0,3,6,0> found in the $Co_{86}B_{14}$ alloy, which has the CN of 9, is also a part of polyhedra found in $Ni_{81}B_{19}$ alloy [76].

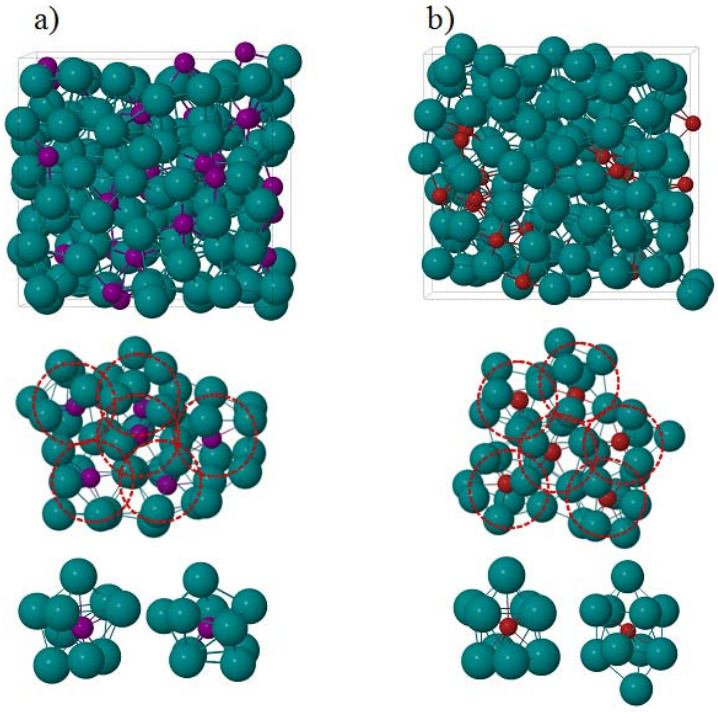

Figure 7.5. The packing of the solute atoms-centered clusters with an icosahedral ordering of the (a) CoP and (b) CoB alloys.

As is also shown in Fig. 7.5a and 7.5b, the formation of 'quasi-equivalent' P- and B-centered Co clusters arising from topological and chemical short-range order is also likely to lead to the medium- range order in the binary alloy. In fact, the short-to-medium range order is seen in other metallic glasses, particularly in transition metal-metalloid and transition metal-transition metal systems where the chemical short-range-order is significant [75, 85, 86].

7.3.5 Electronic and magnetic properties

To incorporate the chemical effect in Co-P and Co-B alloys, electronic interaction analysis between Co and P(B) atoms is performed. Here, we explore the nature of those bonds in terms of their electronic structures. Bulk bonding is dominated by the strong intermixing between the Co d-orbital and the P p-orbital. The p-d bonding is most clearly seen in the electronic density of states (DOS). The Fermi level is used as the reference energy state. In the partial DOS in Fig. 7.6a, the peaks of occupied state densities between -7.0 ~ -4 eV mainly originate from the P 3p and Co 3d intermixing, resulting in high degree of Co 3d and P 3p hybridization. It is apparent that the strong p-d hybridization mainly contributes to stabilizing the *a*-$Co_{80}P_{20}$ alloy structure. It is also noticed that the DOS of P atom accumulated at the Fermi level indicates the metallic character.

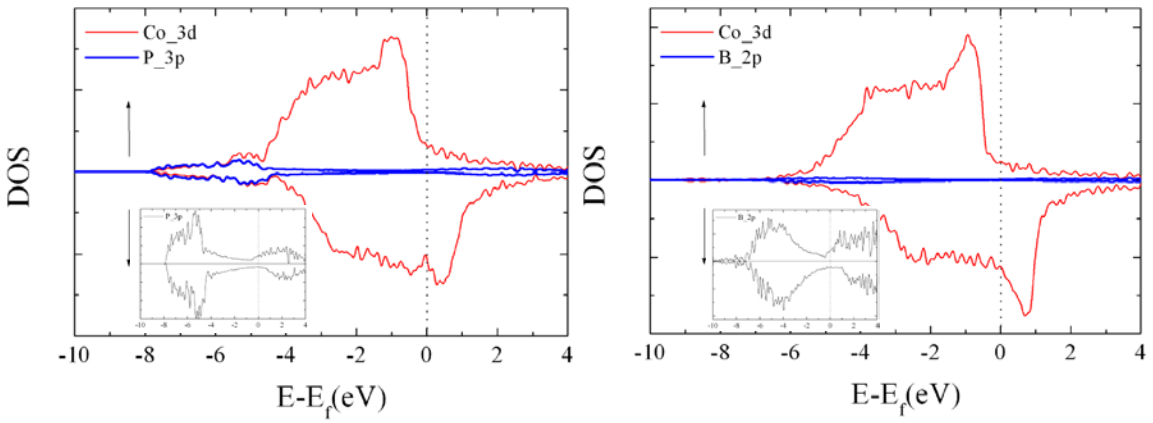

Figure 7.6. Site and spin projected density of states (DOS) of spin polarized *a*-$Co_{80}P_{20}$ (a) and *a*-$Co_{86}B_{14}$ (b) alloys.

The calculated DOS for the a-$Co_{86}B_{14}$ alloy as shown in Fig. 7.6b shows no gap at the Fermi level, also indicating the metallic character. In the energy range between -4 eV and -7 eV, Co 3d – B 2p hybridization can be observed. However, its intensity of intermixing is relatively lower than that of CoP, implying that the Co and B tend to be less attractive.

The magnetization is determined by the energy shift between spin up (↑) and down (↓) populations. The magnitudes of spin splitting are proportional to the magnetic moments. The magnetization is described in terms of Bohr magneton (μ_B). The Bohr magneton of Co in hcp (εCo) and fcc(αCo) are given in Table 7.1. The P and B contents in the *a*-Co-P and *a*-Co-B alloys affect the stabilities against crystallization as well as some of their magnetic properties. The Bohr magnetons of *a*-Co-P and *a*-Co-B alloys decrease as P(B) content increase as shown in Fig. 7.7. Co-P alloy result agrees well with the experimental data [127]. The magnetic moment of CoP alloy more rapidly decreases than that of Co-B alloy as the solute content increases due to the filling of the Co (3d ↑), suggesting that P atom may enhance the chemical interaction with Co while B atom remains in its isolated character. The sizable different μ_B between *a*-$Co_{70}P_{30}$ and *c*-Co_2P indicates that the charge filling of Co from the P may be restricted by the disordered structure in amorphous phase. However, the Co-B alloys do not show the different μ_B between crystalline and amorphous phases, meaning that the charge filling of Co from B is not significant with regards to the structure disordered. In addition, the B is not involved much in charge filling to the Co atom as an evidence of the higher μ_B than the values in Co-P alloys. Our calculations support that the magnetic moment of amorphous *a*-Co-P and *a*-Co-B alloys decrease nearly proportional to P(B) content until ~ 30 at. % and abruptly reach to zero at around ~ 50 at. % of P(B). In addition, *a*-$Co_{80}P_{20}$ and *a*-$Co_{86}B_{14}$ alloys are ferromagnetic. As also shown in Table 7.3, the magnetic moments per Co atom of crystalline phases at 0 K decrease with increasing P (B) content. Cop, CoP_3, and CoB are all diamagnetic as evidenced by the absence of magnetization.

Table 7.3. Calculated Bohr magnetons (μ_B) of crystalline Co-P and Co-B alloys.

Phases	Co_2P	CoP	CoP_3	Co_3B	Co_2B	CoB	*a*-Co[a]
μ_B (per Co)	0.21	0.0	0.0	1.20	1.03	0.0	1.86

[a]: amorphous Co.

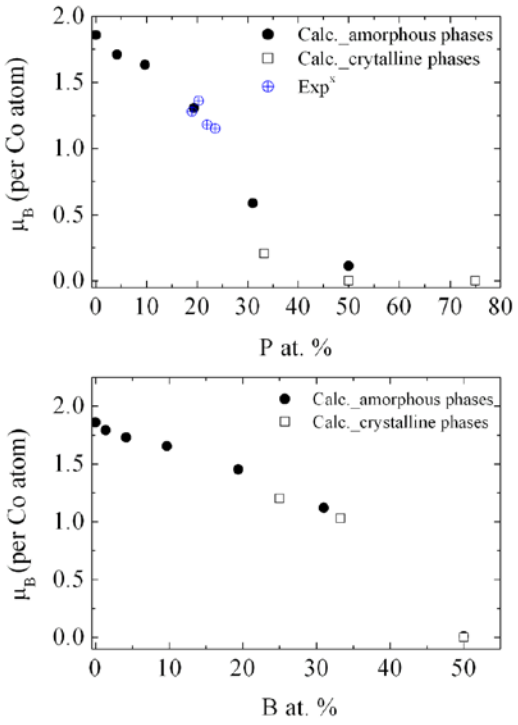

Figure 7.7. Magnetization in Bohr magnetons per Co atom for (a) Co-P alloys and (b) Co-B alloys.

7.4 Summary

Our *ab initio* molecular dynamics (AIMD) study shows that Co-P and Co-B alloys with moderate P (B) content can result in glassy structure exhibiting the topological and strong chemical short and medium range order.

Amorphous phases above ~20 at. % of P and ~ 10 at. % of B are energetically more favorable in the P(B) low content region than the crystalline counterparts for Co-P and Co-B alloys, respectively. In the region where the crystalline phases of Co-P and Co-

B alloys exist, the sizable energy gain of crystalline phases are more favorable than the amorphous phases, however amorphous phases tend to remain as itself due to the negative mixing energy.

In the $Co_{80}P_{20}$ structure, the P-centered polyhedra prefer the TTP phase with Voronoi index <0,4,6,0>, while in the $Ru_{86}B_{14}$, the B-centered polyhedra prefer the <0,3,6,0>. In addition, the Co-P and Co-B systems show the icosahedral medium range ordering arising from packing the 'qusai-equivalent' P-centered (B-centered) clusters in three dimensional spaces. We have also studied the electronic and magnetic properties of amorphous Co-P and Co-B alloys. The p-d hybridization between Co and P(B) is dominant in both alloys, and the amorphous $Co_{80}P_{20}$ and $Co_{86}B_{14}$ are all ferromagnetic with magnetic moments of ~ 1.3 and ~ 1.5 μ_B/Co atom, respectively. Our findings provide insight into the nature of local packing in Co-P and Co-B amorphous structures and understanding of the electronic and magnetic properties arising from the short and medium range orders.

Chapter 8:
On the Nature and Behavior of Li atoms in Si

8.1 Introduction

Silicon-based materials have recently emerged as a promising candidate for anodes in lithium-ion batteries because they exhibit a higher energy-storage capacity than the conventional graphite anode. Silicon (Si) has a theoretical lithium (Li) capacity of $Li_{4.4}Si \approx 4200$ mAh/g, which is more than ten times greater than that of graphite (372 mAh/g) [29, 31, 129]. Moreover, Si is safer, less expensive, and far more abundant than graphite. However, the practical use of Si as an anode material is hampered by its low intrinsic electrical conductivity and poor cycling performance [32-35]. In particular, the volume changes up to 400 % during lithiation and delithiation can cause severe cracking and pulverization of the Si electrode and consequent capacity fading arising from the loss of electrical contacts. Considerable efforts have been made to overcome these problems, for instance, through structural modifications such as amorphous phases [36, 37, 130], nanoparticles [38, 39], nanowires [40] and alloying with active/inactive elements such as silicon-tin [41] and silicon-metal [42-46] composites. In addition, first principles calculations have recently been applied to investigate fundamental aspects of the structural changes and lithiation behavior of Si-based materials, yet many of which still remain unclear.

Recent studies [47-52] have provided evidence for the formation of various stable Li silicide crystalline phases such as $Li_{12}Si_7$, Li_7Si_3, $Li_{13}Si_4$, $Li_{15}Si_4$, and $Li_{22}Si_5$ during high-temperature lithiation. The Li-rich LiSi alloys no longer exhibit a continuous Si tetrahedral network; instead containing discrete Si fragments (Si_n, $n \leq 5$) depending on the Li/Si composition ratio. While the Si network can be easily disintegrated by lithiation, it has also been reported that the lithiated Si at room temperature tends to exhibit no crystalline phases [6], possibly because of a kinetic barrier to crystallization. The kinetic effect can be more important at the onset of lithiation because the introduction of Li into a rather rigid Si network would be thermodynamically more unfavorable and thus the

lithiated structure of Si would be more kinetically controlled, compared to a highly flexible Li-rich LiSi alloy. However, thus far there has been no comprehensive study as to the dynamic behavior of Li in Si-based materials and also the influence of Li introduction on the stability of the host lattice, particularly in the early stages of lithiation.

In this chapter, we examine the structure, diffusion, and interaction of Li atoms in Si and how Li incorporation affects the nature of the Si bonding network using density functional theory calculations. We first present the atomic structure, stability and bonding mechanism of interstitial Li in crystalline Si (*c*-Si). The result also shows how Li introduction leads to weakening of nearby Si-Si bonds in *c*-Si. Next, Li diffusion rates and Li-Li interactions in the neutral and positive charge states are estimated. The calculation results provide some insight into the dynamic behavior of Li atoms and the effect of Li incorporation on destabilization of the Si lattice, particularly in the early stages of lithiation.

8.2 Computational methods

The calculations reported herein were performed on the basis of density functional theory (DFT) within the generalized gradient approximation (GGA-PW91 [65]), as implemented in the Vienna *Ab initio* Simulation Package (VASP) [131]. Spin polarization of the Li/Si system was also examined, but appears to be zero. The projector augmented wave (PAW) method with a planewave basis set was employed to describe the interaction between ion cores and valence electrons. The PAW method is, in principle, an all-electron frozen-core approach that considers exact valence wave functions. Valence configurations employed are: $1s^2\ 2s^1$ for Li and $3s^2\ 3p^2$ for Si. An energy cutoff of 300 eV was applied for the planewave expansion of the electronic eigenfunctions. The Si host is modeled using a 216-atom supercell with a fixed lattice constant of 5.457 Å; the effect of volume relaxation was also checked, and turns out to be unimportant as the 216-atom supercell is large enough to accommodate one or two Li atoms with no significant volume change (less than 1%). For geometry optimization and energy calculations, all atoms were fully relaxed using the conjugate gradient method

until residual forces on constituent atoms become smaller than 5×10^{-2} eV/ Å; but the convergence criterion was tightened to 1×10^{-6} eV for vibrational frequency calculations. A (2×2×2) k-point mesh in the scheme of Monkhorst-Pack was used for the Brillouin zone sampling [111]. Diffusion pathways and barriers were determined using the climbing-image nudged elastic band method (*c*-NEBM) with eight intermediate images for each hopping step.

8.3 Results and Discussion

8.3.1 Structure and stability.

First we determined the atomic structure and stability of interstitial Li in *c*-Si in the neutral (Li^0) and positive (Li^+) charge states. For both charge states, the tetrahedral (T) interstitial configuration (see the illustration above Table 8.1) is identified to be energetically the most favorable configuration.

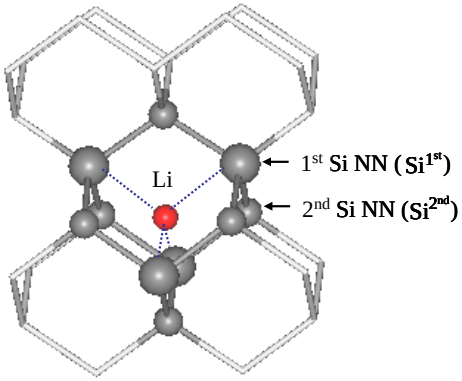

	Relaxed		Unrelaxed
	Li^0/*c*-Si	Li^+/*c*-Si	Li/*c*-Si
Li–Si^{1st}	2.46	2.45	2.36
Li–Si^{2nd}	2.75	2.75	2.75
Si^{1st}–Si^{1st}	4.01	3.99	3.86

Table 8.1. Optimized distances (in Å) between the Li interstitial and neighboring Si lattice atoms for both positive and negative charge states. For comparison, corresponding distances are also presented before the Si lattice relaxation. This clearly demonstrates an outward relaxation of the four Si first neighbors upon the Li insertion.

The Li insertion at the T site leads to a slight outward relaxation of the four Si first neighbors, i.e., 0.08 (0.07) Å displacement from their crystalline positions in the neutral (positive) case.

We examined other possible minimum-energy configurations for a Li interstitial. The hexagonal (H) state that is often another important local minimum for some interstitial atoms such as Si turns out to be a saddle point as detailed later. The <110>-split state in which Li and Si atoms are aligned in the <110> direction while sharing a lattice site also appears to be unstable, while the <110>-split dumbbell structure has been identified to be energetically most favorable for neutral Si and positively charged As-Si interstitial pair.[31] In addition, our calculation confirmed that the <111> bond-centered state in which Li is located between two lattice Si atoms while the lattice Si atoms are substantially displaced outward in the <111> direction is highly unlikely.

Fig. 8.1 shows the relative formation energy of Li^+ with respect to Li^0 at the T site, which is computed by $E_f^+ - E_f^0 = q(\varepsilon_F - \mu_i)$. The Fermi level ($\varepsilon_F$) is given relative to the valence band maximum (E_V). The ionization level (μ_i) is approximated by $E^+ + (E_v^+ + \mu_i) = E^0$, where E^+ and E^0 refer to the total energies of the positive and neutral states of the Li-containing supercell, and E_v^+ is the position of the valence band maximum in supercell E^+. In the periodic approach, a homogeneous background charge is included to maintain the overall charge neutrality of a charged supercell. Hence, to account for the electrostatic interaction with the background charge, a monopole correction was made to the total energy of the charged system [132]. For a point-like +1 charge in the 216-atom Si supercell, the monopole correction is approximated to be 0.11 eV. This approach seems to be reasonable considering the estimated charge state of Li^+ is +0.83 (*vide infra*), while the correction might be larger than the required adjustment if the charge on the impurity is significantly delocalized.

The predicted first donor (+/0) level is located near the conduction band minimum (E_c), i.e., E_c – 0.02 eV for the computed Si bandgap of 0.62 eV. The result suggests that Li interstitials might act like a shallow donor in *c*-Si. This is not surprising considering that Li has one valence electron ($[He]2s^1$) with a low electronegativity of 0.98, and can

thereby be easily ionized via electron donation to the Si matrix (whose electronegativity is roughly scaled at 1.90). Our DFT-GGA calculations as a whole agree well with previous experiments [133] demonstrating that a Li atom introduced to *c*-Si remains at an interstitial site with T_d symmetry and behaves similarly to group-V shallow donors.

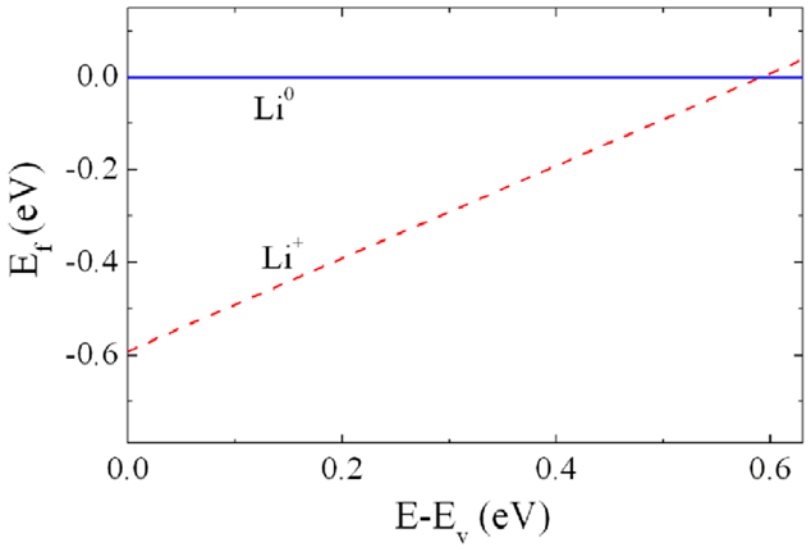

Figure 8.1. Variation in the relative formation energy of Li^+ with respect Li^0 as a function of the Fermi level (ε_F) relative to the valance band maximum (E_V) for the computed Si gap of 0.62 eV.

8.3.2 Bonding mechanism

The amount of electron transfer from the inserted Li^0 to the Si matrix is estimated to be 0.83e from the grid-based Bader charge analysis [72], special care was taken to ensure convergence with respect to the grid size. Likewise, in the positive charge system (Li^+), the Li charge state is also estimated to be +0.83. Analysis of the electronic density of states (DOS) for the Li^0/Si system [Fig. 8.2(a)] shows a shift of the Fermi level above the conduction band minimum of Si (while there is no noticeable change in the Li^+/Si case [Fig. 8.2(b)]). This indicates that the transferred charge from Li^0 partially fills the anti-bonding sp^3 state of neighboring Si atoms, which in turn weakens corresponding Si-Si bonds. The results clearly support that the Si network can be destabilized by lithiation,

leading to the formation of various Si-Li alloy phases as also evidenced by earlier experiments [47-50].

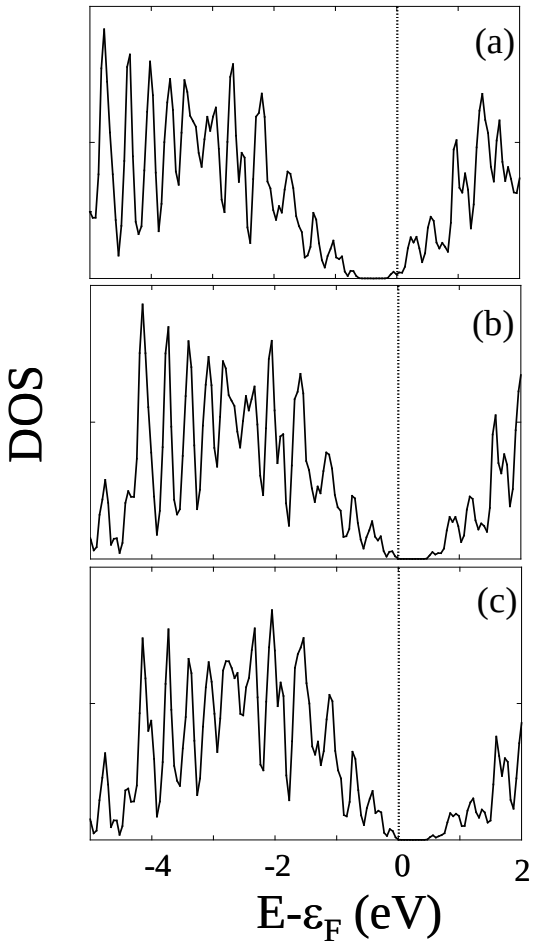

Figure 8.2. Electronic density of states (DOS) for the host Si matrix with (a) Li^0, (b) Li^+, and (c) no Li. The vertical dotted line indicates the Fermi level (ε_F) position.

We analyzed the bonding mechanism for Li^0 in the T configuration by calculating charge density differences before and after the Li insertion. As presented in Fig. 8.3, our calculation demonstrates charge accumulation in the region between the Li and each of its four nearest Si neighbors with a noticeable shift towards the Si atom. This suggests that the Si-Li bond can be characterized by polar covalent. Another important feature is that electron densities are noticeably depleted in the nearby Si-Si covalent bonding

regions, especially between the first and second nearest Si atoms. The charge depletion in the middle region between two Si-Si atoms is indicative of a weakening of its covalent bond, as also demonstrated by the aforementioned LDOS analysis. In addition, the charge density difference plot in Fig. 8.3 shows that the charge transferred from the Li^0 is largely localized within the first nearest Si lattice atoms, which in turn effectively screens the positively ionized Li interstitial.

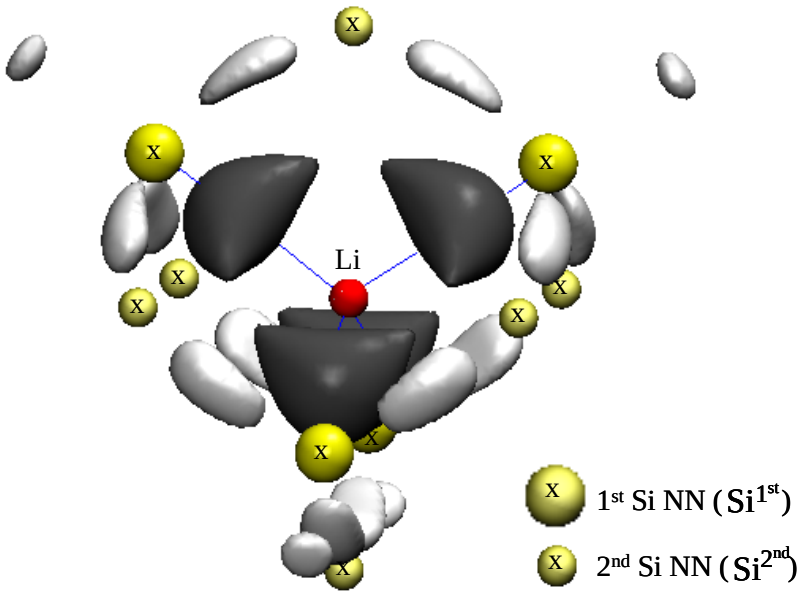

Figure 8.3. Valence charge density difference plot for Li^0 insertion. The charge density difference ($\Delta\rho$) is calculated by subtracting the charge densities of an isolated Li^0 and the Si matrix (with no Li^0) from the total charge density of the Li^0/Si matrix with no atomic displacement, i.e., $\Delta\rho = \rho(Li^0/Si) - \rho(Li^0) - \rho(Si)$. The positions of the Li, and its first and second Si nearest neighbors (NN) are indicated. The dark gray and light grey isosurfaces represent the regions of charge gain (+0.019 e/Å^3) and loss (-0.012 e/Å^3), respectively.

8.3.3 Diffusion.

As illustrated in Fig. 8.4, a Li interstitial may undergo migration by jumping between adjacent T sites via the H site which turns out to be a saddle point. The transition H state

is predicted to be 0.60 (0.62) eV above the local-minimum T state in the neutral (positive) charge state, which is close to 0.58 eV for Li^+ from previous calculations [134].

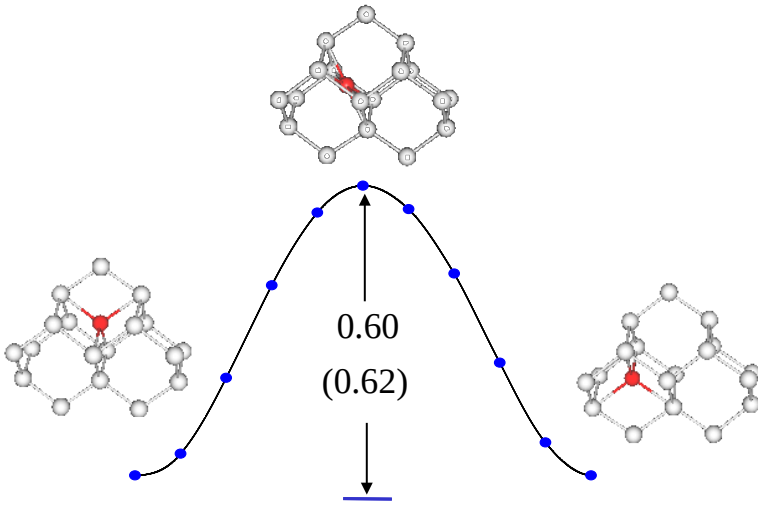

Figure 8.4. Predicted diffusion path for Li in *c*-Si. The energy variation is given in eV; the diffusion barriers for Li^0 and Li^+ are predicted to be 0.60 eV and 0.62 eV, respectively. The black (red) and light grey balls represent Li and Si atoms.

We evaluated the temperature-dependent diffusion coefficients of Li^0/Li^+ using the Arrhenius equation, $D = D_0 \exp(-E_a/k_BT)$, where E_a refers to the activation barrier for diffusion, k_B is the Boltzmann constant, and T is the temperature. Within harmonic transition state theory, the prefactor (D_o) can be derived by $D_0 = (1/2\alpha)\ \lambda l^2 \nu_0$, where α is the dimensionality of the diffusion space (which is 3 in the three-dimensional system considered), λ is the number of equivalent diffusion paths, l is the jump length between two adjacent local minima, and ν_0 is the attempt frequency [135, 136].

For the T → H → T diffusion event, there are four equivalent routes with a jump length of 2.36 Å. Using the Vineyard equation [135], we can estimate the attempt frequency ν_0 by: $\nu_0 = \prod_{i=1}^{3N} \nu_i^* \Big/ \prod_{i=1}^{3N-1} \nu_i^{**}$, where ν_i^* and ν_i^{**} are the harmonic vibrational frequencies at the minimum and saddle points, respectively.

Table 8.2. Predicted values of the attempt frequency (ν_0) and activation energy (E_a) for Li diffusion. Here, the prefactor (D_0) and diffusivity (D) are estimated by: $D_0 = (1/2\alpha)\ \lambda l^2\ \nu_0$ where α is the dimensionality of the diffusion space (which is 3 in the three-dimensional system considered), λ is the number of equivalent diffusion paths, and l is the jump length between two adjacent minima; and $D = D_0 \exp(-E_a/k_BT)$, where k_B is the Boltzmann constant and T is the temperature. Previous calculation and experimental values available in the literature are also presented for the sake of comparison.

		ν_0 (THz)	E_a (eV)	D_0 (10^{-3} cm^2/sec)	D (at 298 K) (10^{-13} cm^2/sec)
This work	Li^0	8.59	0.60	3.19	2.27
	Li^+	8.57	0.62	3.18	1.04
Cal[a]	Li^+	10.11	0.58	3.72	5.78
Exp[b]	Li^+		0.57 – 0.79	1.9 – 9.4	~17.9

a: Ref. [134], b:Ref. [137].

The vibrational frequencies were determined by diagonalizing a Hessian matrix obtained from numerical differentiation of forces that were calculated by displacing 28 non-frozen atoms surrounding the diffusing Li in the $\pm x$, $\pm y$, and $\pm z$ directions by 0.02 Å. At the saddle point, there was one imaginary frequency at around 307i cm^{-1} for Li^0 (312i cm^{-1} for Li^{+1}).

As summarized in Table 8.2, ν_0 and D_0 for Li^+ diffusion are estimated to be 8.57 THz and 3.18 ×10^{-3} cm^2/sec, in good agreement with ν_0 = 10.11 THz and $D_0 = 3.72 \times 10^{-3}$ cm^2/sec from previous calculations [134]. For the Li^0 case, ν_0 and D_0 values are estimated to be 8.59 THz and 3.19×10^{-3} cm^2/sec, close to the Li^+ case. Taking the prefactors and activation barriers, Li diffusion coefficients are estimated to be $D = 1.04 \times 10^{-13}$ cm^2/sec and 2.27×10^{-13} cm^2/sec at 298 K in the positive and neutral charge states, respectively. The predicted diffusivities are close to previous theoretical results (e.g., 5.78×10^{-13} cm^2/sec for Li^+) [134] and also within the range of experimental values reported in the literature (2×10^{-14} cm^2/sec) [137].

8.3.4 Li-Li interaction.

Finally, we looked at the interaction between two Li^0 interstitials in *c*-Si. Fig. 8.5 shows the variation in the relative energies with respect to the fully separated state [(d)] for various Li-Li distances; one Li was at a T site and the other was placed at the first [(a)], second [(b)], or third [(c)] nearest T site. The relative energies for (a), (b), and (c) are 0.19 eV, 0.06 eV, and 0.04 eV higher compared to (d). The total energy increase with decreasing the Li-Li distance is apparently caused by the repulsive interaction between the positively ionized Li interstitials; however, the force of repulsion tends to rapidly diminish as a result of effective screening as discussed earlier. Owing to the repulsive interaction, the diffusion barrier for (a) → (b) is lowered to 0.45 eV, as opposed to 0.6 eV for the non-interacting case. This finding also implies that Li interstitials favorably remain isolated, rather than clustered, at sufficiently low concentrations. For comparison, we also looked at the Li^+-Li^+ interaction; the result looks similar to the Li^0-Li^0 case, as presented in Fig. 8.5.

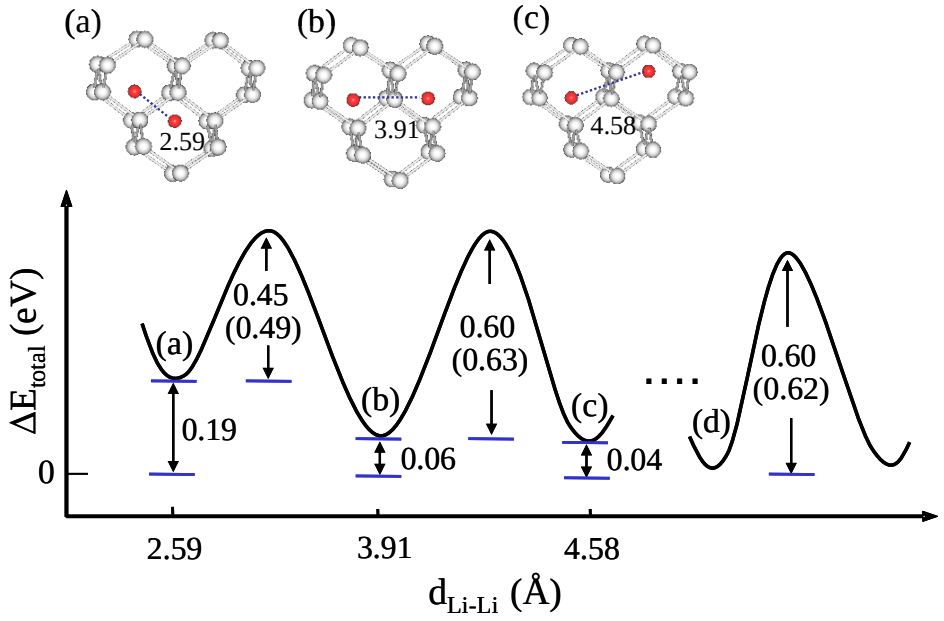

Figure 8.5. Variation in the total energy as a function of the distance between two Li^0 interstitials with respect to the fully separated state [(d)]. The black (red) and light grey balls represent Li and Si atoms. For comparison, diffusion barriers for the Li^+-Li^+ case are also presented in parenthesis.

Our calculations also show that the Li-Li distances are 2.59 Å, 3.91 Å, and 4.58 Å respectively for the (a), (b), and (c) cases, which are larger than 2.36 Å, 3.86 Å, and 4.52 Å for corresponding first, second, and third nearest T sites in *c*-Si (with no Li interstitial). This is not surprising considering the volume expansion of the Si structure upon Li introduction. The results clearly demonstrate that lithiation will rather easily lead to destabilization of the host Si network and subsequent formation of new Si-Li alloy phases, accompanied with significant volume expansion.

8.4 Summary

Using DFT-GGA calculations we examined the structure, stability, diffusion, and bonding mechanism of a single Li interstitial atom in *c*-Si in the neutral and positive charge states. We also looked at the interaction between two Li interstitials and the effect of Li incorporation on the stability of the Si lattice. For both Li^0 and Li^+, the tetrahedral (T) state turns out to be energetically most favored. The first donor (+/0) level is predicted to be at E_c – 0.02 eV for the computed Si bandgap of 0.62 eV, suggesting that interstitial Li would act as an effective donor in *c*-Si. Our DFT calculation shows that interstitial Li may undergo diffusion with a moderate barrier of ≈ 0.6 eV. Taking the computed prefactor of ≈ 3×10^{-3} cm^2/sec, the Li diffusion coefficient is estimated to be on the order of 10^{-13} cm^2/sec at room temperature, while there is no significant difference between Li^0 and Li^+. We find that the interaction between Li^0 interstitials is repulsive due to their positive ionization; the placement of two Li^0 atoms at adjacent T sites is 0.19 eV less favorable compared to when they are fully separated. This implies that Li interstitials favorably remain isolated, rather than clustered. The incorporation of Li^0 at the T site results in noticeable outward displacement of the four Si first neighbors by 0.08 Å from their crystalline positions. Our calculation also shows that the charge transferred from Li^0 is largely localized within the first nearest Si lattice atoms, which in turn effectively screens the positively ionized Li interstitial. Our analysis of electronic density of states (DOS) highlights that the electron transfer leads to partial filling of the anti-bonding *sp3* states of neighboring Si atoms, which in turn weakens corresponding Si-Si

bonds. This also clearly indicates that the host Si lattice can be easily destabilized by Li insertion. The fundamental findings assist in understanding the dynamic behavior of Li atoms and the nature of their interaction with the host Si matrix, particularly during the early stages of lithiation.

Chapter 9:
The Structure and Properties of Li-Si Alloys

9.1 INTRODUCTION

Silicon-based materials have recently emerged as a promising candidate for anodes in lithium-ion batteries because they exhibit a higher energy-storage capacity than the conventional graphite anode. Silicon (Si) has a theoretical lithium (Li) capacity of $Li_{4.4}Si \approx 4200$ mAh/g, which is more than ten times greater than that of graphite (372 mAh/g) [29, 31, 129]. Moreover, Si is safer, less expensive, and far more abundant than graphite. However, the practical use of Si as an anode material is hampered by its low intrinsic electrical conductivity and poor cycling performance [32-35]. In particular, the volume changes up to 400 % during lithiation and delithiation can cause severe cracking and pulverization of the Si electrode, and consequent capacity fading arising from the loss of electrical contacts. Considerable efforts have been made to overcome these problems, for instance, through structural modifications such as amorphous phases [36, 37, 130], nanoparticles [38, 39], nanowires [40] and alloying with active/inactive elements such as silicon-tin [41] and silicon-metal [42-46] composites. In addition, first principles calculations have recently been applied to investigate fundamental aspects of the structural changes and lithiation behavior of Si-based materials, yet many of which still remain unclear.

Recent studies [47-52] have provided evidence for the formation of various stable lithium silicide crystalline phases such as $Li_{12}Si_7$, Li_7Si_3, $Li_{13}Si_4$, $Li_{15}Si_4$ and $Li_{22}Si_5$ during high-temperature lithiation. However, room-temperature Si lithiation frequently leads to amorphous lithium silicides (*a*-Li-Si) [6]. It is therefore necessary to better understand the nature of amorphous Li-Si alloys, with comparisons to their crystalline counterparts. Very recently some theoretical efforts have been undertaken to understand the structure and properties of amorphous lithium silicides. Chevrier *et al*. [53, 54] used a protocol in conjunction with density functional theory (DFT) to analyze the energetic

and structural properties of disordered lithiated Si. Nonetheless, our understanding regarding the nature and properties of Li-Si alloys is still limited.

In this chapter, we examine the energetics, structure, electronic and mechanical properties of Li-Si alloys using DFT calculations. We first evaluate the relative stability of the alloys in both crystalline and amorphous phases by calculating the mixing enthalpies. Next, the structural evolution in terms of Li content and temperature are analyzed. The Bader charge analysis is applied to estimate the charge states of Li and Si for various Li/Si composition ratios. While the Si network and electronic structure undergo considerable changes when alloyed with Li, bulk moduli of Li-Si alloys are calculated to assess the effect of increasing Li content on mechanical properties. In addition, *ab initio* molecular dynamics (AIMD) simulations are performed to look at the dynamic behavior of a few selected Li-Si alloys at finite temperatures.

9.2 COMPUTATIONAL METHODS

The model structures of amorphous Li-Si alloys were created using AIMD simulations based on the atomic configurations of Au-Si alloys that were previously obtained using combined modified embedded atom method (MEAM) and AIMD simulations (see Ref. [84] for detailed computational methods). According to the previous study [84], Au and Si atoms in the bulk Au-Si amorphous alloy are overall well mixed with no segregation. The Au-Si interaction differs from the Li-Si interaction in nature, and thus the local atomic configurations (or short-range order) of the alloys tend to be dissimilar. Nonetheless, the Au-Si structure is likely a good starting configuration for the Li-Si amorphous structure (where Li and Si atoms are overall well distributed as well); in particular, the high mobilities of Li and Si at high temperatures (> 1000 K) allow facile local structure rearrangements. With Au-Si alloy configurations, after all Au atoms were replaced with Li atoms, the alloys were annealed at 1,500 K to accelerate melting for 2 picoseconds (*ps*) with a time step of 1 femtosecond (*fs*), and then rapidly quenched to 300 K at a rate of 0.6 K/*fs*, along with volume optimization. Here, the temperature was controlled via velocity rescaling. Each model structure contains a total

of 64 Li and Si atoms. To change the Li/Si composition ratio, Li sites are chosen at the fully scattered position in the Si matrix because the intermixing of Li and Si is preferable. This approach can provide reasonable Li-Si amorphous structures at significantly reduced computational burden compared to starting with crystalline initial configurations. The crystalline Li-Si structures considered are summarized in Table 9.1.

The calculations reported herein were performed on the basis of density functional theory (DFT) within the generalized gradient approximation (GGA-PW91 [65]), as implemented in the Vienna *Ab initio* Simulation Package (VASP) [21, 66]. Spin polarization of the Li-Si system was also examined, but appears to be insignificant. The projector augmented wave (PAW) method with a planewave basis set was employed to describe the interaction between ion cores and valence electrons. The PAW method is, in principle, an all-electron frozen-core approach that considers exact valence wave functions. Valence configurations employed are: $1s^2 2s^1$ for Li and $3s^2 3p^2$ for Si. An energy cutoff of 350 eV was applied for the planewave expansion of the electronic eigenfunctions. During geometry optimization, all atoms were fully relaxed using the conjugate gradient method until residual forces on constituent atoms become smaller than 5×10^{-2} eV/ Å. A (2×2×2) k-point mesh in the scheme of Monkhorst-Pack was used for the Brillouin zone sampling [111] for all amorphous structures and (3×3×3) ~ (11×11×11) were used for crystalline structures as shown in Table 9.1.

Table 9.1. Equilibrium lattice parameters for crystalline Li-Si alloys obtained from PAW-GGA calculations.

Phases	Space group	Lattice constants (Å)	Volume(Å^3)	# Li/Si	k-point mesh[a]	Ref.
Li	Im-3m(229)	a=3.438 (3.436)	325.2	16/0	δ	b
Si	Cm(8)	a=5.457 (5.430)	4387.6	0/216	α	c
LiSi	I41/a(88)	a=9.353 (9.353), c=5.753 (5.743)	31.5	8/8	χ	d
$Li_{12}Si_7$	Pnma(62)	a=8.546 (8.600), b=19.665 (19.755), c=14.327(14.336)	43.0	96/56	β	e
Li_7Si_3	C2/m(12)	a=4.3973,c=17.928, γ=120	50.0	40/16	χ	f
$Li_{13}Si_4$	Pbam(55)	a=7.9195, b=15.1057, c=4.4423	66.4	26/8	χ	g
$Li_{15}Si_4$	I-43d(220)	a=10.623 (10.685)	74.9	60/16	χ	h
$Li_{22}Si_5$	F23(196)	a=18.651	81.1	88/20	β	i

[a] α = (2×2×2), β = (3×3×3), χ = (5×5×5), δ = (11×11×11)
b,c:Ref. [138], d: Ref. [49, 51], e: Ref.[139], f: Ref. [140], g:Ref. [141], h:Ref. [50], i: Ref. [142].
Experimental values are supplied in parentheses whenever available.

9.3 RESULTS AND DISCUSSION

9.3.1 Structures and Stabilities

Fig. 9.1 shows a variation in the mixing enthalpy for amorphous and crystalline Li-Si alloys as a function of Li:Si composition ratio, with respect to crystalline Si (*c*-Si) and body-centered cubic Li (*bcc*-Li). The mixing enthalpy per atom (ΔE_{mix}) is given by:

$$\Delta E_{mix} = E_{Li_xSi_{1-x}} - xE_{Li} - (1-x)E_{Si}$$

where $E_{Li_xSi_{1-x}}$ is the total energy per atom of the Li-Si alloy examined; x is the atomic fraction of Li; E_{Si} and E_{Li} are the total energies per atom of *c*-Si and *bcc*-Li, respectively.

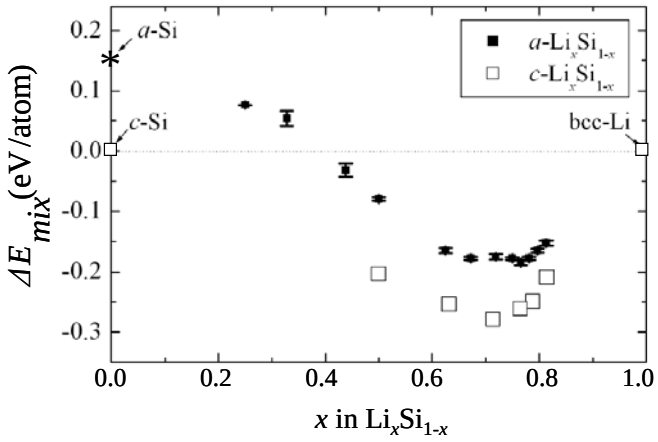

Figure 9.1. Variation in the mixing enthalpy for amorphous and crystalline Li-Si alloys as a function of Li content (at. %). The values for amorphous alloys are averaged based on 5 different 64-atom supercells.

For amorphous phases at low Li content, the mixing enthalpy is positive in value and peaks around 25 at.% Li. As the Li content increases, this value drops and changes from positive to negative at 40 at.% Li. Above this Li content, the mixing enthalpy continues to decrease and falls to a valley plateau between 60 to 80 at.% Li. The positive value of mixing enthalpy at Li contents < 40 at.% may indicate the presence of an initial barrier for Li incorporation into the Si matrix. Contrarily, the negative mixing enthalpy

at Li contents > 40 at.% suggests favorable alloy formation. According to the trend, amorphous Li-Si alloys with 60 ~ 80 at.% Li are most stable with an energy gain of 0.16−0.18 eV/atom with respect to *c*-Si and *bcc*-Li. Our calculations are consistent with previous experiments that evidenced the formation of *a*-$Li_{2.1}Si$ (≈ 68 at.% Li) with an energy gain of 0.12 eV [6]. For crystalline phases, a distinct mixing enthalpy minimum is found at 71 at.% Li, and on average the total energies are ~ 0.1 eV/atom lower than their amorphous counterparts; hence *a*-Li-Si alloys may undergo recrystallization at elevated temperatures, as evidenced by earlier experiments [30].

We looked at the structural evolution of the amorphous Li_ySi alloy with varying Li contents from y = 0 to 4.4. Figure 9.2 shows a set of the amorphous structures from our simulations, together with corresponding crystalline structures for comparison.

The amorphous structures were characterized using pair distribution function (PDF, $g(r)$), which is defined as [83]

$$g(r) = \frac{V}{N}\frac{n(r)}{4\pi r^2 \Delta r}$$

where n(r) represents particles in a shell within the region $r \pm \Delta r/2$, where Δr is the shell thickness; N denotes the number of particles in the model volume V.

Fig. 9.3 shows the pair-distribution functions for selected amorphous Li_ySi alloys; for each composition five independent 64-atom samples were used to obtain good statistics. No sharp second-neighbor peak is present, which confirms the amorphous nature (lack of long-range order) of the Li_ySi alloys. The total $g(r)$ of the $Li_{0.78}Si$ structure exhibits two distinct peaks at 2.4 and 2.7 Å, which are different from that of the remaining Li_ySi structures. The first peak originates from Si-Si pairs, whereas the second peak is attributed to a combination of Si-Li and Li-Li pairs. As the Li content increases, the second peak becomes stronger while the first peak dwindles. Furthermore, with increasing Li content, the Si-Si peak position shifts to larger pair distance while the opposite trend is found for the Li-Li peak. This is indicative of the weakened Si-Si bonds; note that the charge transferred from Li fills up the anti-bonding sp^3 states of Si and thereby weakens the Si-Si bonds as discussed in Ref. [143].

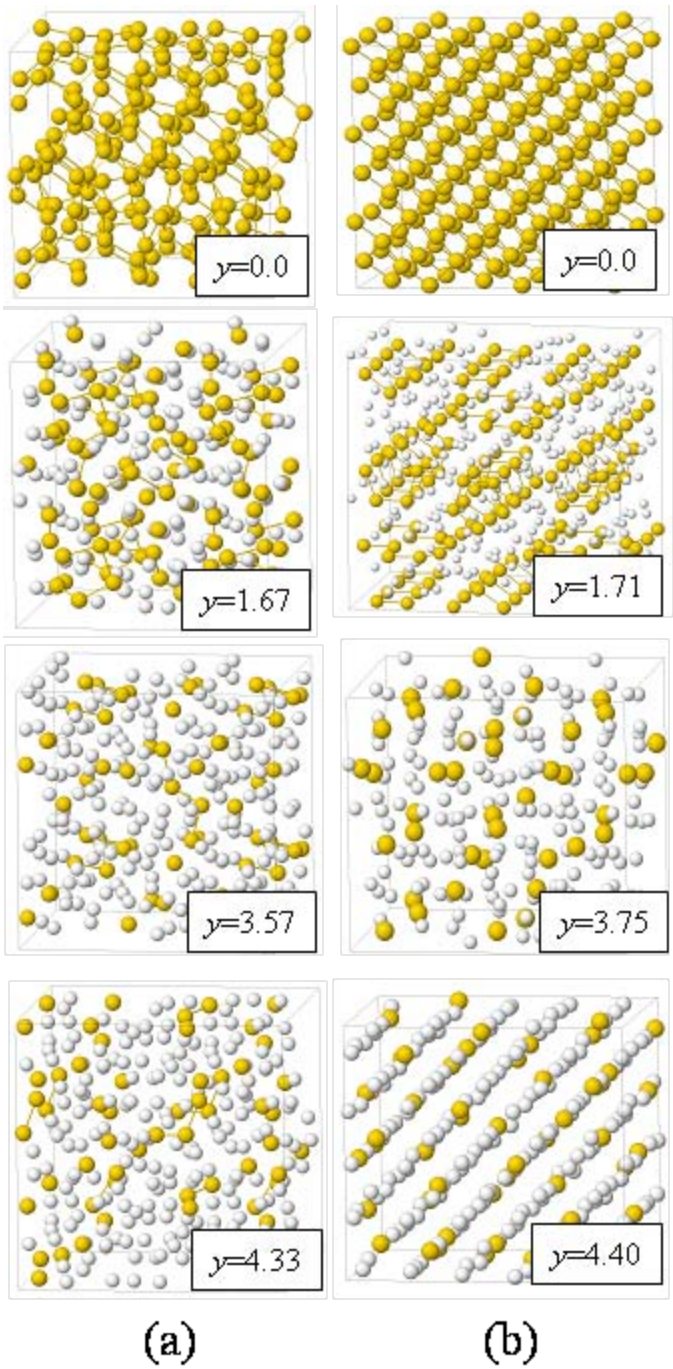

Figure 9.2. Schematic structures of amorphous and crystalline Si-Li alloys from low to high Li content y in Li_ySi. The darker (yellow) and light grey (white) balls represent Si and Li atoms, respectively.

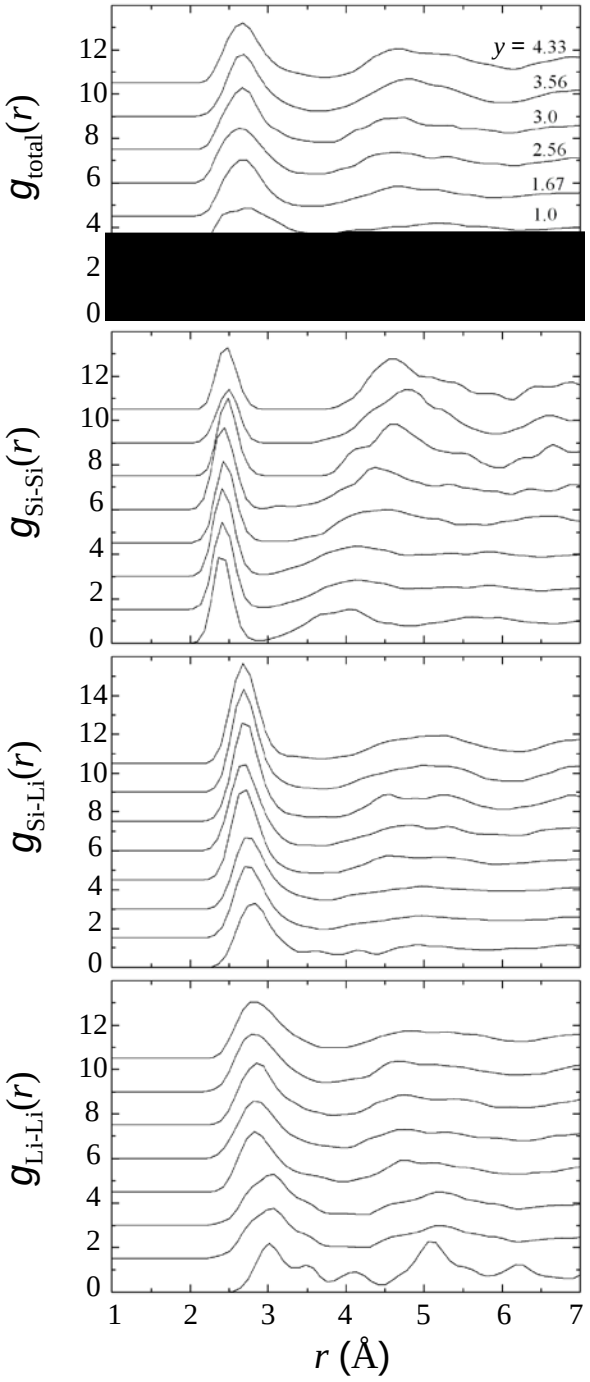

Figure 9.3. Total and partial pair-distribution functions for selected *a*-Li_ySi; for each composition, five independent 64-atom samples are used to obtain good statistics.

Table 9.2 lists the calculated average and standard deviation values for the coordination number (CN) of Si in the selected alloys as a function of cut-off radius (r). At $r \leq 2.6$ Å, the average CN decreases from 3.34 to 2.33 with increasing y from 0.5 to 4.33, and an opposite trend is observed for $r \leq 3.1$ Å, where CN increases from 6.54 to 9.97. Considering the Si-Si bond length of ≈ 2.5 Å in *a*-Si and the Li-Si bond length of 2.57 − 3.09 Å in *c*-Li_ySi alloys, the CN at $r < 2.6$ Å represents the number of Si neighbors and CN at $r \leq 3.1$ Å represents the number of Si and Li neighbors combined. The *a*-Si structure is composed of sparse Si network, but as Li content increases, the Li-Si alloy becomes more densely packed as evident by the increasing CN. We also find that at r = 3.1 Å, the CN of Si is 10.04 in *a*-$Li_{3.57}Si$ and 9.97 in *a*-$Li_{4.33}Si$, indicating the former is more highly packed (albeit to a small degree). Note that the more densely packed *a*-$Li_{3.57}Si$ also has a slightly lower mixing enthalpy than *a*-$Li_{4.33}Si$, and the same relationship is found for their crystalline counterparts, suggesting energetically *a*-$Li_{3.57}Si$ might be more favorable than *a*-$Li_{4.33}Si$.

Table 9.2. Average and standard deviation of the calculated average coordination number of Si in selected amorphous Li_ySi alloys as a function of cut-off radius (r).

y	r = 2.5	r = 2.6	r = 2.7	r = 2.8	r = 2.9	r = 3.1
0.33	2.92 (0.01)	3.36 (0.02)	3.77 (0.02)	4.45 (0.02)	4.88 (0.02)	5.68 (0.01)
0.78	2.61 (0.21)	3.26 (0.15)	4.42 (0.05)	5.47 (0.13)	6.32 (0.09)	7.50 (0.22)
1.00	2.28 (0.17)	3.44 (0.05)	5.01 (0.02)	6.31 (0.18)	7.39 (0.16)	8.41 (0.09)
1.67	2.20 (0.07)	3.28 (0.14)	4.95 (0.04)	6.64 (0.12)	7.59 (0.30)	9.12 (0.29)
2.56	1.69 (0.29)	3.18 (0.38)	5.27 (0.21)	6.62 (0.44)	7.80 (0.55)	9.15 (0.69)
3.00	1.65 (0.22)	2.78 (0.05)	5.16 (0.01)	6.91 (0.06)	8.04 (0.28)	9.69 (0.22)
3.57	1.19 (0.06)	2.84 (0.26)	5.40 (0.27)	7.31 (0.38)	8.66 (0.35)	10.04 (0.37)
4.33	1.23 (0.33)	2.33 (0.30)	5.28 (0.07)	7.17 (0.44)	8.58 (0.22)	9.97 (0.29)

Based on the model structures, the variations in volume and density as a function of Li content were calculated as shown in Fig. 9.4; the volume of each alloy is

normalized with respect to that of *c*-Si (in which each Si occupies a volume of ≈ 20.47 Å^3). For both crystalline and amorphous phases, the volume increases nearly linearly with Li content, and the opposite trend is true for the density values. As expected, the crystalline phase is slightly denser than the amorphous alloy of corresponding composition. The fully lithiated *a*-$Li_{4.33}Si$ (*c*-$Li_{4.4}Si$) phase is predicted to yield a 334 (296) % volume expansion, which is in good agreement with ≈ 300% from previous experimental measurements [44].

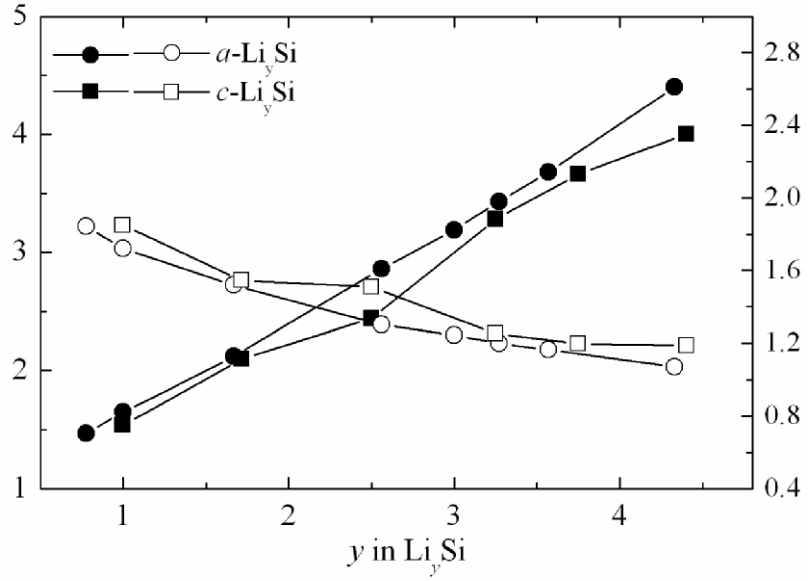

Figure 9.4. Variation in volume (solid circle and square) and density (open circle and square) of amorphous and crystalline Li-Si alloys as a function of Li content. The volume (per Li_ySi) of each alloy is normalized with respect to that of *c*-Si.

It was also found that the tetrahedrally-bonded network of Si is disintegrated into smaller Si fragments with increasing Li content. In crystalline phases, the diamond cubic structure of *c*-Si breaks up into small clusters in various shapes [49, 51, 52]. For instance, *c*-LiSi has a threefold-coordinated Si network that consists of interconnected chains and puckered eight-membered rings; *c*-$Li_{12}Si_7$ has two types of clusters, Si_5 rings and Si_4 stars; *c*-Li_7Si_3 has Si_2 dumbbells; *c*-$Li_{13}Si_4$ has a mixture of Si_2 dumbbells and Si atoms; and *c*-$Li_{15}Si_4$ and *c*-$Li_{22}Si_5$ have only single Si atoms. Likewise, in amorphous phases, the disintegration of *a*-Si into low-connectivity Si clusters also occurs as the Li content

increases. Fig. 9.5 (lower panel) shows the Si-Si coordination number versus Li content (y) for various a-Li_ySi and c-Li_ySi alloys, together with representative Si clusters found in the amorphous phases (upper panels). a-LiSi has Si_3 and Si_4 coordinated network; a-$Li_{1.67}Si$ has mixed $Si_4 \sim Si_6$ strings and rings (as also reported in Ref. [144]); a-$Li_{2.56}Si$ has Si_3 clusters, Si_2 dumbbells and Si atoms; a-$Li_{3.57}Si$ has Si_3 and Si_4 strings; a-$Li_{4.33}Si$ has Si_2 dumbbells and Si atoms. As summarized in Fig. 9.5, in amorphous phases, roughly 30 ~ 40% of Si atoms still form Si-Si pairs even in highly lithiated states (a-$Li_{3.57}Si$ and a-$Li_{4.33}Si$); however, in crystalline phases (c-$Li_{15}Si_4$ and c-$Li_{22}Si_5$), all Si atoms are isolated.

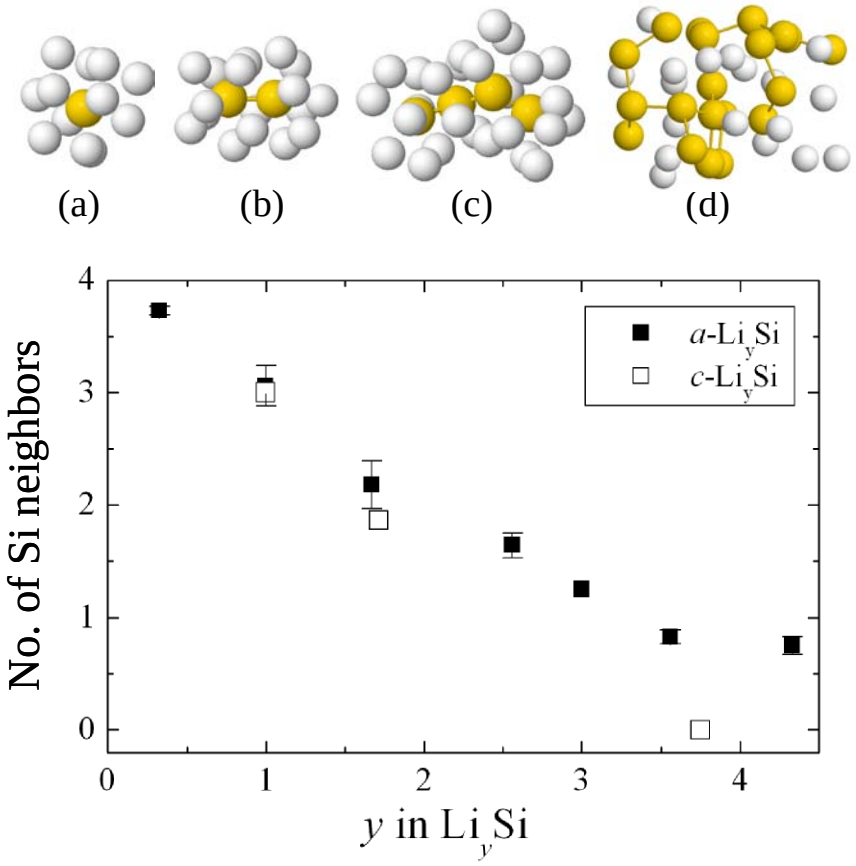

Figure 9.5. (Lower panel) Si-Si coordination number (CN) versus Li content (y) for various a-Li_ySi and c-Li_ySi alloys; (Upper panels) representative Si clusters found in the amorphous phases. The darker (yellow) and light grey (white) balls represent Si and Li atoms, respectively.

9.3.2 Dynamic behaviors at finite temperatures

We performed *ab initio* molecular dynamics (AIMD) simulations in the canonical (NVT) ensemble to examine the dynamic behavior of Li and Si in $Li_{1.67}Si$ and $Li_{3.57}Si$ alloys. Three simulation temperatures were chosen; 300 K and 500 K in amorphous state and 1,050 K in liquid state. For the amorphous cases, the alloy density was kept constant regardless of the temperature variation (see Fig. 9.4 for the density values). In the liquid state, the experimental densities for Li-Si alloys of similar compositions and temperature were used (minor scaling was done as needed). For each alloy, the internal pressure as a function of cell volume was verified to ensure that the chosen density is reasonable. For the short-range order analysis, all three alloys examined were equilibrated at 300 K and 500 K for 2 *ps*, and 1,050 K for 6 *ps*; 5 different configurations were used for each alloy to produce averaged PDFs as shown in Fig. 9.6. When the temperature increases, atoms spread around their average positions as the PDF peaks broaden and shrink in intensity. At 1,050 K, the first peak is more broadened, but there is no significant deviation from the PDF profiles at 500 K; this may suggest the short range order of Li-Si alloys is maintained even in the liquid state.

To better understand the dynamic properties, AIMD simulations were also performed to estimate Li and Si mobilities in molten LiSi, $Li_{1.67}Si$, and $Li_{3.57}Si$ alloys at 1,050 K. The MD duration of 6 *ps* appears to be sufficient to obtain well converged results, and for each alloy, 5 samples were averaged to calculate the mean-square displacements (MSD). Fig. 9.7 shows the variations in MSD (insets) and diffusion constant of Si and Li as simulation time progresses. The MSDs are linearly proportional to time as can be expected from a liquid phase. The diffusion constants of Si and Li were calculated based on the Einstein relation:

$$D = \frac{< |R_i(t) - R_i(0)|^2 >}{6t}$$

where R_i is the atomic position, broken brackets denote thermal averages and t is the time.

For LiSi, the diffusion coefficients were predicted to be D_{Li}= 0.45 ± 0.04 10^{-4} and D_{Si} = 0.20 ± 0.05× 10^{-4} cm^2/sec. For $Li_{1.67}Si$, D_{Li}= 0.50 ± 0.07 × 10^{-4} and D_{Si} = 0.23 ±

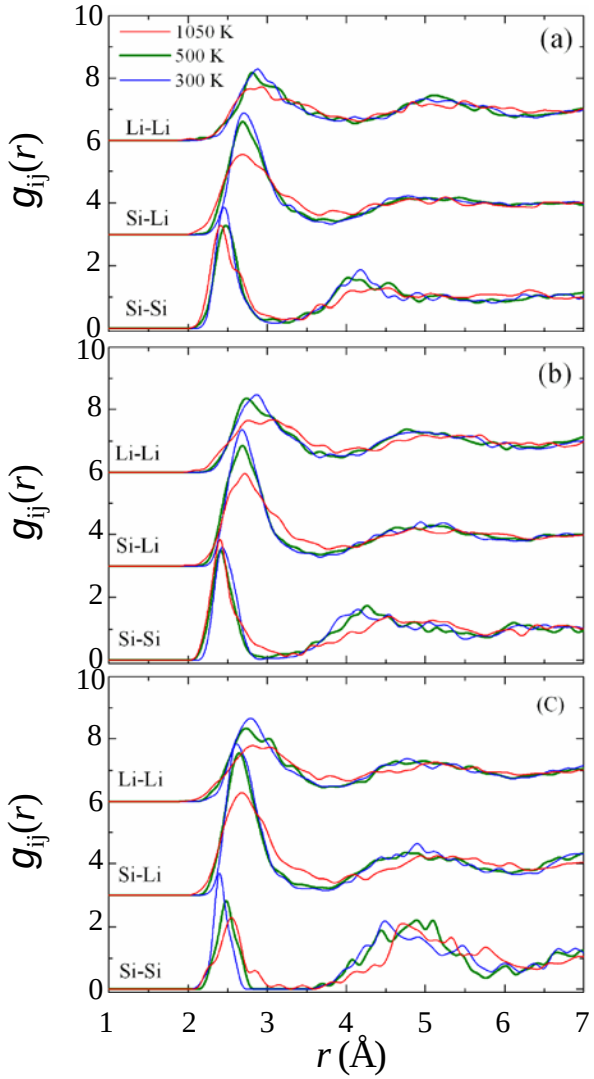

Figure 9.6. Pair distribution functions for (a) LiSi , (b)$Li_{1.67}Si$, and (c) $Li_{3.57}Si$ at 300 K (blue), 500 K (green) and 1,050 K (red).

0.07 × 10^{-4} cm^2/sec, which are comparable to the values reported in previous DFT calculations, D_{Li}= 0.94 × 10^{-4} and D_{Si} = 0.42 x 10^{-4} cm^2/sec [144]. For $Li_{3.57}Si$, the diffusivities increase to D_{Li}= 0.73 ± 0.06 × 10^{-4} and D_{Si} = 0.33 ± 0.05 × 10^{-4} cm^2/sec. Note that despite the change in alloy composition, the diffusion coefficient ratio between Li and Si remains more the less constant, $D_{Li}/D_{Si} \approx 2$. This is not surprising considering

the mass dependence of diffusivity in a liquid-like phase, i.e., $D_2/D_1 \sim (m_1/m_2)^{1/2}$ for a disparate-mass binary mixture. Given the atomic mass for Li and Si are 6.94 amu and 28.09 amu, respectively, our calculation result is consistent with what would be expected from the mass-dependency, i.e., $D_{Li}/D_{Si} \approx (28.09/6.94)^{1/2} = 2.0$. Our calculations also show that Li mobility tends to be hindered by the heavier and slower Si atoms. At the highly lithiated case ($Li_{3.57}Si$) the diffusivity of Li is enhanced relative to that in LiSi or $Li_{1.67}Si$, while the diffusivity of Si also increases as facilitated by the fast diffusing Li.

For reference, the experimental self-diffusion coefficients for Li at 470 K and Si at 1,687 K were reported to be $D_{Li} \approx 0.65\times10^{-4}$ cm^2/sec [145] and $D_{Si} \approx 4.00\times10^{-4}$ cm^2/sec [146]. Since there is no experimental data available, we approximated D_{Li} and D_{Si} at our simulation temperature of 1,050 K using analytical models [147-152] that have been proposed to describe the temperature-dependence of liquid diffusivity. Here, Si is assumed to be liquid at 1,050 K for comparison purpose; although *a*-Si might start to melt above 1480 ± 50 K [153]. From these models, the Li and Si self-diffusion coefficients at 1,050 K were roughly estimated to be 0.65 ~ 3.24×10^{-4} and 1.55 ~ 4.00×10^{-4} cm^2/sec, respectively [154], greater than the predicted values in the Li-Si alloys. The lower diffusivities might be attributed to the interaction between Li and Si; this is not surprising considering that the alloys are more stable than their pure counterparts as evidenced by the negative mixing enthalpy values presented earlier.

9.3.3 **Electronic and mechanical properties**

We calculated the charge states of Si and Li in *c*-Li_ySi and *a*-Li_ySi using the grid-based Bader analysis [72], special care was taken to ensure convergence with respect to the grid size. As summarized in Table 9.3, the Si charge state significantly varies from −0.84 to −3.31 with increasing Li content from y= 1 to 4.4 in *c*-Li_ySi, while the Li charge state remains nearly unchanged (+0.8 ~ +0.82). For highly lithiated amorphous phases (*a*-$Li_{3.57}Si$ and *a*-$Li_{4.33}Si$) where Si_2 dimers and single Si atoms are prevailing, the charge states of Si and Li are estimated to be −2.38 (± 0.41) for Si_2 dimers, −3.61 (± 0.23) for Si monomers, and +0.8 (± 0.02) for Li. The charge states of Si can be explained by general

Zintl rules [155] with the consideration that only partial charge is transferred from Li to Si. For instance, the calculated charge states of Si dimers (in *c*-Li_7Si_3) and monomers (in *c*-$Li_{22}Si_5$) are −2.05 and −3.31, while if were in perfect Zintl phases (transfer completes the octet shell of Si), these values should be close to −3.0 and −4.0, respectively.

Table 9.3. The charge states of Si and Li in *c*-Li-Si alloys calculated using the grid-based Bader charge analysis.

	LiSi	$Li_{12}Si_7$	Li_7Si_3	$Li_{15}Si_4$	$Li_{22}Si_5$
Si	- 0.84	- 1.3$^{(R)}$ - 0.46$^{(SC)}$ - 1.88$^{(ST)}$	- 2.05$^{(D)}$	- 3.31$^{(M)}$	- 3.31$^{(M)}$
Li	+ 0.84	+ 0.84	+ 0.80 ~ 0.82	+ 0.80	+ 0.80 or 0 (Li^0)

(R): ring, (SC): string center, (ST): string terminal, (D): dumbbell, (M): monomer

Fig. 9.8 shows the electron density of states (DOS) projected on Si atoms in selected amorphous and crystalline Li-Si alloys, along with the DOS of pure Si for comparison; the analysis could demonstrate how the Si-Si bonding property changes as a function of Li content. The Fermi level is used as a reference energy, which is set to be zero. As expected, pure Si exhibits strong *s*-*p* hybridization leading to the tetrahedral sp^3 structure, while the amorphous phase yields a larger band gap than the crystalline phase. As Li content increases, the degree of *s*-*p* hybridization decreases; note that the splitting between 3*s* and 3*p* states grows larger going from LiSi to their higher lithiated states. As the Li content increases, the Li-Si alloy bandgap gradually diminishes, showing more metallic character. In addition, the distributions of the 3s and 3p states get narrower with increasing Li content, which is apparently attributed to the decreasing Si-Si bonding interaction, as the Si network loses its connectivity and disintegrates into smaller fragments, as discussed earlier. We can also notice that the DOS profiles for the crystalline and amorphous phases have slightly different patterns at any given

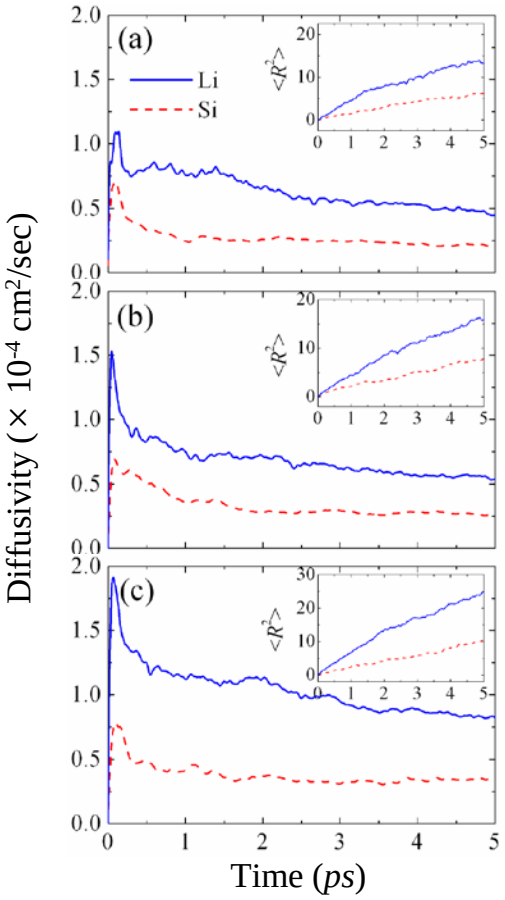

Figure 9.7. The variation in mean square displacement (shown in insets) and diffusion constant of Si and Li in liquid (a) LiSi, (b) $Li_{1.67}Si$, and (c) $Li_{3.57}Si$ alloys at 1,050 K as simulation time progresses. The blue and dotted-red lines represent Li and Si profiles, respectively.

composition, which is mainly due to variations in the Si cluster shape (such as pairs, strings, rings, etc). For instance, *a*-$Li_{1.67}Si$ has broader peaks than its crystalline counterpart (*c*-$Li_{12}Si_7$) because Si_3 ~ Si_4 strings and rings in the former phase allow stronger Si-Si interaction than the Si_4 stars and Si_5 rings in the later phase. Likewise, *a*-$Li_{3.57}Si$ that also consists of a fair amount of Si_2 dimers has broader peaks than *c*-$Li_{15}Si_4$ containing only Si monomers.

Our calculations clearly demonstrate the gradual structural transformation as well as the softening of Si-Si bond strength as the Li content increases. Finally, we looked at how the changes in the atomic and electronic structures affect the mechanical properties

of Li-Si alloys. Here, we only calculated the bulk modulus (B) for each alloy, which can be determined by fitting the Murnaghan equation of state [73] to the corresponding energy versus volume curve. In our calculations, uniform tensile and compressive stresses were imposed on the alloys to achieve ±10 % volume variation.

$$E(V) = E_0 + \left(\frac{BV}{B'}\right)\left[\frac{(V_0/V)^{B'}}{(B'-1)} + 1\right] - \frac{V_0 B}{(B'-1)}$$

where E and E_o refer to the total energies of a given LiSi supercell at volume V and V_o (equilibrium), respectively, B is the bulk modulus, and B' is the pressure derivative of the bulk modulus.

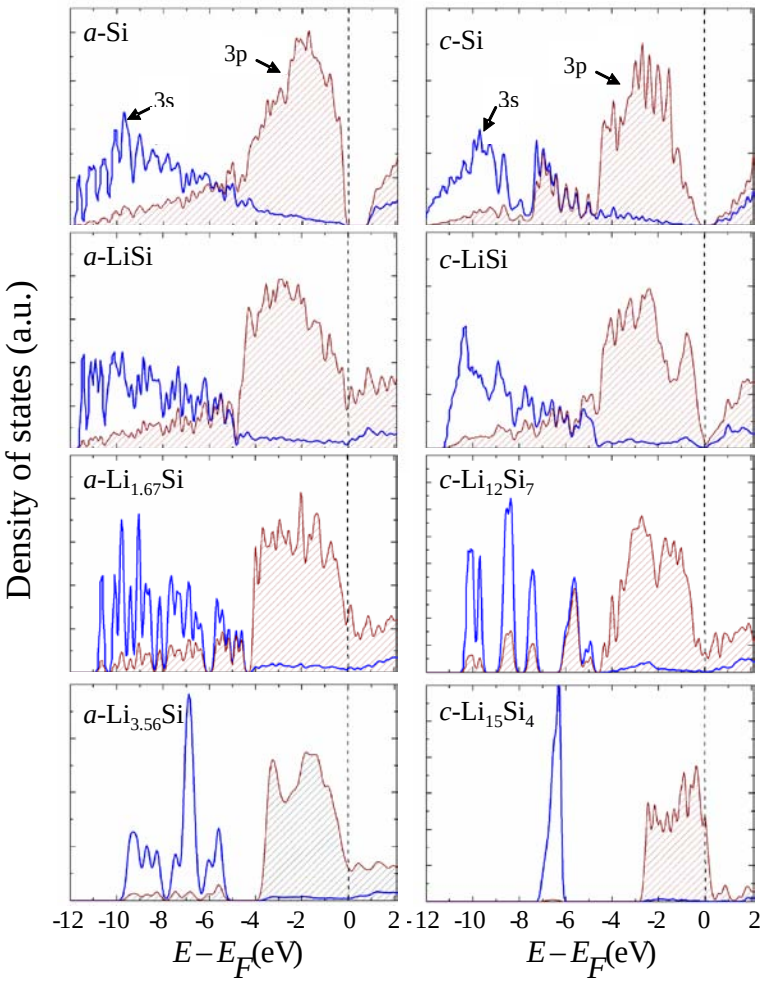

Figure 9.8. The electron density of states (DOS) projected on Si atoms in various Li-Si alloys in both amorphous and crystalline phases, along with the DOS of pure Si for comparison. The Fermi level is used as the reference energy state, which is set to zero.

Fig. 9.9 shows the variation in bulk moduli for *c*-Li-Si and *a*-Li-Si alloys. The calculated bulk moduli for *c*-Si and *bcc*-Li are $B_{c\text{-}Si}$ = 87.8 GPa and $B_{bcc\text{-}Li}$ = 12.7 GPa, in good agreement with the experimental values of $B_{c\text{-}Si}$ = 100.0 GPa [156] and $B_{bcc\text{-}Li}$ = 11.6 GPa [157]. The dotted line connecting the bulk moduli of *c*-Si and *bcc*-Li represents a linear relation between the bulk modulus and the Li concentration (*x*). For both amorphous and crystalline Li-Si alloys, the bulk moduli indeed decrease with increasing Li content in a nearly linear manner leading to significant elastic softening. For a given Li content, the amorphous phase tends to be softer than its crystalline counterpart.

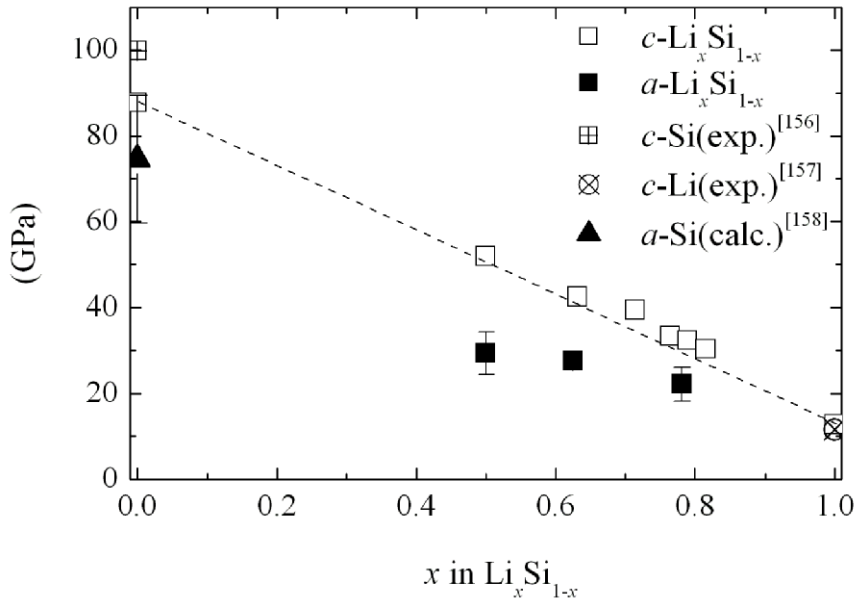

Figure 9.9. Variation in bulk moduli for *c*-Li-Si and *a*-Li-Si alloys as a function of Li content; the dotted line connecting the bulk moduli of *c*-Si and *bcc*-Li represents a linear relation between bulk modulus and *x*. The calculated bulk modulus for *a*-Si is $B_{a\text{-}Si}$= 74.5 ± 14.9 [158] and experimental value for *a*-Li is $B_{a\text{-}Li}$≈12.0 GPa [157].

9.4 SUMMARY

Using DFT-GGA and AIMD calculations, we examined the energetics, structure, electronic and mechanical properties of crystalline and amorphous Li-Si alloys. According to our mixing enthalpy calculations, the favorable alloy formation occurs around 71 at. % Li for the crystalline phase and 60 - 80 at. % Li for the amorphous phase, and *c*-Li-Si alloys are approximately 0.1 eV more favorable than their amorphous

counterparts. With increasing Li content, we find that: i) the tetrahedrally bonded Si network undergoes disintegration into low-connectivity clusters of various shapes; ii) the *a*-Li-Si becomes more densely packed as evidenced by the increasing CN; iii) Si-Si PDF peaks shift toward larger *r* values as a result of weakened Si-Si bonds. Bader charge analysis shows that while the charge state of Li remains nearly unchanged around +0.80 to +0.82, that of Si varies significantly from −0.46 to −3.31 depending on the number of Si neighbors as can be understood by Zintl rules. Our electronic DOS analysis illustrates that towards higher lithiated states, the Si s-p splitting grows larger accompanied by weakening/breaking of Si-Si bonds and changes in the alloy structure. Due to the softening of the Si network, the bulk modulus decreases almost linearly with increasing Li content. The electronic analysis also reveals the band gap narrowing with increasing degree of lithiation, showing more metallic character. According to AIMD calculations at finite temperatures, the short range order of Li-Si alloys tends to be maintained even in the liquid state; due to the Li-Si interaction, a drop in Li and Si diffusivities is seen when alloyed with each other. The fundamental findings assist in understanding the nature of Li-Si alloys, and the present work also provides a framework for the study of various lithiated alloys.

Chapter 10:
The Structure and Properties of Li-Si, Li-Ge, and Li-Sn Alloys

10.1 Introduction

Semiconductor or semiconductor alloy materials have recently emerged as a promising candidate for anodes in lithium-ion batteries because they exhibit a higher energy-storage capacity than the conventional graphite anode. However, the practical use of a pure semiconductor (Si, Ge, Sn) as an anode material is hampered by their low intrinsic electrical conductivity and poor cycling performance [32-35]. In particular, the volume increasing up to 200 % (for Sn), 250% (for Ge), and 300 % (for Si) during lithiation can cause severe cracking and pulverization of the electrode and consequent capacity fading arising from the loss of electrical contacts.

Considerable efforts have been made to overcome these problems, for instance, through structural modifications such as amorphous phases [36, 37, 159], nanoparticles [38, 39], nanowires [40] and alloying with active/inactive elements such as silicon-tin [41] and silicon-metal [42-46] composites. Here the two issues can be combined into both amorphous phase and alloy. The amorphous semiconductor alloy (silicon and tin) provides several advantages over the binary Si-Li, Ge-Li, and Sn-Li system such as homogeneous lower volume expansion than the pure Si and flexibility for Li to diffuse in/out. Recently, Dahn et al. sputtered the amorphous Si-Sn film and then showed that the electrochemical reaction with Li is reversible for long cycles [41, 44, 159, 160]. Before foregoing our work focusing on the effective alloy, it is necessary to investigate fundamental aspects of the structural changes and lithiation behavior of amorphous Si-Li, Ge-Li, and Sn-Li system.

While the tetrahedral network in the covalent bond system can be easily disintegrated by lithiation, it has also been reported that the lithiated Si at room temperature tends to exhibit no crystalline phases [6], possibly because of a kinetic barrier to crystallization. The kinetic effect can be more important at the onset of lithiation because the introduction of Li into a rather rigid tetrahedral network would be

thermodynamically more unfavorable and thus the lithiated structures of Si (Ge, Sn) would be more kinetically controlled, compared to a highly flexible Li-rich alloy. However, thus far there has been no comprehensive study as to the dynamic behavior of Li in Ge (Sn)-based materials and also the influence of Li introduction on the stability of the host lattice, particularly in the early stages of lithiation.

Very recently some theoretical efforts have been undertaken to understand the structure and properties of amorphous lithium silicides. Chevrier *et al*. [53, 54] used a protocol in conjunction with density functional theory (DFT) to analyze the energetic and structural properties of disordered lithiated Si. Nonetheless, our understanding regarding the nature and properties of Li-Ge and Li-Sn alloys are still limited.

In this chapter, we examine the structure, diffusion, and interaction of Li atoms in Si, Ge, Sn and how Li incorporation affects the nature of the tetrahedral bonding network using density functional theory calculations. In the first part, we present the atomic structure, stability and bonding mechanism of interstitial Li in crystalline host matrix. The result also shows how Li introduction leads to weakening of nearby bonds in host matrix. Next, Li diffusion and Li-Li interactions in the neural states are estimated.

In the second part, we evaluate the relative stability of the alloys in both crystalline and amorphous phases by calculating the mixing enthalpies. Next, the structural evolution in terms of Li content is analyzed. The Bader charge analysis is applied to estimate the charge states of Li and Si (Ge, Sn) for various Li/Si(Ge, Sn) composition ratios. While the tetrahedral network and electronic structure undergo considerable changes when alloyed with Li, bulk moduli of Li-Si, Li-Ge, and Li-Sn alloys are calculated to assess the effect of increasing Li content on mechanical properties.

The calculation results provide some insight into the effect of Li incorporation on destabilization of the Si (Ge, Sn) lattice, particularly in the early stages of lithiation. In addition, the alloy calculations provide some insight into the thermodynamical stability of the binary alloys, dynamic behavior of Li atoms.

10.2 Methods

The model structures of amorphous Li-Si, Li-Ge, and Li-Sn alloys were created using AIMD simulations based on the atomic configurations of Au-Si alloys that were previously obtained using combined modified embedded atom method (MEAM) and AIMD simulations (see Ref. [143] for detailed computational methods). According to the previous study [84], Au and Si atoms in the bulk Au-Si amorphous alloy are overall well mixed with no segregation. The Au-Si interaction differs from the Li-Si interaction in nature, and thus the local atomic configurations (or short-range order) of the alloys tend to be dissimilar. Nonetheless, the Au-Si structure is likely a good starting configuration for the Li-Si amorphous structure (where Li and Si atoms are overall well distributed as well); in particular, the high mobilities of Li and Si (Ge, Sn) at high temperatures (> 1000 K) allow facile local structure rearrangements. With Au-Si alloy configurations, after all Au atoms were replaced with Li atoms and Si atoms were replaced with Ge for Li-Ge or Sn for Li-Sn, the alloys were annealed at 1,500 K for 2 picoseconds (*ps*) with a time step of 1 femtosecond (*fs*), and then rapidly quenched to 300 K at a rate of 0.4 K/fs, along with volume optimization. Each model structure contains a total of 64 Li and Si (Ge or Sn) atoms. Here, the temperature was controlled via velocity rescaling. This approach can provide reasonable amorphous structures at significantly reduced computational burden compared to starting with crystalline initial configurations. The crystalline Li-Si, Li-Ge, and Li-Sn structures considered are summarized in Table 10.1.

The calculations reported herein were performed on the basis of density functional theory (DFT) within the generalized gradient approximation (GGA-PW91) [65], as implemented in the Vienna *Ab initio* Simulation Package (VASP) [21, 66] Spin polarization of the Li-Si system was also examined, but appears to be insignificant. The projector augmented wave (PAW) method with a planewave basis set was employed to describe the interaction between ion cores and valence electrons. The PAW method is, in principle, an all-electron frozen-core approach that considers exact valence wave functions. Valence configurations employed are: $1s^2 2s^1$ for Li, $3s^2 3p^2$ for Si, $3d^{10} 4s^2 4p^2$ for Ge, and $4d^{10} 5s^2 5p^2$ for Sn. An energy cutoff of 350 eV was applied for the planewave

expansion of the electronic eigenfunctions. During geometry optimization, all atoms were fully relaxed using the conjugate gradient method until residual forces on constituent atoms become smaller than 5×10^{-2} eV/ Å. A (2×2×2) k-point mesh in the scheme of Monkhorst-Pack was used for the Brillouin zone sampling[38] for all amorphous structures and (3×3×3) ~ (11×11×11) were used for crystalline structures as shown in Table 10.1.

Table 10.1. Optimized lattice parameters for crystalline Li-Ge and Li-Sn alloys considered in this work, together with crystallographic description. For each structure, the number of Li and Ge(Sn) atoms per supercell and the k-point mesh size employed are also presented.

Phases	Space group	Lattice constants (Å)	Volume (Å^3)	# Li/Ge	k-points mesh$^{\alpha}$	Ref.
Ge	Cm(8)	a=5.75 (5.66)	47.52	0/2	δ	a
LiGe	I41/a(88)	a=9.846 (9.75),b=9.846 (9.75), c=5.810 (5.78)	564.34	16/16	δ	b
Li7Ge2	Cmmm(55)	a=8.179 (9.24), b=15.135 (13.21), c=4.508(4.63)	558.12	28/8	χ	c
Li15Ge4	I-43d (220)	a=10.698 (10.72)	1224.41	60/16	χ	d
Li22Ge5	F23(196)	a=18.859 (18.75)	1676.92	88/20	β	e

Phases	Space group	Lattice constants (Å)	Volume (Å3)	#Li/Sn	k-points$^{\alpha}$	Ref.
Sn	Fd-3m (227)	a=4.70 (5.43), b=4.70 (5.43),c=4.70 (5.43)	73.29	0/2	χ	l
Li2Sn5	P4/mbm(127)	a=10.460 (10.274), b=10.460(10.274),c=3.080 (3.125)	336.99	4/10	χ	g
LiSn	P2/m (10)	a=5.197 (5.17), b=3.121(3.18),c=7.856 (7.74), β=104.5	125.40	3/3	χ	f
Li7Sn3	P2-1/m(11)	a=8.53 (8.56), b=4.71 (4.72), c=9.44(9.45), γ=105.95	364.62	14/6	χ	h
Li13Sn5	P-3m1(164)	a=4.69 (4.74), b=4.69 (4.74), c=17.04(19.83), γ=120	322.82	13/5	χ	i
Li7Sn2	Cmmm(65)	a=8.578(9.8), b=15.996(13.8), c=4.714(4.75)	646.84	28/8	β	j
Li22Sn5	F23(196)	a=19.66(19.7), b=19.66(19.7), c=19.66(19.7)	1900.79	88/20	α	k

$^{\alpha}$ α = (2×2×2), β = (3×3×3),χ = (5×5×5),δ = (11×11×11)
j: Ref. [141], a ~ i and k ~ l : Ref. [161-171].

10.3 RESULTS AND DISCUSSION

10.3.1 Structure and Stability

In order to probe the lattice disturbance induced by Li interstitials in different host materials, a comparative study on the displacements of nearest neighbors (NNs) and relative formation energy were performed with the consideration of possible effects from volume relaxation. Li was inserted in the tetrahedral interstitial position (T-site), which has been identified as the most favorable insertion site in diamond Si [143]. For the volume-relaxation calculation, the unit-cell volume and atom positions of the host lattice were allowed to relax after lithium insertion whereas for the constant-volume calculation, only the atom positions were allowed to relax. Lithium insertion imposes a strain field on the surrounding atoms, leading to a slight outward relaxation of the nearest neighbors (NNs) and variation in cell volume, as summarized in Fig. 10.1.

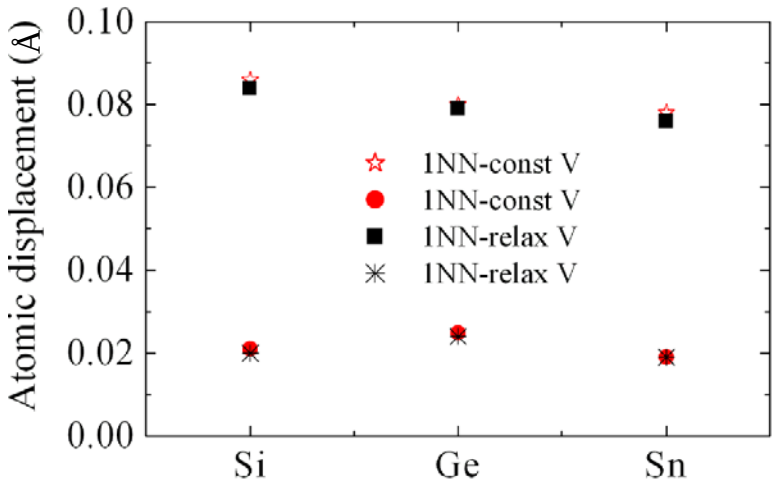

Figure 10.1. First and second nearest neighbor displacements upon one Li T-site insertion in Si, Ge and Sn 216-atom cells.

The atomic displacements for the 2nd NNs are significantly smaller than that of the 1st NNs, indicating the strain imposed by Li insertion falls off quickly beyond the nearest neighbor distance. Among host lattices considered, Si has the largest and Sn the smallest atomic displacement. This trend could be explained considering the outward

relaxation is highly dependent on both the atomic size and modulus of a host material. If the host atoms were smaller in size, greater atomic displacement could be expected simply due to the geometrical effect. Greater atomic displacements could also be expected from a host material of smaller cohesive energy, thus weaker bond strength, lower modulus and more compliant. Given the atomic radii of Si $_{(1.11\ Å)}$ < Ge $_{(1.22\ Å)}$ < Sn $_{(1.40\ Å)}$, and the cohesive energies (bulk moduli) of Sn $_{[3.14]}$ < Ge $_{[3.83]}$ < Si $_{[4.68\ eV/atom]}$ (Sn $_{[43]}$ < Ge $_{[75]}$ < Si $_{[98\ GPa]}$), it is reasonable to find Si with the highest and Sn with the lowest atomic displacement/volume variation. Note that the effect of volume relaxation does not lead to significantly different results, and the variation in cell volume due to one Li insertion is less than 0.4 %.

Next, the formation energy of T-site Li with respect to *c*-Si (Ge, Sn) and *bcc*-Li (body-centered cubic Li) is determined in order to evaluate the relative ease of Li insertion. The formation energy is defined by the equation below, and comparative results are shown in Fig. 10.2.

$$E_f = E_{total}^{A+Li} - (E_{total}^{A} + E_{total}^{Li})$$

where *A* denotes the respective host material.

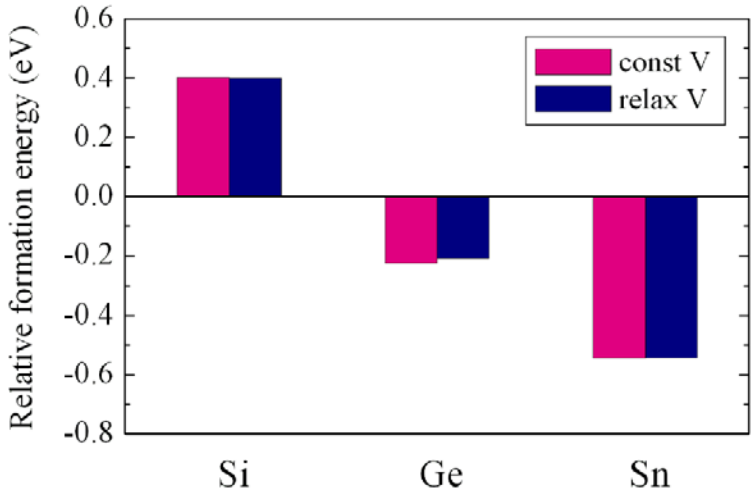

Figure 10.2. Calculated relative formation energies of one T-site Li in Si, Ge and Sn lattices. Negative formation energy indicates the lithiated solid solution is stable and energetically favorable.

As shown in Fig. 10.2, Li incorporation in Sn requires the lowest formation energy among the three host materials considered. The bigger atomic size and softer matrix of Sn permit larger interstitial space and less resilience to structural expansion, thus incorporation of Li in Sn is favorable and causes only minor disturbance to the host lattice. Contrarily, due to the size and modulus effect, more severe lattice disturbance is expected in Si and therefore the positive formation energy.

10.3.2 Bonding Mechanism

Fig. 10.3 shows the electron density of states (DOS) of the pure host materials and the projected DOS on Si, Ge and Sn as one T-site Li is inserted in 216-atom cells. The Fermi level is used as a reference energy, which is set to be zero. The analysis could provide some insight on how the bonding property changes upon Li insertion. In all three host materials, Fermi level shifts above the original conduction band minimum, indicate the transferred charge from Li to the host lattice. The amounts of electron transfer to Si, Ge and Sn matrixes are estimated to be 0.83e, 0.85e and 0.87e from the grid-based Bader charge analysis [72], special care was taken to ensure convergence with respect to the grid size. In the case of Li in Si lattice, previous study has shown that the transferred charge is highly localized within the first nearest Si atoms. In order to determine whether this transferred charge localization is also seen in the other host lattices, we calculated the nearest neighbor electron gain (per atom) in Si, Ge and Sn; results are shown in Fig. 10.4. Compared to Ge and Sn, a more rapid drop in electron gain is seen in Si; from 0.24e (1^{st} NN), 0.1e (2^{nd} NN) to 0.01e (3^{rd} NN), and there is no indication of electron gain beyond the 3^{rd} NN. For Li in Ge, the electron gain drops less rapidly from 0.13e, 0.06e to 0.05e at the 3^{rd} NN. In the case of Sn, although the electron gain decreases from 0.15e, 0.04e to 0.03e at the 3^{rd} NN, the analysis indicates still 0.02e gain at the 4^{th} NN, suggesting the transferred charge is more itinerant and farther spread in Sn. Based on these results, we see the transferred electron is highly localized in Si and more itinerant in Sn; the positively ionized Li interstitial may be effectively screened by the transferred electron in Si and less so in Sn.

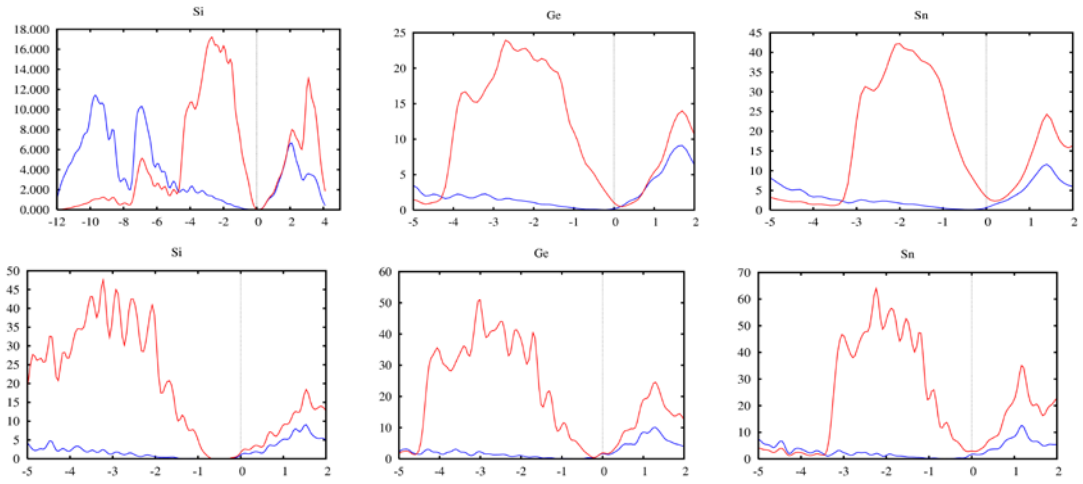

Figure 10.3. The electron density of states (DOS) projected on Si, Ge and Sn as one T-site Li is inserted in 216-atom cells, along with the DOS of pure host materials for comparison. The Fermi level is used as the reference energy state, which is set to zero.

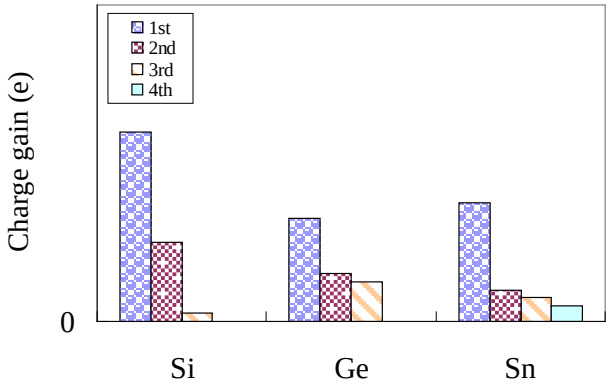

	Si	Ge	Sn
1st	0.24	0.13	0.15
2nd	0.1	0.06	0.04
3rd	0.01	0.05	0.03
4th			0.02

Figure 10.4. The electron gain (per atom) by the 1st, 2nd, 3rd and 4th nearest neighbors in Si, Ge and Sn matrices; the charge transfer is estimated using grid-based Bader charge analysis.

10.3.3. Li-Li Interaction

Next, we look at the interaction between two Li interstitials in crystalline Si, Sn and Ge. Fig. 10.5 shows the variation in the relative energies with respect to the fully separated state for various Li-Li distances; one Li is at a T-site while the other is placed

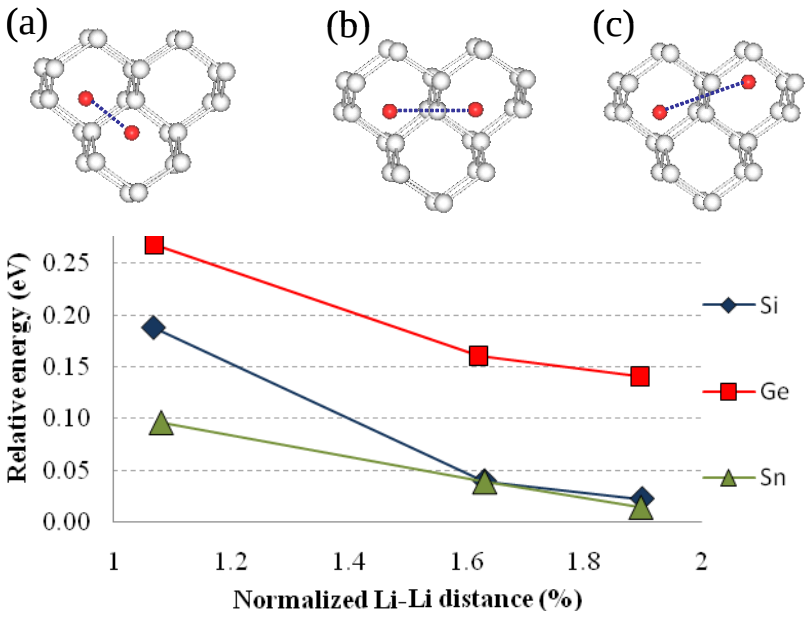

Figure 10.5. Variation in the relative energy with respect to the fully separated state for various Li-Li distances. Li and the host atoms are represented in red and white, respectively. One Li is at T-site while the other is placed at the first (a), second (b) or third (c) nearest neighboring T-site.

at the first (a), second (b) or third (c) nearest neighboring T-site. The Li-Li distances were normalized to their respective self-interstitial distances.

The relative energy drops with increasing Li-Li separation distance; the value and rate of the descending energy plot provide insight into the repulsive Coulomb interaction in different matrices. Three features in Fig. 10.5 are worth noting. First, the Li-Li distances in configuratios (a), (b), and (c) are predicted to be the large than the distances between the corresponding 1^{st}, 2^{nd} , and 3^{rd} nearest T-site self-interstitials attributed to both the repulsive interaction between Li and the outward relaxation of the host lattice upon Li insertion. Second, based on the Coulomb potential, the repulsive interaction between Li cations are expected to be stronger in Si than Ge and Sn due to its lower electrical permittivity; however, the repulsion seems to be the highest in Ge instead of Si. This is reasonable accounting for the beforementioned strong screening effect in Si; as Li cations are more effectively shielded, the repulsive interaction in reduced more greatly in Si, leading to the lower relative energy. Third, looking at the steepness of the descending

relative energy, we see the repulsive interaction drops most rapidly in Si, consistent with its ability to shield Li cations.

10.3.4 Diffusion

Comparison of the Li ion mobility in materials of potential application as secondary battery electrode is of vital interest. As previously identified, the most favorable diffusion path of Li in *c*-Si is for Li to jump between adjacent T-sites via the H-site [143]. In this work, we look into the variations in Li migration barrier as the host lattice material changes from Si to Ge, Sn; the Li diffusion pathway is illustrated in Fig. 10.6.

	Diffusion barrier (*D*) (eV)
Si	0.62
Ge	0.44
Sn	0.39

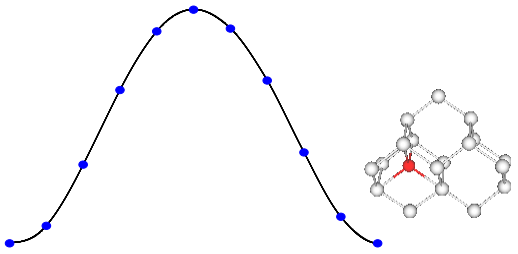

Figure 10.6. The Li (red atom) diffusion pathway in Si, Ge or Sn (white atoms). Li jumps from T-site (a) to the adjacent T-site (c) via H-site (b).

As Li tends to lose an electron to its nearest neighbors, the cation diffusion model proposed by Sharma and Kasir may be applied in aid to understand the contributing factors to affect the barriers. According to this model, cation diffusion is analogous with a hard sphere passing through a square, which has some flexibility to expand or contract. The diffusion barrier is the difference in energy when the ion is at the saddle point position, *S*, and when it is at the site *B*. This energy difference actually consists of two parts. The first part, E_1, is associated with the electrostatic (Madelung) work that can influence the transport the ion from *B* to *S*. The second part, E_2, attributes to the

mechanical work due to outward lattice relaxation for the ion to pass through. This relation is described as [129]

$$E_C^+ = E_1 + E_2 = (\alpha_S - \alpha_B)\frac{e^2}{a} + \frac{1}{2}K\delta^2 V_0$$

where α_S and α_B are the Madelung constants of the cation at positions *S* and *B*, *e* is the electronic charge, *a* is the nearest cation-cation distance, *K* is the bulk modulus, δ is the volume dilation and V_o is the atomic volume.

In the case of a single Li diffusion, only the mechanical work part attributes to the difference in barrier as the host material changes. The calculated diffusion barriers of Li in Si, Ge and Sn are 0.62, 0.44 and 0.39 eV, respectively. As expected, the diffusion barrier is the largest in Si, which is the stiffest among the host materials considered. Li diffusion in the presence of the second Li nearby is slightly more complex, and the Li-Li interaction (Madelung potential) can also affect the barrier value. A diffusion pathway of two Li interstitials is shown in Fig. 10.7. The diffusion barriers for Li in Si, Ge and Sn are lowered to 0.47, 0.35 and 0.33 eV under the influence of the Li repulsive potential. This prediction also implies it is more favorable for Li interstitials to remain isolated rather than clustered at low concentrations.

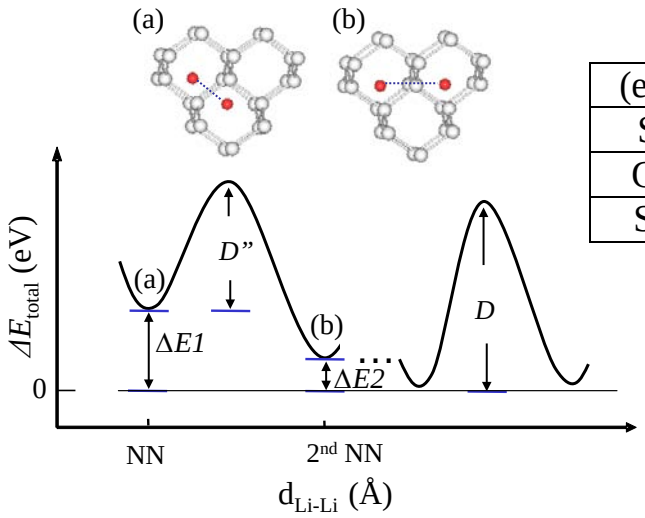

(eV)	*D"*	Δ*E1*	Δ*E2*
Si	0.47	0.19	0.04
Ge	0.35	0.27	0.15
Sn	0.33	0.08	0.01

Figure 10.7. The diffusion pathway of Li (red atom) with another Li nearby in a single element lattice, Si, Ge or Sn (white atoms). Li jumps from (a) to the next interstitial site (b). *D* indicates the diffusion barrier for the fully separated state.

10.3.5 Alloys Stabilities and Structures

Fig. 10.8 shows a variation in the mixing enthalpy for crystalline and amorphous Li-Si (a), Li-Ge (b) and Li-Sn (c) alloys as a function of Li:Si(Ge,Sn) composition ratio, with respect to crystalline Si, Ge, Sn and *bcc*-Li. The mixing enthalpy per atom (ΔE_{mix}) is given by:

$$\Delta E_{mix} = E_{Li_xX_{1-x}} - xE_{Li} - (1-x)E_X$$

where $E_{Li_xX_{1-x}}$ is the total energy per atom of the Li-*X* alloy examined (*X* = Si, Ge or Sn); *x* is the atomic fraction of Li; E_X and E_{Li} are the total energies per atom of *c*-*X* and *bcc*-Li, respectively.

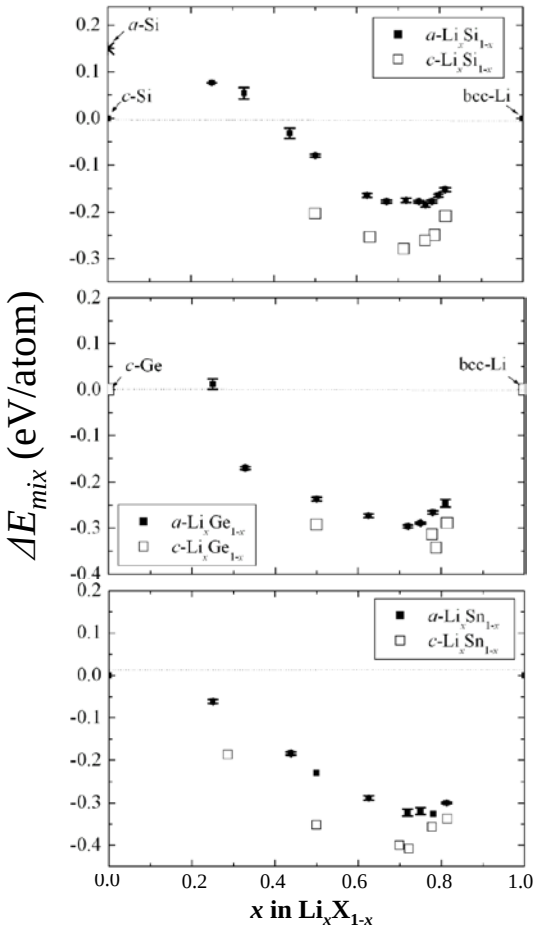

Figure 10.8. Variation in the mixing enthalpy for amorphous and crystalline Li-Si alloys as a function of Li content (at. %). The values for amorphous alloys are averaged based on 5 different 64-atom supercells.

The mixing enthalpy profiles for all three alloys share a common trend described in the previous work on Li-Si alloys [172]. The initially positive mixing enthalpy in Li-Si and Li-Ge alloys at < 40 at.% and 25 at.% Li decreases with increasing Li content and falls to a valley between 60 ~ 80 at.% Li; for crystalline phases, distinct minima are found at 71 at.% Li, and on average the crystalline phases have total energies ~ 0.05 to 0.1 eV/atom lower than their amorphous counterparts. A different characteristic is found in Li-Sn alloys in which the mixing enthalpies are negative even at very low Li contents. The mixing energy decreases in the order of Si (-0.17 eV/atom), Ge (-0.29 eV/atom), and Sn (-0.33 eV/atom), which is consistent with the trend predicted in the formation energy calculations, suggesting the incorporation/alloying of Li in Sn is particularly favorable. Based on the calculated mixing enthalpy values of Li-X amorphous and intermetallic compounds, we further expend the comparison to the alloys' glass forming ability (GFA), which can be expressed by

$$\text{GFA } \alpha \ \frac{\Delta H^{amor}}{\Delta H^{inter} - \Delta H^{amor}}$$

where ΔH^{amor} and ΔH^{inter} are the formation enthalpies of amorphous phase and intermetallic compounds, respectively.

The higher the absolute value of ΔH^{amor} and the smaller the enthalpy difference between the intermetallic phase and the amorphous phase are, the better the GFA is [172]. We find the glass forming ability increases in the order of Li-Si, Li-Sn, and Li-Ge, and for all three alloys, the GFA values are particularly high ~ 80 at.% Li.

Structurally, a general trend can also be observed in Li_yX alloys with varying Li contents (X = Si, Ge, Sn and y = 0 to 4.4). For crystalline phases, as Li content increases, the original tetrahedrally-bonded diamon network disintegrates into small clusters of different shapes [49-51]. As reported in the previous study, depending on the Li content, Li-Si alloys show various types of Si clusters, such as threefold-coordinated Si network, Si_5 rings and Si_4 stars , $Si_{7\sim3}$ string cluster, Si_2 dumbbells and single Si atom. Likewise, similar structural changes and clusters are to be expected in Li-Ge and Li-Sn alloys.

Next, we look at the structural evolution of the amorphous Li_yX alloy with varying Li contents from y = 0 to 4.4. The amorphous structures were characterized using pair distribution function (PDF, $g(r)$), which is defined as

$$g(r) = \frac{V}{N}\frac{n(r)}{4\pi r^2 \Delta r}$$

where n(r) represents particles in a shell within the region $r \pm \Delta r/2$, where Δr is the shell thickness; N denotes the number of particles in the model volume V.

Fig. 10.9 shows the pair-distribution functions for selected amorphous Li_yX alloys with the coordination numbers of corresponding cut-off radius presented in the insets; for each composition five independent 64-atom samples were used to obtain good statistics. No sharp second-neighbor peak is present, which confirms the amorphous nature (lack of long-range order) of the Li_yX alloys. As Li content increases, both X-Li and Li-Li peaks shift to shorter pair distance, as indicative of the increasingly favorable intermixing between Li and Si (Ge and Sn). The partial $g_{X\text{-}X}(r)$ of Li_yX alloys each exhibits a distinct first peak at 2.43 and 2.63, and 3.03 Å, which correspond to the presences of Si-Si, Ge-Ge and Sn-Sn dimers as their bond distances are 2.37, 2.49 and 2.80 Å, respectively. In all three Li_yX alloys, the intensity of the first $g_{X\text{-}X}(r)$ peak attenuates with increasing Li content; nevertheless, the presence of these peaks at y = 3.57 supports the existence of Si-Si, Ge-Ge and Sn-Sn dimers even in highly lithiated phases. Furthermore, it is noticed that the reduction in the first peak intensity is especially pertinent in LiSn alloys, suggesting the likelihood of Sn encaged by Li. A clearer comparison is shown in Fig. 10.10, in which the number of Si-Si, Ge-Ge and Sn-Sn neighbors is plotted as a function of Li content.

Based on the model structures, the variations in volume as a function of Li content were calculated as shown in Fig. 10.11; the volume of each alloy is normalized with respect to that of their crystalline phases. In both phases, volume increases nearly linearly with Li content. As expected, the crystalline phases are slightly denser than the amorphous counterparts. It is noticed that the volume deviation between crystalline and

amorphous phases is more significant in Li-Sn alloys, possibly due to the strong intermixing between Li and Sn, thereby large clustering of Sn-Li may be expected to form.

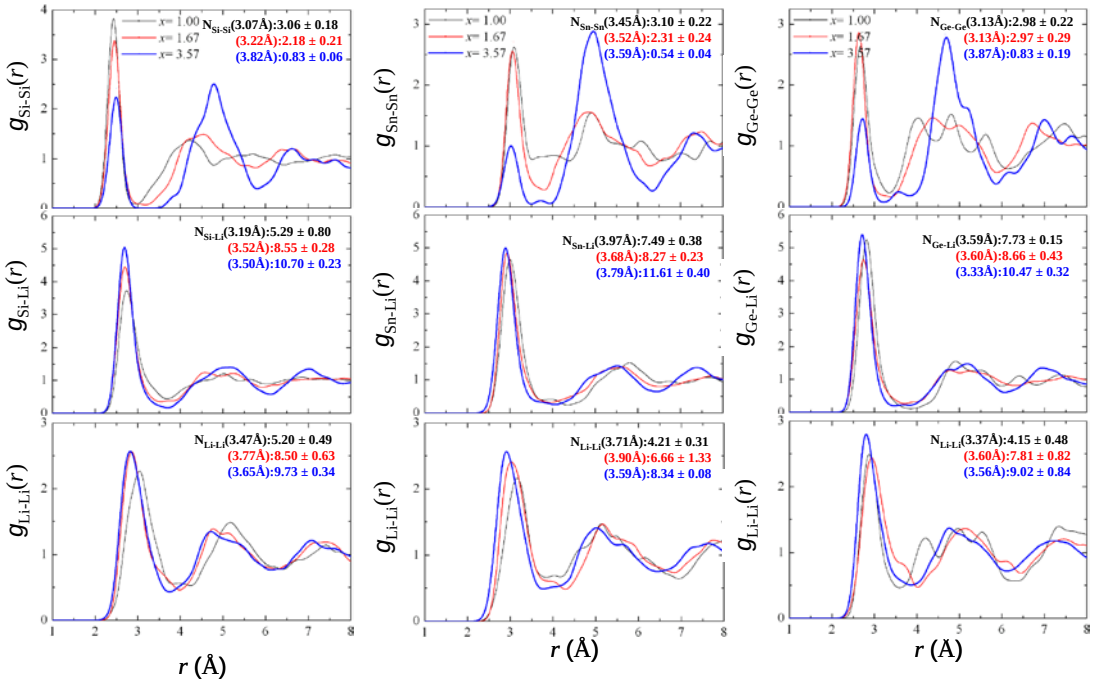

Figure 10.9. Partial pair-distribution functions for selected *a*-Li$_y$Si, *a*-Li$_y$Ge, and *a*-Li$_y$Sn for each composition; five independent 64-atom samples are used to obtain good statistics.

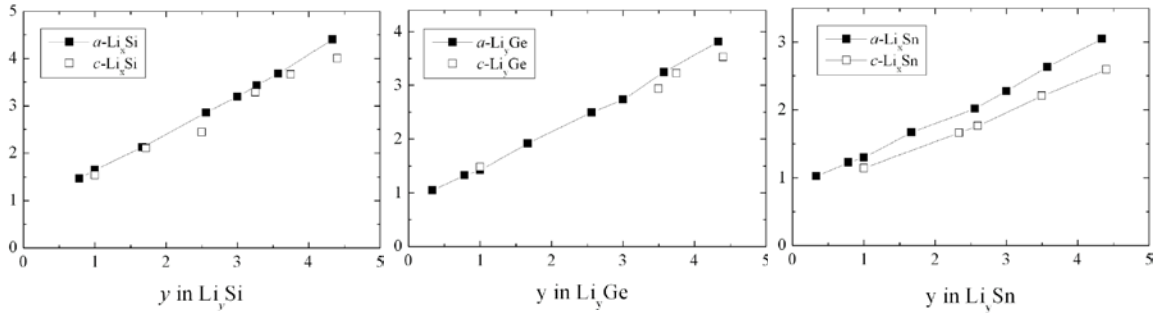

Figure 10.10. Variation in volume (solid circle and square) and density (open circle and square) of amorphous and crystalline Li-Si alloys as a function of Li content. The volume of each alloy is normalized with respect to that of *c*-X.

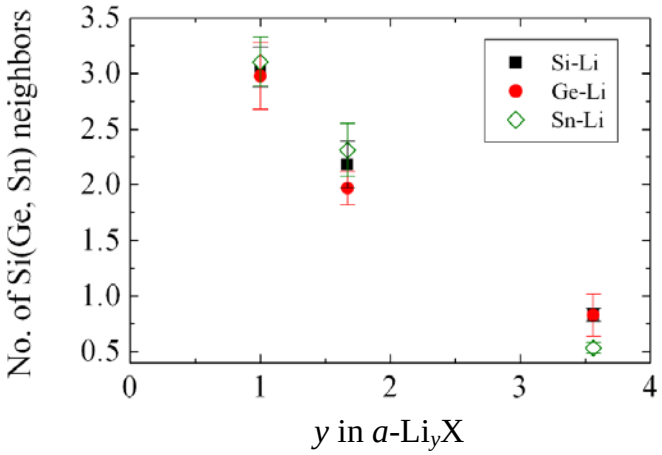

Figure 10.11. Coordination number of X(Si, Ge, and Sn) around X.

At highly lithiated state, volume expansion predicted in the order from small to larger is *a*-$Li_{4.33}Sn$ (200 %), *a*-$Li_{4.33}Ge$ (280 %), and *a*-$Li_{4.33}Si$ (334 %); attributed to the larger atomic size and hence the larger interstitial sites, Sn can more easily accommodate Li with less degree of lattice distance and volume expansion.

10.3.6. Electronic properties and elastic constants of alloys

We calculated the charge states of Si, Ge, Sn, and Li in *c*-Li_ySi, *c*-Li_yGe and *c*-Li_ySn using the grid-based Bader analysis [72]; special care was taken to ensure convergence with respect to the grid size. As summarized in Table 10.2, the Si charge state significantly varies from −0.84 to −3.08 with increasing Li content from y= 1 to 3.57, while the Li charge state remains nearly unchanged (+0.82 ~ +0.84). For all *c*-LiSi, *c*-LiGe, and *c*-LiSn alloys are composed of three-dimensional networks with each *X* connected to three other *X* atoms and receives 0.84~0.85 *e* from Li atom. For highly lithiated crystalline phases (*c*-$Li_{15}Si_4$, *c*-$Li_{15}Ge_4$, and *c*-Li_7Sn_2), both Si and Ge atoms are mostly isolated by 12 Li atoms, while Sn has two cases, one is one Sn and 12 Li atoms, another is 14 Li atoms as neighbors. In *c*-Li_7Sn_2 phase, Sn dimer may be given the charge from the Li leading to decreasing the charge gain. The charge states of Si, Ge, and Sn can be explained by general Zintl rules with the consideration that only partial charge is transferred from Li to Si.

Table 10.2. The charge states of X and Li in *c*-Li-X alloys calculated using the grid-based Bader charge analysis.

Element\Phases	*c* -LiSi	*c* -LiGe	*c* -LiSn	*c* -$Li_{15}Si_4$	*c* -$Li_{15}Ge_4$	*c* -Li_7Sn_2
Si,Ge,Sn	- 0.84	- 0.84	- 0.85	- 3.08[a]	-3.08[a]	- 3.30/-2.46[b]
Li	+ 0.84	+ 0.84	+ 0.85	+ 0.82	+ 0.82	+ 0.82

a: In $Li_{15}Si_4$, and $Li_{15}Ge_4$, each atom(Si or Ge) has 12 Li neighbors

b: In Li_7Sn_2, two different culsters are existed, one Sn atom has 14 Li neighbors, the other has 12 Li and 1 Sn neighbors.

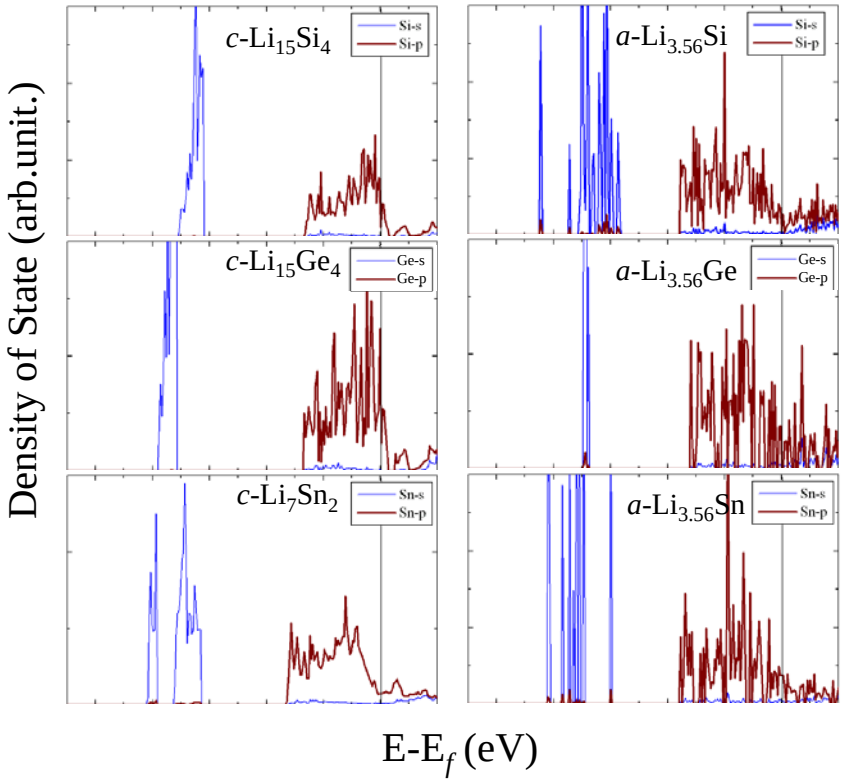

Figure 10.12. The electron density of states (DOS) projected on X atoms in various Li-X alloys in both amorphous and crystalline phases. The Fermi level is used as the reference energy state, which is set to zero.

Fig. 10.12 shows the electron density of states (DOS) projected on Si atoms in selected crystalline Li-Si alloys. The Fermi level is used as a reference energy, which is set to be zero. At high Li content for all phases, there is no trace of *s-p* hybridization and no band gap. This result is apparently attributed to the absence of Si-Si, Ge-Ge, and Sn-

Sn bonding interaction, as the covalent network loses its connectivity and disintegrates into smaller fragments.

Finally, we calculated the elastic constants of several crystalline phases of low and high Li contents to evaluate the effects on mechanical properties. Elastic constants, C_{ij} can be obtained by computing the energies of deformed unit cells. For cubic phases (LiGe, $Li_{15}Si_4$ and $Li_{15}Ge_4$), orthorhombic, isotropic and monoclinic distortions were applied to obtain three independent elastic constants, C_{11}, C_{12} and C_{44} (expressed using Voigt notations [173]). For tetragonal phases (LiSi, Li_2Sn_5 and Li_7Sn_2), six independent deformation modes were applied to calculate C_{11}, C_{12}, C_{13}, C_{33}, C_{44} and C_{66}. Self-consistent relaxation are allowed in all strained unit cells, and the total energy change with respect to the strain tensor gives [173]

$$E(e_{ij}) = E_0 - P(V)\Delta V + \frac{V}{2}\sum_{ij} C_{ij}e_{ij} + O[e_{ij}^3]$$

where E_0 and $E(e_{ij})$ are the internal energies of the initial and strained lattices, respectively; V is the volume of the unstrained lattice; $P(V)$ is the pressure of the undistorted lattice at volume V; ΔV is the change volume; e_{ij} is the strain tensor; $O[e_{ij}^3]$ indicates the neglected terms in the polynomial expansion.

The parameterizations of strains used are shown in Table 10.3. For each of the strains, we performed calculations for seven values of γ ranging from −0.01 to 0.01. Elastic constants calculations require a high degree of precision because the energy variation involved is very small; the geometry optimization were performed at cutoff energy of 350 eV and force tolerance of 0.005 eV. Once C_{ij} values are known, the bulk modulus can be calculated as

$$B = 1/9(C_{11} + C_{22} + C_{33} + 2C_{12} + 2C_{13} + 2C_{23}).$$

The computed elastic constants and bulk moduli are summarized in Table 10.4. The calculated $B_{c\text{-}SiLi}$ = 64.78 GPa and $B_{c\text{-}Si15Li4i}$ = 32.36 GPa are in good agreement with the theoretical value of 53.0 GPa and 30.0 GPa [173], respectively. The bulk moduli indeed decrease with increasing Li content leading to significant elastic softening. For a given Li content, Li-Ge and Li-Sn alloys tend to be softer than the Li-Si alloy.

Table 10.4 shows the elastic parameters for *c*-Li_xSi and *c*-Li_xGe, and *c*-Li_xSn alloys at selected compositions of x = 0.4~1 and x = 3.5~3.75. The calculated bulk moduli for $B_{c\text{-}SiLi}$ = 64.78 GPa and $B_{c\text{-}Si15Li4i}$ = 32.36 GPa are in good agreement with the theoretical value of 53.0 GPa and 30.0 GPa [173], respectively. The bulk moduli indeed decrease with increasing Li content leading to significant elastic softening. For a given Li content, the Ge and Sn alloys tends to be softer than the Si-Li alloy.

Table 10.3. Parameterizations of the strains used to calculate elastic constants of cubic LiGe, $Li_{15}Si_4$ and $Li_{15}Ge_4$, and tetragonal LiSi, Li_2Sn_5 and Li_7Sn_2.

Strain	Parameters (unlisted e_{ij}=0)	$\Delta E/V$
	cubic phase	
1	$e_1 = e_2 = \gamma$, $e_3 = (1+\gamma)^{-2} - 1$	$3(C_{11} - C_{12})\gamma^2$
2	$e_1 = e_2 = e_3 = \gamma$	$3/2(C_{11} + 2C_{12})\gamma$
3	$e_6 = \gamma$, $e_3 = \gamma^2(4-\gamma^2)^{-1}$	$1/2C_{44}\gamma^2$
	tetragonal phase	
1	$e_1 = 2\gamma$, $e_2 = e_3 = -\gamma$	$1/2(5C_{11} - 4C_{12} - 2C_{13} + C_{33})\gamma^2$
2	$e_1 = e_2 = -\gamma$, $e_3 = 2\gamma$	$(C_{11} + C_{12} - 4C_{13} + 2C_{33})\gamma^2$
3	$e_1 = e_2 = \gamma$, $e_3 = -2\gamma$, $e_6 = 2\gamma$	$(C_{11} + C_{12} - 4C_{13} + 2C_{33} + 2C_{66})\gamma 2$
4	$e_1 = \gamma$	$1/2C_{11}\gamma^2$
5	$e_3 = \gamma$	$1/2C_{33}\gamma^2$
6	$e_4 = 2\gamma$	$1/2C_{44}\gamma^2$

Table 10.4. Calculated elastic parameters for Li-Si, Li-Ge, and Li-Sn alloys.

Phase	*C11*	*C33*	*C12*	*C13*	*C44*	*C66*	*B*
c-LiSi	109	71.67	24.92	39.03	54.58	37.93	55.07
c-LiGe	*72.1*	*43.48*	*27.24*	*30.45*	*23.78*	*13.91*	40.44
c-Li_2Sn_5	96.41	136.39	111.87	28.75	112.75	9.31	74.22
c-$Li_{15}Si_4$	55.87		20.61		33.93		32.36
c-$Li_{15}Ge_4$	43.1		19.78		30.98		27.55
c-Li_7Sn_2	61.49	88.56	22.08	3.286	63.30	40.89	29.87

10.4 Summary

Using DFT-GGA calculations we examined the structure, stability, diffusion, and bonding mechanism of a single Li interstitial atom in *c*-X in the neutral charge states. We also looked at the interaction between two Li interstitials and the effect of Li incorporation on the stability of the X lattice. The tetrahedral (T) state turns out to be energetically most favored. Our DFT calculation shows that interstitial Li may undergo diffusion with a moderate barrier of ≈ 0.62, 0.44, and 0.39 eV in Si, Ge, and Sn matrix, respectively. We also find that the interaction between Li^0 interstitials is repulsive due to their positive ionization; the diffusion barriers for Li in Si, Ge, and Sn are lowered to 0.47, 0.35, and 0.33 eV under the influence of the Li repulsive potential. This implies that Li interstitials favorably remain isolated, rather than clustered. The incorporation of Li^0 at the T site results in noticeable outward displacement of the four X first neighbors by ~ 0.08 Å from their crystalline positions. Our calculation also shows that the charge transferred from Li^0 is largely localized within the first and second nearest Si lattice atoms, while the charge transferred from Li^0 in the Ge and Sn matrix spread to the 3rd and 4th nearest neighbors, respectively. This result indicates that the positively ionized Li interstitial may be effectively screened by the transferred electron in Si and less so in Sn.

Our analysis of electronic density of states (DOS) highlights that the electron transfer leads to partial filling of the anti-bonding sp3 states of neighboring Si atoms, which in turn weakens corresponding X-X bonds. This also clearly indicates that the host X lattice can be easily destabilized by Li insertion.

In the second part, we examined the energetics, structure, electronic and mechanical properties of crystalline and amorphous Li-X alloys. According to our mixing enthalpy calculations, the mixing energy decreases in the order of Si (-0.17 eV/atom), Ge (-0.29 eV/atom), and Sn (-0.33 eV/atom), which is consistent with the trend predicted in the beforementioned formation energy calculations, suggesting the incorporation/alloying of Li in Sn is particularly favorable.

With increasing Li content, we find that: i) the tetrahedrally bonded Si network undergoes disintegration into low-connectivity clusters of various shapes; ii) the *a*-Li-Si

becomes more densely packed as evidenced by the increasing CN; iii) Si-Si PDF peaks shift toward larger *r* values as a result of weakened X-X bonds. Bader charge analysis shows that while the charge state of Li remains nearly unchanged around ~ +0.84, that of Si varies significantly from −0.85 to −3.30 depending on the number of X neighbors as can be understood by Zintl rules. Our electronic DOS analysis illustrates that towards higher lithiated states, the Si *s*-*p* splitting grows larger accompanied by weakening/breaking of X-X bonds and changes in the alloy structure. Due to the softening of Si network, the bulk modulus decreases almost linearly with increasing Li content. The electronic analysis also reveals the band gap narrowing with increasing degree of lithiation, showing more metallic character. The fundamental findings assist in understanding the dynamic behavior of Li atoms and the nature of their interaction with the host X matrix particularly during the early stages of lithiation and the nature of Li-Si alloys further, and the present work can also provide a framework for the study of various lithiated alloys.

Chapter 11:

The Structure and Properties of amorphous Li-X (X; Si, Sn, $Si_{0.75}Sn_{0.25}$) system.

11.1 Introduction

Li-X (Si, Sn and Si+Sn) alloys have great promise as anode materials for the lithium ion battery (LIB). There can be several reasons for enhancing the demand for specific capacity, rate capability, and a low voltage. The amorphous phase, which has superior features over crystalline phase, in anode materials, has the potential to expand the volume homogeneously and show smooth voltage profiles. Specifically, amorphous SiSn alloy creates large specific capacities over many cycles reversibly. The reason for good cycling capacity of this alloy is attributed to the absence of the phase transformation undergone by most tin-containing materials. This lithiation reaction is estimated to give volume expansion on the order of 250% for $Li_{4.33}Si_{0.75}Sn_{0.25}$, which is compared to the volume expansions, 300 % and 200 % for $Li_{4.33}Si$ and $Li_{4.33}Sn$, respectively. The amorphous silicon-tin alloy provides several advantages over the binary Si-Li and Sn-Li system such as homogeneous lower volume expansion than the pure Si and flexibility for Li to diffuse in/out. Recently, Dahn et al. sputtered the amorphous Si-Sn film and then showed that the electrochemical reaction with Li is reversible for long cycles [41, 44, 159, 160]. Understanding of the structural evolution during lithiation/delithiation for alloys is lacking due to the features of amorphous. In this chapter, we focus on the amorphous structural stability of host semiconductor alloys, Si-Sn, and amorphous Li-Si-Sn structural evolution as Li content increase. Density functional theory (DFT) is used to examine the Li-Si-Sn ternary system and morphology changes that occur in amorphous Li-Si-Sn alloy as it react with lithium.

11.2 Computational method

The model structures of amorphous Li-Si-Sn alloys were created using AIMD simulations based on the atomic configurations of Li-Si alloys that were previously

obtained using combined modified embedded atom method (MEAM) and AIMD simulations (see Ref. 5 for detailed computational methods). According to the previous study [84], Au and Si atoms in the bulk Li-Si amorphous alloy are overall well mixed with no segregation. The Li-Si interaction differs from the Li-Si interaction in nature, and thus the local atomic configurations (or short-range order) of the alloys tend to be dissimilar. Nonetheless, the Li-Si structure is likely a good starting configuration for the Li-Si-Sn amorphous structure (where Sn and Si atoms are overall well distributed as well); in particular, the high mobilities of Li and Si at high temperatures (> 1000 K) allow facile local structure rearrangements. With Li-Si alloy configurations, Si atoms were replaced with Sn atoms, the alloys were annealed at 1,000 K for 2 picoseconds (*ps*) with a time step of 1 femtosecond (*fs*), and then rapidly quenched to 300 K at a rate of 0.4 K/fs, along with volume optimization. Each model structure contains a total of 64 Li, Si, and Sn atoms. Here, the temperature was controlled via velocity rescaling. This approach can provide reasonable Li-Si-Sn amorphous structures at significantly reduced computational burden compared to starting with crystalline initial configurations.

The calculations reported herein were performed on the basis of density functional theory (DFT) within the generalized gradient approximation (GGA-PW91 [65]), as implemented in the Vienna *Ab initio* Simulation Package (VASP) [21, 66, 67]. Spin polarization of the Li-Si system was also examined, but appears to be insignificant. The projector augmented wave (PAW) method with a planewave basis set was employed to describe the interaction between ion cores and valence electrons. The PAW method is, in principle, an all-electron frozen-core approach that considers exact valence wave

functions. Valence configurations employed are: $1s^2 2s^1$ for Li, $3s^2 3p^2$ for Si, and $4d^{10} 5s^2 5p^2$ for Sn. An energy cutoff of 350 eV was applied for the planewave expansion of the electronic eigenfunctions. During geometry optimization, all atoms were fully relaxed using the conjugate gradient method until residual forces on constituent atoms become smaller than 5×10^{-2} eV/ Å. A (2×2×2) k-point mesh in the scheme of Monkhorst-Pack was used for the Brillouin zone sampling [111] for all amorphous structures.

11.3 Result and Discussion

11.3.1 Amorphous $Si_{0.75}Sn_{0.25}$

Silicon or Sn pulverize rapidly when cycled during lithiation/delithiation due to the large volume change. This structural rearrangement leads to the mechanical stress on the host structure. Therefore, the host alloying materials should be chosen to improve the dimensional stability and thus the reversibility for higher lithium uptakes. Recently, the Si-Sn alloy has been shown to have good electrochemical properties.

Beaulieu et al. studied about the amorphous Si-Sn alloy, which have been prepared by sputtering Si and Sn targets in radio-frequency magnetron sputtering equipment. All samples sputtered by RF with $n < 0.36$ in Sn_xSi_{1-x} are amorphous and all samples with $n > 0.4$ show evidence for crystalline Sn precipitates [44]. They also found that the film with $n = 0.36$ can undergo reversible colossal volume expansion; thus, improved charge-discharge cycling behavior. Maruyama et al. also studied thin films of amorphous Si-Sn, which have been prepared by sputtering Si and Sn targets with radio-frequency magnetron sputtering equipment. They found that the film of $n < 0.28$ is amorphous but that crystalline β-Sn is formed in the amorphous film for $x > 0.28$ [174].

We select the composition of $Si_{0.75}Sn_{0.25}$ as a model structure to ensure the amorphous phase. The host amorphous structure is modeled by adopting a 64 amorphous Si atom supercell constructed from the continuous random networking (CRN) model. The

Sn concentration (25 at. %) is modeled by distributing Sn atoms in the substitutional site of Si, which maximizes the Sn-Sn bond length within the supercell. This configuration is found to be preferable energetically. The topology of our model is determined through the pair distribution function (PDF), rigidity and optimized volume. The PDF for the model structure consisting of 25 at. % of Sn in the 64-supercell is shown in Fig. 11.1. The total coordination number around Si and Sn at the cutoff radius of 3.15 Å and 3.50 Å are predicted to be 4 and 4, respectively, demonstrating that both Si and Sn maintain tetrahedral network as shown in the inset of Fig. 11.1. From the integration of the first peak of partial PDF, the partial coordination number around Si is calculated to be 2.83 of Si neighbors, 1.17 of Sn neighbors, while the partial coordination number around Sn is 3.5 of Si neighbors and 0.5 Sn neighbors. The small intensity of first peak in $g_{Sn\text{-}Sn}(r)$ is indicative of the small existence of Sn dimmers.

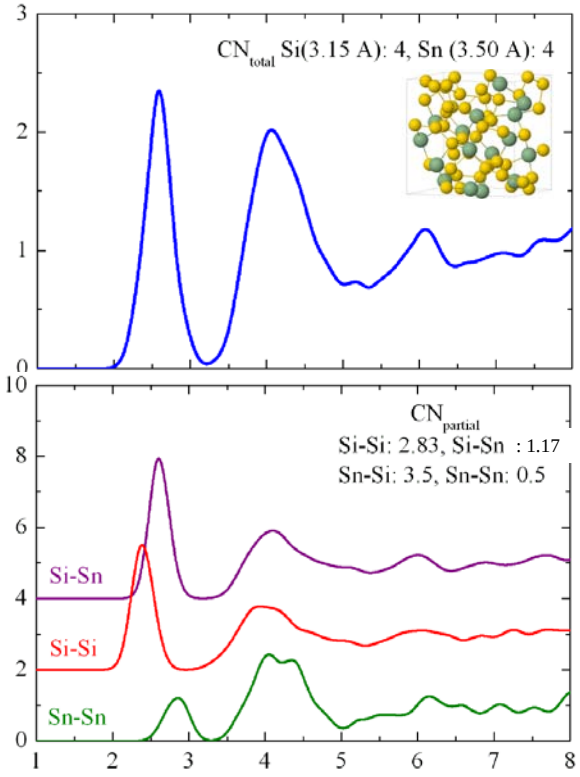

Figure 11.1. Total and partial distribution function for a-$Si_{0.75}Sn_{0.25}$.

To evaluate the topological rigidity of tetrahedral lattice, we used the parameter

*a*** which is defined by Cai and Thrope [175, 176]. It is a measure of force required to produce a unit displacement. For a rigid lattice, $0 \leq a^{**} \leq 0.5$ ($a^{**} = 0$ is a perfectly rigid lattice), and for a soft lattice, $0.5 \leq a^{**} \leq 1$ ($a^{**} = 1$ is the floppy limit).

For Sn_nSi_{1-n} alloys the definition of the topological rigidity parameter *a*** can be shown as

$$\langle L_{SiSi} \rangle = Le - n\, a^{**}(L^0_{SnSn} - L^0_{SiSi}),$$

$$\langle L_{SnSn} \rangle = \langle L_{SiSi} \rangle + a^{**}(L^0_{SnSn} - L^0_{SiSi}),$$

$$\langle L_{SnSi} \rangle = \tfrac{1}{2}(\langle L_{SiSi} \rangle + \langle L_{SnSn} \rangle),$$

$$Le = n\, L^0_{SnSn} + (1-n)\, L^0_{SiSi},$$

L^0_{SiSi} and L^0_{SnSn} are the Si-Si and Sn-Sn bond lengths calculated for crystalline Si and amorphous Sn, respectively, and $\langle L_{SiSi} \rangle$, $\langle L_{SiSn} \rangle$, and $\langle L_{SnSn} \rangle$ are the Si-Si, Si-Sn, and Sn-Sn mean bond lengths in Sn_xSi_{1-x} alloy of composition x. The calculated mean bond lengths are Si-Si: 2.35 Å, Si-Sn: 2.58 Å, and Sn-Sn: 2.81 Å. By fitting the calculated data with these expressions the topological rigidity parameter *a*** determined is 0.67 for *a*-$Si_{0.75}Sn_{0.25}$, which is compared to the calculated *a*** of 0.69, 0.63 for Sn_nGe_{1-n}, Si_nGe_{1-n}, respectively. The soft lattice of *a*-Si-Sn may enhance the Li mobility in the host structure during lithiation/delithiation.

11.3.2 Formation energy and electrochemical analysis for the *a*-$Li_xSi_{0.75}Sn_{0.25}$

Fig. 11.2a shows the variation in formation energy as a function of Li content for an amorphous Li-Si-Sn alloy system with respect to the bulk crystalline Si, Sn, and Li. The Gibbs free energy, ΔG, is given by:

$$\Delta G = \Delta E + P\Delta V - T\Delta S \qquad (11\text{-}1)$$

While the internal energy term (ΔE) is ~ 1 eV per Li atom, the contributions from work ($P\Delta V$) and entropy ($T\Delta S$) terms are only in the magnitude of ~ 10^{-5} eV and the thermal energy (k_BT) of ~ 2.5 x 10^{-2} eV at 298 K, respectively. Hence, a fair approximation of $\Delta G \approx \Delta E$ can be made. The formation energy per Si atom (E_f) is

computed by:

$$E_f(x) = E_{\mathrm{LixSi0.75Sn0.25}} - (xE_{\mathrm{Li}} + 0.75E_{\mathrm{Si}} + 0.25\mathrm{E}_{\mathrm{Sn}}), \qquad (11\text{-}2)$$

which has been used in the reaction for

$$\mathrm{Li}_x\mathrm{Si}_{0.75}\mathrm{Sn}_{0.25} + \Delta x\mathrm{Li} \rightarrow \mathrm{Li}(x+\Delta x)\mathrm{Si}_{0.75}\mathrm{Sn}_{0.25} \quad (11\text{-}3)$$

where Δx is the number of lithium transferred, $E_{\mathrm{LixSi0.75Sn0.25}}$ is the total energy of the $\mathrm{Li}_x\mathrm{Si}_{0.75}\mathrm{Sn}_{0.25}$ structure divided by the numbers of Si and Sn atoms, x is the atomic fraction of Li, E_{Li} is the total energy of a single Li atom in bcc Li, E_{Si} is the total energy of a single Si atom in a diamond lattice, and E_{Sn} is the total energy of a single Sn atom in a diamond lattice. For comparison, the formation energies per Si atom for *a*-$\mathrm{Li}_x\mathrm{Si}$ and *a*-$\mathrm{Li}_x\mathrm{Sn}$ are presented in Fig. 11.2a.

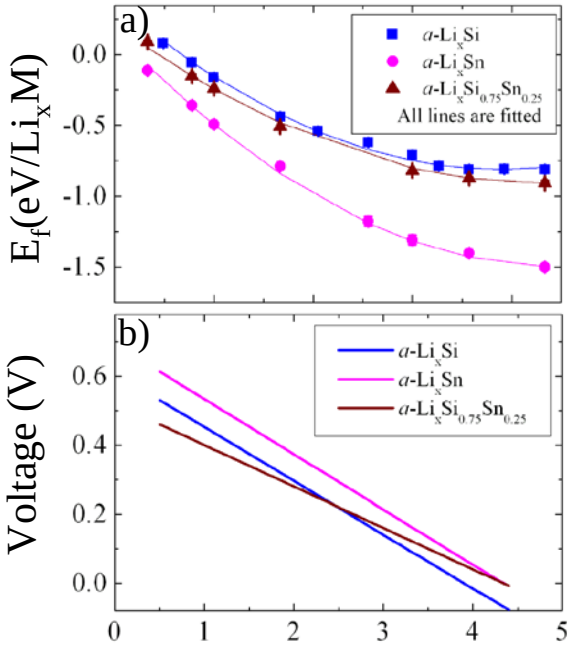

Figure 11.2. a) The variation in formation energy as a function of Li content for an amorphous Li-Si-Sn alloy system with respect to the bulk crystalline Si and Li. b) Calculated voltage profile of *a*-$\mathrm{Li}_x\mathrm{Si}_{0.75}\mathrm{Sn}_{0.25}$.

Overall, the formation energies approach a minimum close to x = 4. The formation energies of *a*-$\mathrm{Li}_x\mathrm{Si}_{0.75}\mathrm{Sn}_{0.25}$ are within those of *a*-$\mathrm{Li}_x\mathrm{Si}$ and *a*-$\mathrm{Li}_x\mathrm{Sn}$, more

closely to Li-Si than Li-Sn, indicating that the Li and Si or Sn has an intermixing interaction and the system will be randomly alloyed. This fact is compared with an experimental study about the reaction of Li with amorphous $Si_{0.66}Sn_{0.34}$ alloy [[44]. From in situ X-ray diffraction (XRD), they found that this material remains amorphous throughout all portions of the charge and discharge profile, in the range $0 < x < 4.4$ in $Li_xSi_{0.66}Sn_{0.34}$. The formation energy of $Li_xSi_{0.75}Sn_{0.25}$ shows the similar trend with that of Li_xSi with an energy gain of 0.1 eV/formula. It is also noted that the formation energies for Li_xSn have relatively lower values than those of Li_xSi and Li_xSiSn. The strong attractive interaction between Sn and Li may enhance the Li trap around Sn atoms, instead of Si atoms; thus it may localize the Si and Sn clusters.

Incorporation of Li atoms into the Si (Sn) anodes leads to an increase in the chemical potential and subsequently a decrease in voltage. Using the definition of Gibbs free energy and the Nernst equation, the electric potential of a $Li_xSi(Sn)$ anode can be approximated by Equation (11-4) [177, 178].

With the calculated formation energy, the cell voltage is also defined as

$$V = - \Delta E_f(x)/\Delta x \quad (11\text{-}4)$$

This approach has been successfully applied to compute the potential variation as a function of Li content in a variety of electrode materials including Li-Si alloys and Li-Sn alloys. The voltage profile presented in Fig.11.3b seems to be in good agreement with the experimental result, and all of our data points fall within the experimental lithiation/delithiation curve reported in the recent literature [44].

Figure 11.2b shows the potential vs. composition curve constructed using Equation (11-6) and numerical regression method. The fitted curve for *a*-Li-Si has a deviation at the region of $x = 2\sim3$. The formation energy of *a*-$Li_{2.56}Si$ is somewhat higher than that of the neighboring alloys (*a*-$Li_{1.67}Si$ and *a*-$Li_{3.0}Si$) as shown in Fig. 11.4. This leads to smoothly varying voltage profile near $x = 2$ and subsequent voltage drop near $x = 3$. However, in our study we used one secondary equation to compare the results for three

systems. The fitted curves of *a*-Li_xSn and *a*-Li_xSi-Sn are all well fitted with a secondary equation. The parameters in a secondary equation, $y= y_0 + \gamma(x-x_0)^2$, are summarized in Table 11.1.

Table 11.1. The computed parameters for *a*-Li_xSi, *a*-Li_xSn, and *a*-$Li_xSi_{0.75}Sn_{0.25}$.

	γ	y_0	x_0
a-Li_xSi	0.078	- 0.812	3.9
a-Li_xSn	0.082	- 1.500	4.5
a-$Li_xSi_{0.75}Sn_{0.25}$	0.060	- 0.909	4.3

As shown in Fig. 11.2, the *a*-$Li_xSi_{0.75}Sn_{0.25}$ has lower slope in the voltage profile than the *a*-Li_xSi and *a*-Li_xSn. This result indicates that the *a*-$Li_xSi_{0.75}Sn_{0.25}$ may be possible to extend the electrical performance during lithiation/delithiation

11.3.3 Amorphous structures analysis for *a*-$Li_xSi_{0.75}Sn_{0.25}$

We looked at the structural evolution of the amorphous $Li_xSi_{0.75}Sn_{0.25}$ alloy by varying Li content at x = 1, 1.67, and 3.57. Fig. 11.3 shows the total and partial pair-distribution functions for the optimized configurations at selected Li contents; for each composition five independent 64-atom samples were used for good statistics. In the analysis, we notice several features with increasing Li contents: i) the higher peak at x = 3.57 in the total distribution function is due to the correlations from first-neighbor Li atoms. ii) the Si-Si peak gradually becomes smaller with slightly increasing bond distance while the Li-Li peak gradually becomes stronger; iii) the Si-Si and Sn-Sn peaks gradually becomes distinctive, and the Sn-Sn first peak at x = 3.57 disappear.

In the amorphous phase, Si atoms still form Si-Si pairs even in highly lithiated *a*-$Li_{3.57}Si_{0.75}Sn_{0.25}$, instead of remaining completely isolated as seen in the crystalline counterparts (*c*-$Li_{15}Si_4$, *c*-$Li_{22}Si_5$, and *c*-$Li_{22}Sn_5$). However, Sn atoms are fully surrounded by Li atoms as an evidence of disappearance of first nearest peak in PDF and the calculated partial coordination number of 0 for the Sn atom.

It is believed that the tetrahedral network in the ternary alloy (Li-Si-Sn) is more prominent than the binary alloy (Li-Si) in highly lithiated phase. To verify the evolution of the covalent bonded network between Si-Si and Si-Sn depending on the Li content, we integrated the first peak of the partial PDF to calculate the coordination number. As shown in Fig. 11.4, initial host matrix of Si, Sn, and $Si_{0.75}Sn_{0.25}$ have 4 Si, Sn, and Si+Sn neighbors, respectively, around Si, i.e., $CN_{Si-Si} = 4$, $CN_{Sn-Sn} = 4$, and $CN_{Si-(Si+Sn)} = 4$, while there are $CN_{Si-Si} = 2.23$ and $CN_{Si-Sn} = 0.6$ at $x = 1$, $CN_{Si-Si} = 2.11$ and $CN_{Si-Sn} = 0.43$ at $x = 1.67$, and $CN_{Si-Si} = 0.76$ and $CN_{Si-Sn} = 0.24$ at $x = 3.57$. In highly lithiated phase of *a*-$Li_{3.57}Si_{0.75}Sn_{0.25,}$ the Si atom has 1(0.76(Si)+0.24(Sn)) nearest neighbor. This result is somewhat higher than that the value of Si neighbor (0.82) in the binary Li-Si alloy.

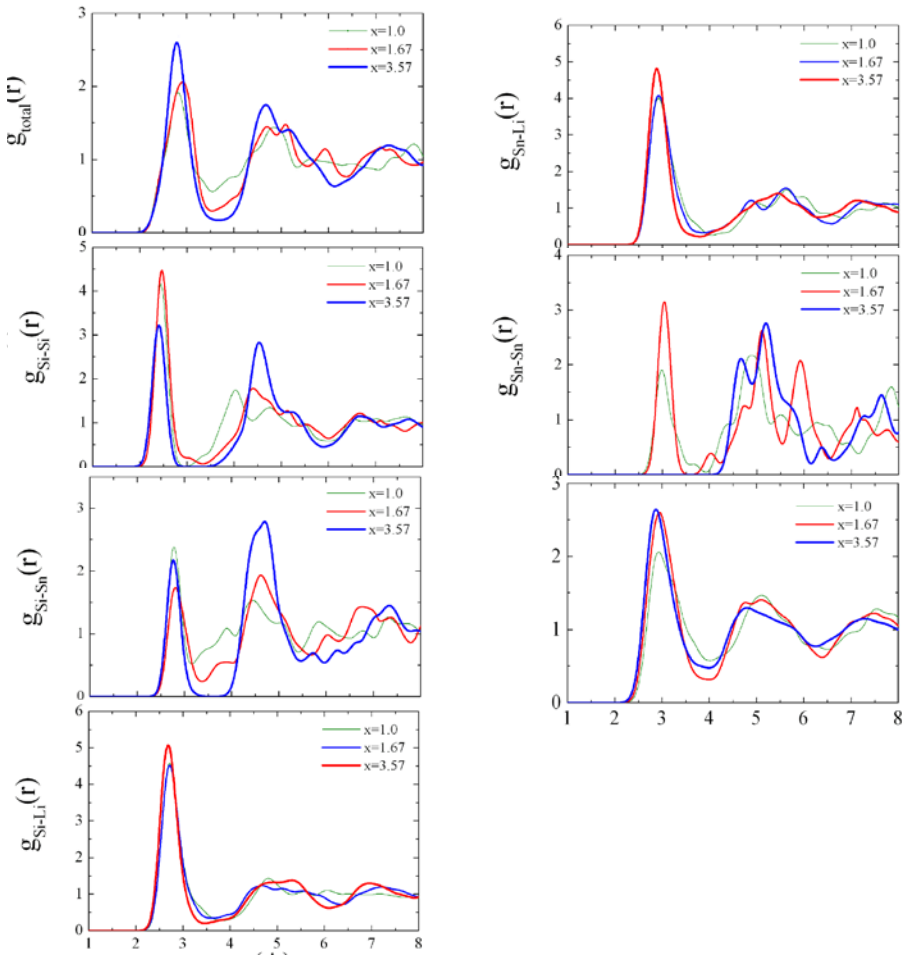

Figure 11.3. Total and partial pair-distribution functions for *a*-$Li_xSi_{0.75}Sn_{0.25}$ with x = 1, 1.67, and 3.57.

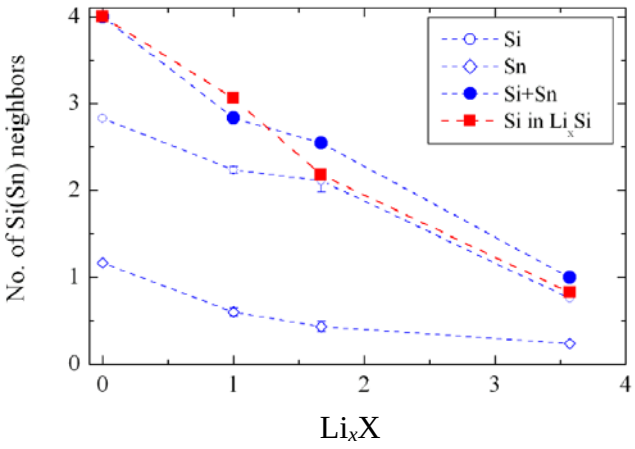

Figure 11.4. Coordination number of Si and Sn around Si

At x = 1, which is considered as initial lithiation (or final delithiation), the Si atom has 2.83 Si and Sn neighbors, which is also below the coordination number of Si in the binary Si-Li system. In terms of structural effects, the low coordination number at x = 1 leads to smoothness that make a room for Li atoms to move more freely than in the binary Si-Li system, which has CN of 3. The closer network of the host matrix in *a*-$Li_{3.5}Si_{0.75}Sn_{0.25}$ and sparser network of the host matrix in *a*-$LiSi_{0.75}Sn_{0.25}$ may enhance the structural stability during lithiation/delithiation.

Fig. 11.5 shows the variation of the number of Li neighbors around Si and Sn at selected Li content. As Li content increases from x = 1 to x = 3.57, the Li neighbors increase from 6.73 to 9.88 around Si, while from 8.1 to 11.2 around Sn. For comparison, on average the Li neighbors around Si are 5.29 and 10.7 in *a*-LiSi and *a*-$Li_{3.5}Si$, respectively, while the Li neighbors around Sn are 7.49 and 11.61 in *a*-LiSn and *a*-$Li_{3.5}Sn$ [174], respectively.

Higher Li neighbors at x = 1 and lower Li neighbors at x =3.57 in the ternary system than in binary system indicate that the ternary system provides opportunity for Li atom to be more released from the host matrix at x = 1 and more room for Li atom to be stored in the host matrix at x = 3.57.

This is believed to be extendable in the electrochemical performance in the ternary Si-Sn-Li system.

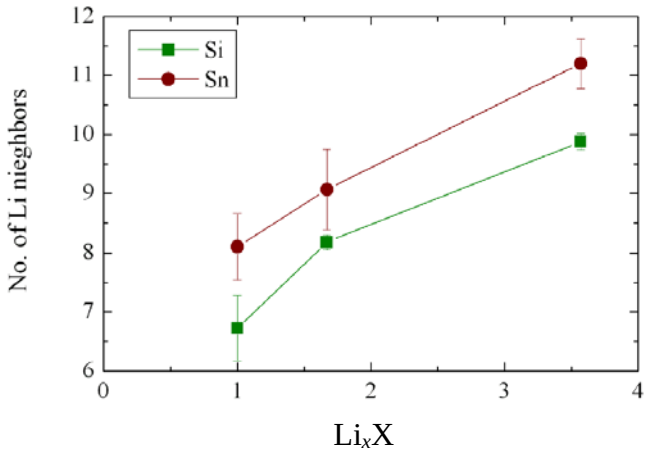

Figure 11.5. Coordination number of Li around Si and Sn

As shown in Fig. 11.6, we estimated a change in the volume of *a*-$Li_xSi_{0.75}Sn_{0.25}$ as a function of Li content. The volume expansion for an alloy anode is normalized with respect to the host lattice: atomic volume in diamond Si for *a*-Li_xSi, atomic volume in diamond Sn for *a*-Li_xSn, and atomic volume of *a*-$Si_{0.75}Si_{0.25}$ for *a*-$Li_xSi_{0.75}Sn_{0.25}$.

The predicted volume expansion from the amorphous host structure ($Si_{0.75}Sn_{0.25}$) of ≈ 279 % for fully lithiated $Li_{4.4}Si_{0.75}Sn_{0.25}$ is in good with the experimental result of 250 % for $Li_{4.4}Si_{0.66}Sn_{0.34}$ from in situ AFM [41].

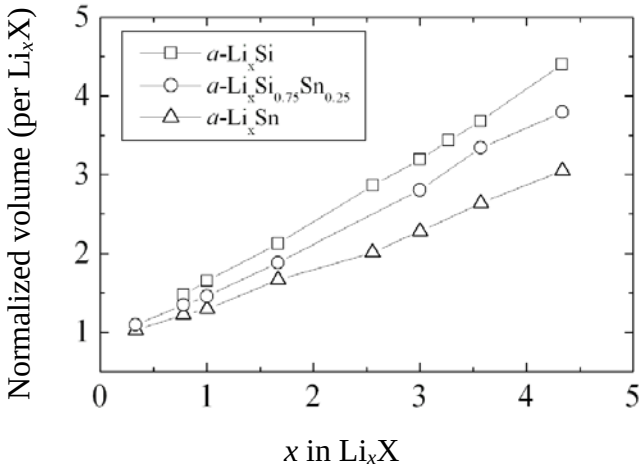

Figure 11.6. Variation of volume with respect to the pristine structure.

11.3.4 Electronic properties and bulk moduli of *a*-$Li_xSi_{0.75}Sn_{0.25}$

Fig. 11.7 shows the electron density of states (DOS) projected on Si atom and Sn atoms in selected amorphous Li-Si-Sn alloys. The analysis could demonstrate how the Si-Si and Sn-Sn bonding property changes as a function of Li content. The Fermi level is used as a reference energy, which is set to be zero. As expected, the degree of *s-p* hybridization decreases; note that the splitting between *s* and *p* states in *a*-$LiSi_{0.75}Sn_{0.25}$ is larger than that in *a*-$Li_{3.57}Si_{0.75}Sn_{0.25}$, as a result of the decreased Si-Si and Sn-Sn bonding interaction. In addition, the degree of s-p hybridization of Sn in *a*-$Li_{3.57}Si_{0.75}Sn_{0.25}$ is relatively smaller than that of Si, due to the smaller amount of Sn dimers than Si dimers as shown in Fig. 11.3.

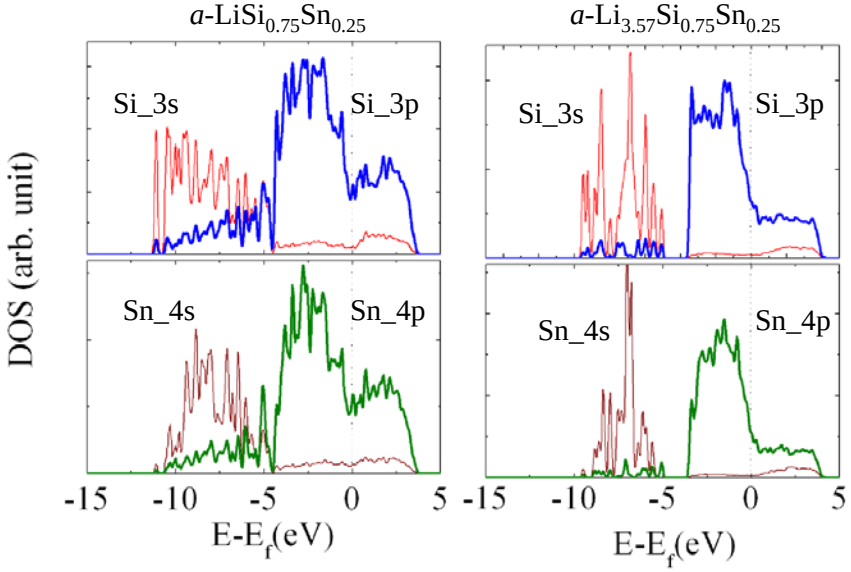

Figure 11.7. Density of State for *a*-$Li_xSi_{0.75}Sn_{0.25}$

As mentioned in our previous calculations, the gradual structural transformation is due to the softening of Si-Si bond strength as the Li content increases.

Finally, we looked at how the changes in the atomic and electronic structures affect the mechanical properties of Li-Si-Sn alloys. Here, we only calculated the bulk modulus (*B*) for the selected alloy, which can be determined by fitting the Murnaghan equation of state [73] to the corresponding energy versus volume curve. In our

calculations, uniform tensile and compressive stresses were imposed on the alloys to achieve ± 10 % volume variation.

The calculated bulk moduli for *c*-Si and *bcc*-Li are $B_{c\text{-}Si}$ = 87.8 GPa and $B_{bcc\text{-}Li}$ = 12.7 GPa, in good agreement with the experimental values of $B_{c\text{-}Si}$ = 100.0 GPa [140] and $B_{bcc\text{-}Li}$ = 13.3 GPa (78 K) [179]. The bulk moduli of a-$LiSi_{0.75}Sn_{0.25}$ and a-$Li_{3.57}Si_{0.75}Sn_{0.25}$ are computed to be 32.05 ± 0.26 and 19.39 ± 1.59 GPa, respectively, which are compared with the moduli of *a*-LiSi (32.95 ± 1.08 GPa) and *a*-$Li_{3.57}Si$ (21.16 ± 3.93 GPa), respectively. The bulk moduli decrease with increasing Li content leading to significant elastic softening. For a given Li content, the ternary alloy tends to be slightly softer than the binary alloy.

11.4 Summary

Using DFT-GGA and AIMD calculations, we examined the energetics, structure, electronic and mechanical properties of amorphous $Si_{0.75}Sn_{0.25}$ and $Li_xSi_{0.75}Sn_{0.25}$ alloys. The model which is considered as an amorphous semiconductor is well defined by the pair distribution in which the coordination number of Si and Sn are 4 neighbors. In addition, the amorphous $Si_{0.75}Sn_{0.25}$ is predicted to be soft.

The electrochemical experiment showed that the thin $Si_{0.75}Sn_{0.25}$ film remained amorphous phases during lithiation by the evidence of no sharp peak in the differential capacity. The calculated potential vs. composition curve seems to be in good agreement with the experimental result, and all of our data fall within the experimental lithiation/delithiation curve. The agreement with experiment confirms that the amorphous models presented in this study are correctly captured.

According to our mixing enthalpy calculations for *a*-$Li_xSi_{0.75}Sn_{0.25}$ alloys, the favorable alloy formation occurs around 60−80 at. % Li. With increasing Li content, we

find that: i) the tetrahedrally bonded Si network undergoes disintegration into low-connectivity clusters; ii) the *a*-Li-Si-Sn becomes more densely packed as evidenced by the increasing CN; iii) Si-Si PDF peaks shift toward larger *r* values as a result of weakened Si-Si bonds, also Sn-Sn bond length increase. The sparser network of the host matrix at x=1.0, the closer network of host matrix at x=3.57 may enhance the structural stability during lithiation/delithiation.

Our electronic DOS analysis illustrates that towards higher lithiated states, the Si *s*-*p* splitting grows larger accompanied by weakening/breaking of Si-Si bonds (Sn-Sn bonds) and changes in the alloys structure. Due to the softening of Si and Sn network, the bulk modulus decreases almost linearly with increasing Li content. The electronic analysis also reveals the band gap narrowing with increasing degree of lithiation, showing more metallic character. The fundamental findings assist in understanding the nature of Li-Si-Sn alloys further, and the present work can also provide a framework for the study of various lithiated alloys.

CHAPTER 12:
Conclusions and Recommendations for Future Work

12.1 Conclusion

The first part of this thesis covers the formability of amorphous alloys and examined the bulk, surface, and interfaces of the amorphous alloys to provide structural and electronic properties for the applications as microelectronic devices. First, we investigated the formability of amorphous alloys (RuP, RuB, CoP, and CoB) by calculating two quantities, the total energy difference and the mixing enthalpy. The study describes the stability of amorphous alloys compared to the crystalline counterparts and the results are related, where possible to experimental results. The amorphous alloys, RuP, CoP, RuB, and CoB, become energetically more favorable than its crystalline counterpart when the solute content is above 20 at. %, 20 at. %, 10 at. %, and 10 at. %, respectively, meaning that they can retain their amorphous structures at moderate conditions. The forming ability of Ru-based alloys is mainly governed by the elastic atomic size ratio, while that of Co-based alloys is determined by both elastic atomic size ratio and heat of mixing.

Second, we analyzed the atomistic structures of the selected $Ru_{80}P_{20}$, $Co_{80}P_{20}$, $Ru_{87}B_{13}$, $Co_{86}B_{14}$ alloys. Their structures turn out to have well-defined local structures depending on the atomic size ratio and electronic interactions of the host and solutes atoms. The icosahedral ordering as a medium-range order is predicted to be the stable packing in metallic glasses. From the calculated DOS of Ru 4d (Co 3d) and P 3p (B 2p), we can see a high degree of p-d hybridization, which contributes to stabilizing the Ru(Co)-P(B) alloy structure. However, B containing alloys (Ru-B and Co-B) do not have much electronic interaction between the metal and B as a result from the less filled valence electron of B.

Third, we investigated the surface and interface interactions between these alloys and Cu or *a*-SiO_2. The P atom undergoes surface segregation, while the B atom does not in high temperature annealing. A Cu film and monolayer (ML) of Cu on the Ru substrate

are predicted to be wetted well by the thermodynamic stability calculation. The Ru substrate has good adhesion properties with Cu, because Cu and Ru have a strong electronic intermixing to enhance the chemical bonding strength. However, P does not associate with Cu, because P and Cu have a weak electronic intermixing, resulting in degradation of the adhesion strength of two films of RuP/Cu. We also investigated the interaction between *a*-SiO_2 and Ru in terms of adhesion properties and interfacial chemical bonding. At optimum contents of the non-bridging oxygen, Ru has a good adhesion energy with *a*-SiO_2, while, at low contents of non-bridging oxygen at the surface, it has poor adhesion strength. However, if the oxygen is surplus at the interface, the Ru may be oxidized; thus, their adhesion strength may be decreased due to the poor adhesion between oxygen atoms.

The second part of this thesis focused on the Si (Ge, Sn) based anode materials. We examined the structure, stability, diffusion, and bonding mechanism of a single Li interstitial atom in i) *c*-Si in the neutral and positive charge states and ii) *c*-Ge and *c*-Sn in the neutral states. We also looked at the interaction between two Li interstitials and the effect of Li incorporation on the stability of the diamond Si (Ge, Sn) lattice. The tetrahedral (T) state turns out to be energetically most favored. Our result shows that interstitial Li may undergo diffusion with a moderate barrier of ≈ 0.6, 0.44, and 0.39 eV in *c*-Si, *c*-Ge, and *c*-Sn, respectively. We also find that the repulsive interaction between Li^0 interstitials can make Li interstitials isolated, rather than clustered. The incorporation of Li^0 at the T site results in noticeable outward displacement of the four first neighbors, leading to charge localization within the first nearest atoms and weakening of covalent bonds.

We examined the energetics, structure, electronic and mechanical properties of crystalline and amorphous Li-X (X: Si, Ge, and Sn) alloys. According to our mixing energy calculations, the mixing energy decreases in the order of Si (-0.17 eV/atom), Ge (-0.29 eV/atom), and Sn (-0.33 eV/atom), suggesting the incorporation/alloying of Li in Sn is particularly favorable. With increasing Li content, we find that: i) the tetrahedrally bonded Si network undergoes disintegration into low-connectivity clusters of various

shapes; ii) the *a*-Li-Si becomes more densely packed; iii) X-X PDF peaks shift toward larger *r* values as a result of weakened X-X bonds. Bader charge analysis shows that while the charge state of Li remains nearly unchanged around ~ +0.84, that of Si varies significantly from −0.85 to −3.30 depending on the number of M neighbors as can be understood by Zintl rules. Our electronic DOS analysis illustrates that towards higher lithiated states, the Si *s-p* splitting grows larger accompanied by weakening/breaking of X-X bonds and changes in the alloy structure.

The mobility of Li in the different host matrix increases in the order of Si, Ge, and Sn, as the atomic size increase. Due to the softening of Si network, the bulk modulus decreases almost linearly with increasing Li content. The electronic analysis also reveals the band gap narrowing with increasing degree of lithiation, showing more metallic character.

Next, the mixing energy of ternary Li-Si-Sn alloy showed that these alloys are well mixed. The ternary system enhances structural stability during charge/discharge by maintain high Si-Si connectivity at high Li content, and by lowering the Si-Si connectivity at low Li content, which enhances Li mobility. The bulk moduli decrease almost linearly with increasing Li content in the ternary system.

The fundamental findings assist in understanding the dynamic behavior of Li atoms and the nature of their interaction with the host M matrix particularly during the early stages of lithiation and the nature of Li-Si alloys further, and the present work can also provide a framework for the study of various lithiated alloys.

12.2 Future work

In addition to above semiconductor-based alloys, the litihiated alloys including an inactive material (for examples, C, Cu, Co, Pd, Pt, Fe, Ni,…), which stabilizes the connectivity of the host structure during charge/discharge without reaction, will be necessary in order to improve the cycle performance of the LIB. In this thesis, some preliminary progress toward explaining the ternary system is presented. However, understanding of the electronic and magnetic properties of alloys including inactive

materials will be necessary to optimize the electrochemical performance. It is believed that the cycling ability increases as the inactive component increases, while the specific capacity decreases. In order to probe the effective interaction between active and inactive material, a formation energy database is essential as a useful indicator of the magnitude of the effective interactions. The stronger the interaction, the more rapid the drop of specific capacity is likely to be; the weaker the interaction, the more limited the improvement in the cycling performance over the pure active material has been suggested. Based on this analysis, the inactive alloys which have the intermediate interaction with active material should be chosen.

Li ions easily diffuse into the Si matrix thereby weakening the covalent bond, and subsequently disordering the Si network. However, when the Li ion is extracted from the Si matrix, electrochemical cycling appeared to be limited by the difficulty of reincorporating the covalent bond. The electrochemical performance degradation may be strongly related to the covalent bond recovery efficiency during discharge of Li ions. It has been commercially reported that the cobalt (Co) sustained the Sn matrix (in 'Nexelion') with a consistent coordination number of Co around Sn during charge/discharge, suggesting that the consistent structural change will be valuable to optimizing the electrochemical performance [180]. To understand in detail how the broken bonds recover in the semiconductor based alloy, *ab initio* molecular dynamics (AIMD) simulations will be necessary.

In addition to above future work, it is essential to investigate the surface structure and surface segregation phenomenon. Surface segregation describes the deviation of the chemical composition in the near-surface layers, compared to bulk, and plays a technologically important role, as it may strongly influence electrochemical process. Since finely dispersed Li reactive particles may enhance the capacity and cycle performance, it seems like that the Li enrichment at surface, influenced by the surface segregation during thermal treatment, and may become less likely. With higher Li concentration at the surface, Li clustering (Li dendrite) may be possible. To understand this phenomenon, AIMD simulation will be necessary.

References

1. Mattox, D.M., *The Foundations of Vacuum Coating Technology*. 2003, Norwich, N.Y.: Noyes Publications/William Andrew Pub.
2. Rehn, L.E., et al., *Solid-State Amorphization of Zr_3Al: Evidence of an Elastic Instability and First-Order Phase Transformation. Phys. Rev. Lett.*, 1987. **59**: p. 2987-2990.
3. Arminni, A.J., S.N. Bunker, and M.B. Spitzer. *Non-mass-analyzed Ion Implantation Equipment for High Volume Solar Cell Production*. in *Proc. 16th IEEE Photovoltaic Specialists Conference*. 1982. San Diego California.
4. Cahn, R.W., *Physical Metallurgy*. 3rd ed. 1983, B.V.: Elsevier Science Publishers.
5. Suryanarayana, C., *Mechanical alloying and milling. Progress in Materials Science*, 2001. **46**: p. 1-184.
6. Limthongkul, P., et al., *Electrochemically-driven solid-state amorphization in lithium-silicon alloys and implications for lithium storage. Acta. Mate.*, 2003. **51**: p. 1103.
7. Klement, W., R. Willens, and P. Duwez, *Non-crystalline structure in solidified gold-silicon alloys. Nature*, 1960. **187**: p. 869.
8. Smith, T.F. and H.L. Luo, *Superconductivity of lanthanum compounds at zero and high pressure. J. Phys. Chem. Solids*, 1967. **28**: p. 569-576.
9. Inoue, A., et al., *Mg-Cu-Y Amorphous Alloys with High Mechanical Strengths Produced by a Metallic Mold Casting Method.* Materials Transactions, JIM., 1991. **32**: p. 609-616.
10. Zhang, T., A. Inoue, and T. Masumoto, *Amorphous Zr-Al-TM (TM=Co, Ni, Cu) Alloys with Significant Supercooled Liquid Region of Over 100 K.* Mater. Trans. JIM., 1991. **32**: p. 1005-1010.
11. Chen, H.S., *Mater. Sci. Eng.*, 1976. **25**: p. 59.
12. Inoue, A., T. Zhang, and T. Itoi, *New Fe-Co-Ni-Zr-B Amorphous Alloys with Wide Supercooled Liquid Regions and Good Soft Magnetic Properties.* Mater. Trans. JIM, 1997. **38**: p. 359-362.

13. Inoue, A. and K. Hashimoto, *Amorphous and Nano-crystalline Materials*. 2001, Berlin: Springer.
14. Giessen, B.C. *Glass formation diagram: A two-parameter presentation of readily glass forming binary alloy system*. in *4th International Conference on Rapidly Quenched Metals*. 1982. Sendai: The Japan Institute of Metals.
15. Hume-Rothery, W., R.E. Smallman, and C.W. Haworth, *Structure of Metals and Alloys*. 1969, London: Institute of Metals.
16. Miedema, A.R., P.F.d. Chatel, and F.R.d. Boer, *Cohesion in alloys-fundamentals of a semi-empirical model. Physica B*, 1980. **100**: p. 1-28.
17. Inoue, A. and A. Takeuchi, *Recent Progress in bulk metallic glasses.* Mater. Trans. JIM, 2002. **43**: p. 1892-1906.
18. Schwarz, R.B. and W.L. Johnson, *Formation of an Amorphous Alloy by Solid-State Reaction of the Pure Polycrystalline Metals. Phys. Rev. Lett.*, 1983. **51**: p. 415-418.
19. Mihalkovic, M. and M. Widom, *Ab initio calculations of cohesive enengies of Fe-based glass-forming alloys. Phys. Rev. B*, 2004. **70**: p. 144107.
20. Zhou, S.H. and R.E. Napolitano, *Phase equilibria and thermodynamic limits for partitionless crystallization in the Al-La binary system. Acta. Materialia*, 2006. **54**: p. 831-840.
21. Kresse, G. and J. Hafner, *Ab initio molecular dynamics for liquid metals. Phys. Rev. B*, 1993. **47**: p. 558-561.
22. Chai, J.-D., et al., *Dynamic structure factor of liquid and amorphous Ge from ab initio. Phys. Rev. B*, 2003. **67**: p. 104205.
23. Egami, T. and S. Aur, *Local atomic structure of amorphous and crystalline alloys: Computer simulation. J. Non-Cryst. Solids*, 1987. **89**: p. 60-74.
24. Wang, Q., et al., *Low-temperature chemical vapor deposition and scaling limit of ultrathin Ru films. Appl. Phys. Lett.*, 2004. **84**: p. 1380.
25. Shin, J., et al., *Chemical vapor deposition of amorphous ruthenium-phosphorus alloy films. Thin Solid films*, 2007. **515**: p. 5298.

26. Henderson, L.B. and J.G. Ekerdt, *Time-to-failure analysis of 5nm amorphous Ru(P) as a copper diffusion barrier. Thin Solid films*, 2009. **517**: p. 1645-1649.
27. Henderson, L.B. and J.G. Ekerdt, *Chemical Vapor Deposition of Amorphous Cobalt-Phosphorus Alloy Films. J. Electrochem. Solid-State Lett.*, 2009. **12(5)**: p. D36-D38.
28. Henderson, L.B. and J.G. Ekerdt, *Effect of Phosphorus and Carbon Incorporation in Amorphous Cobalt Films Prepared by Chemical Vapor Deposition. J. Electrochem. Soc.*, 2010. **157(1)**: p. D29-D34.
29. Winter, M. and J.O. Besenhard, *Electrochemical lithiation of tin and tin-based intermetallics and composites. Electrochim. Acta*, 1999. **45**: p. 31.
30. Sharma, R.A. and R.N. Seefurth, *Thermodynamic Properties of the Lithium-Silicon System. J. Electrochem. Soc.*, 1976. **123**: p. 1763.
31. Boukamp, B.A., G.C. Lesh, and R.A. Huggins, *All-Solid Lithium Electrodes with Mixed-Conductor Matrix. J. Electrochem. Soc.*, 1981. **128**: p. 725.
32. Beaulieu, L.Y., et al., *Colossal Reversible Volume Changes in Lithium Alloys. J. Electrochem. Solid-State Lett.*, 2001. **4**: p. A137.
33. Ryu, J.H., et al., *Failure Modes of Silicon Powder Negative Electrode in Lithium Secondary Batteries. Electrochem. Solid-State Lett.*, 2004. **7**: p. A306.
34. Obrovac, M.N. and L. Christensen, *Structural Changes in Silicon Anodes during Lithium Insertion/Extraction. Electrochem. Solid-State Lett.*, 2004. **7**: p. A93.
35. Maranchi, J.P., A.F. Hepp, and P.N. Kumta, *High Capacity, Reversible Silicon Thin Film Anodes for Lithium-Ion Batteries. Electrochem. Solid-State Lett.*, 2003. **6**: p. A198.
36. Netz, A., R.A. Huggins, and W. Weppner, *The formation and properties of amorphous silicon as negative electrode reactant in lithium systems. J. Power Sources*, 2003. **95**: p. 119-121.
37. Bourderau, S., T. Brousse, and D.M. Schleich, *Amorphous silicon as a possible anode material for Li-ion batteries. J. Power Sources*, 1999. **223**: p. 81-82.

38. Gao, B., et al., *Alloy Formation in Nanostuructured Silicon. Adv. Mater.*, 2001. **13**: p. 816.
39. Gratetz, J., et al., *Highly Reversibe Lithium Storage in Nanostructured Silicon. Electrochem. Solid-State Lett.*, 2003. **6**: p. A194.
40. Chan, C.K., et al., *High-performance lithium battery anodes using silicon nanawires. Nat. Nanotechnol.*, 2008. **3**: p. 31.
41. Beaulieu, L.Y., et al., *The Electrochemical Reaction of Li with Amorphous Si-Sn Alloys. J. Electrochem. Soc.*, 2003. **150**: p. A149.
42. Mao, O., et al., *Active/Inactive Nanocomposites as Anodes for Li-Ion Batteries. Electrochem. Solid-State Lett.*, 1999. **2**: p. 3.
43. Fleischauer, M.D., J.M. Topple, and J.R. Dahn, *Combinational Investigations of Si-M (M=Cr+Ni, Fe, Mn) Thin Film Negative Electrode Materials. Electrochem. Solid-State Lett.*, 2005. **8**: p. A1457.
44. Beaulieu, L.Y., et al., *Reaction of Li with Alloy Thin Films Studied by In Situ AFM. J. Electrochem. Soc.*, 2003. **150**: p. A1457.
45. Nazri, G.A. and G. Pistoia, *Lithium Batteries: Science and Technology*. 2004, Boston: Kluwer Academic Plenum.
46. Anani, A., S. Crouch-Baker, and R.A. Huggins, *Kinetic and Thermodynamic Parameter of Several Binary Lithium Alloy Negative Electrode Materials at Ambient Temperature. J. Electrochem. Soc.*, 1987. **134**: p. 3098.
47. Anantharaman, T.R., *Metallic glasses: production properties and applications*. 1984: Trans Tech Publications.
48. Massalski, T.B. and H. Okamoto, *Binary Alloys Phase Diagrams*. 1990: ASM International.
49. Stearns, L.A., et al., *Lithium monosilicide (LiSi), a low-dimensional silicon-based material prepared by high pressure synthesis: NMR and vibrational spectroscopy and electrical properties characterization. J. Solid State Chem.*, 2003. **173**: p. 251.
50. Kubota, Y., et al., *Crystal and Electronic Structure of $Li_{15}Si_4$. J. Appl. Phys.*, 2007. **102**: p. 053704.

51. Kubota, Y., et al., *Electronic structure of LiSi. J. Alloys and Compounds*, 2008. **458**: p. 151.
52. Leuken, H.v., G.A.d. Wijs, and W.v.d. Lugt, *Electronic structure of $Li_{12}Si_7$. Phys. Rev. B*, 1996. **53**: p. 10599.
53. Chevrier, V.L. and J.R. Dahn, *First Principles Studies of Disordered Lithiated Silicon. J. Electrochem. Soc.*, 2010. **157(4)**: p. A392-A398.
54. Chevrier, V.L. and J.R. Dahn, *First principles model of amorphous silicon lithiation. J. Electrochem. Soc.*, 2009. **156(6)**: p. A454-A458.
55. Finney, J.L., *Random Packings and the Structure of Simple Liquids. II. The Molecular Geometry of Simple Liquids. Proc. R. Soc.*, 1970. **319**: p. 495-507.
56. Finney, J.L., *Modeling the structures of amorphous metals and alloys. Nature*, 1977. **266**: p. 309-314.
57. Hohenberg, P. and W. Kohn, *Inhomogeneous Electron Gas. Phys. Rev. B*, 1964. **864**: p. 136.
58. Kohn, W. and L.J. Sham, *Self-consistent equations including exchange and correlation effects. Phys. Rev.*, 1965. **140(4A)**: p. 1133A-1138A.
59. Hafner, J., *Atomic-scale computational materials science. Acta. Materialia*, 2000. **48(1)**: p. 71.
60. Ceperley, D.M. and B.J. Alder, *Ground-state of the electron-gas by a stochastic method. Phys. Rev. Lett.*, 1980. **45**: p. 566.
61. Perdew, J.P., et al., *Atoms, molecules, solids, and surfaces applications of the generalized gradient approximation for exchange and correlation. Phys. Rev. B*, 1992. **46**: p. 6671.
62. Parrinello, M., *From Silicon to RNA: The Coming of Age of Ab Initio Molecular Dynamics. Solid State Comm.*, 1997. **102**: p. 107.
63. Perdew, J.P., K. Burke, and M. Ernzerhof, *Generalized gradient approximation made simple. Phys. Rev. Lett.*, 1996. **77**: p. 3865.
64. Vanderbilt, D., *Soft self-consistent pseudopotentials in generalized eigenvalue formalism. Phys. Rev. B*, 1990. **41**: p. 7892.

65. Blochl, P.E., *Projector augmented-wave method. Phys. Rev. B*, 1994. **50**: p. 17953.
66. Kresse, G. and J. Furthmuller, *Efficiency of ab-initio total energy calculations for metals and semiconductors using a plane-wave basis set. J. Comput. Mater. Sci.*, 1996. **6**: p. 15-50.
67. Kresse, G., *Efficient iterative schemes for ab initio total-energy calculations using a plane-wave basis set. Phys. Rev. B*, 1996. **54**: p. 11169-11186.
68. Payne, M.C., et al., *Iterative minimization techniques for ab initio total-energy calculations: molecular dynamics and conjugate gradient. Rev. Mod. Phys.*, 1992. **64**: p. 1045.
69. Allen, M.P. and D.J. Tildesley, *Computer Simulations of Liquids*. 1990, Oxford: Clarendon Press.
70. Henkelman, G., G. Johannesson, and J. Jonsson, *Methods for finding saddle points and minimum energy paths*, ed. S.D. Schwartz. 2000: Kluwer Academic Publishers. 269-300.
71. Henkelman, G., B.P. Uberuaga, and H. Jonsson, *A climbing image nudged elastic band method for finding saddle points and minimum energy paths. J. Chem. Phys.*, 2000. **113**: p. 9901.
72. Henkelman, G., A. Arnaldsson, and H. Jonsson, *A fast and robust algorithm for Bader decomposition of charge density. Comp. Mater. Sci*, 2006. **36**: p. 354-360.
73. Murnaghan, F.D., *The Compressibility of Media under Extreme Pressure. Proceedings of the National Academy of Sciences*, 1944. **30**: p. 244-247.
74. Bernal, J.D., *The Bakerian Lecture, 1962. The Structure of Liquids. Proc. R. Soc. A*, 1964. **280**: p. 299.
75. Lamparter, P., *Reverse monte carlo simulation of amorphous $Ni_{80}P_{20}$ and $Ni_{81}P_{19}$. Phys. Scr.*, 1995. **T57**: p. 72.
76. Sheng, H.W., et al., *Atomic packing and short-to-medium-range order in metallic glasses. Nature*, 2006. **439**: p. 419.
77. Rundqvist, S., *Phosphides of platinum metals. Nature*, 1960. **185**: p. 31.

78. Rundqvist, S., *Phosphides of the B2/(MnP) structure type. Acta Chem. Scand.*, 1962. **16**: p. 287.
79. Holseth, H. and A. Kjejsgys, *Compounds with Marcasite type crystal structure II, On the crystal structures of the binary pnictides. Acta Chem. Scand.*, 1968. **22**: p. 3284.
80. *Internal Tables for X-ray Crystallography*. 1968, Birmingham, England.
81. Daams, J.L.C., P. Villars, and J.H.N.v. Vucht, *Atlas of Crystal Structure Types for Intermetallic Phases*, in *ASM International*. 1991, Materials Park: OH.
82. Winter, M., *WebElements Periodic Table*. 2000, University of Sheffield: UK. p. http://www.webelements.com.
83. Allen, M. and D. Tildesley, *Computer simulation of liquids*. 1987, New York: Oxford University Press. 54.
84. Lee, S.-H. and G.S. Hwang, *Structure, energetics, and bonding of amorphous Au-Si alloys. J. Chem. Phys.*, 2007. **127**: p. 224710.
85. Gaskell, P.H., *Amorphous Metals*, ed. H.M.a.P.G. Zielinski. 1985, Singapore: World Scientific Publishing.
86. Luo, W.K., et al., *Icosahedral Short-Range Order in Amorphous Alloys. Phys. Rev. Lett.*, 2004. **92**: p. 145502.
87. Ruban, A.V., H.L. Skriver, and J.K. Norskov, *Surface segregation energies in transition-metal alloys. Phys. Rev. B*, 1999. **59**: p. 15990-16000.
88. Christensen, A., et al., *Phase diagrams for surface alloys. Phys. Rev. B*, 1997. **56**: p. 5822.
89. Kaloyerlos, A., et al., *Tantalum Nitride Films Grown by Inorganic Low Temperature Thermal Chemical Vapor Deposition Diffusion Barrier Properties in Copper Metallization. J. Electrochem. Soc.*, 1999. **146**: p. 170.
90. *International Technology Roadmap for Semiconductors*. 2006. http://public.itrs.net.

91. Kim, H., *Atomic layer deposition of metal and nitride thin films: Current research efforts and applications for semiconductor device processing. J. Vac. Sci. Technol B,* 2003. **21**: p. 1622676.
92. Shin, J., et al., *Effects of P on amorphous chemical vapor deposition Ru-P alloy films for Cu interconnect liner applications. J. Vac. Sci. Technol A*, 2008. **26**: p. 974.
93. Kittel, C., *Introduction to Silid State Physics*. 8th ed. 2005, New York: John Wiley & Sons, Inc.
94. Kim, H., et al., *The physical properties of cubic plasma-enhanced atomic layer deposition TaN films. J. Appl. Phys.*, 2004. **95**: p. 5848.
95. Birkholz, M., et al., *Amorphous-crystalline phase transition during the growth of thin films: The case of mocrocrystalline silicon. Phys. Rev. B*, 2001. **64**: p. 085402.
96. Finnis, M.W., *The Thoery of metal-ceramic interface. J. Phys. Condens. Matter*, 1996. **8**: p. 5811-5836.
97. Freund, L.B. and S. Suresh, *Thin Film Materials: Stress, Defect Formation and Surface Evolution.* 2003, Cambridge, England: Cambridge University Press.
98. Vitos, L., et al., *The surface energy of metals. Surf. Sci.*, 1998. **411**(1-2): p. 186-202.
99. Chou, M.Y. and J.R. Chelikowsky, *Structural properties of the Ru(0001) surface. Phys. Rev. B,* 1987. **35**: p. 2124-2127.
100. Lin, J. and C. Lee, *Grain Boundary Diffusion of Copper in Tantalum Nitride Thin Films. J. Electrochem. Soc.*, 1999.
101. Wang, H., et al., *Copper diffusion characteristics in single-crystal and polycrystalline TaN. Appl. Phys. Lett.*, 2002. **81**: p. 1453.
102. Oku, T., et al., *Diffusion barrier property of TaN between Si and Cu. Appl. Surf. Sci.*, 1996. **99**: p. 265.
103. Figuera, J.d.l., et al., *Determination of buried dislocation structures by scanning tunneling. Phys. Rev. B*, 2001. **63**: p. 165431.

104. Hashibon, A., et al., *First-principles study of thermodynamical and mechanical stabilities of thin copper film on tantalum. Phys. Rev. B,* 2007. **76**: p. 245434.
105. Shin, J., et al., *Growth of Ultrathin Films of Amorphous Ruthenium-Phosphorus Alloys Using a Single Source CVD Precusor. J. Am. Chem. Soc,* 2006. **128(51)**: p. 16510-16511.
106. Nagao, K., J.B. Neaton, and N.W. Ashcroft, *First-principles study of adhesion at Cu/SiO_2 interfaces. Phys. Rev. B*, 2003. **68**: p. 125403.
107. Jiang, D.E. and E.A. Carter, *First-principles study of the interfacial adhesion between SiO_2 and $MoSi_2$. Phys. Rev. B,* 2005. **72**: p. 165410.
108. Molodtsov, S.L., et al., *Formation and chemical structure of the Au/Si(111) interface. Phys. Rev. B*, 1991. **44**: p. 8850-8857.
109. Hannon, J.B., et al., *The influence of the surface migration of gold on the growth of silicon nanowires. Nature*, 2006. **440**: p. 69-71.
110. Zhuravlev, L.T., *Concentration of hydroxyl group on the surface of amorphous silicas. Langmuir*, 1987. **3(3)**: p. 316-318.
111. Monkhorst, H.J. and J.D. Pack, *Special points for Brillouin-zone integrations. Phys. Rev. B,* 1976. **13**: p. 5188-5192.
112. Johnson, P.A.V., A.C. Wright, and R.N. Sinclair, *Neutron scattering from vitreous silica II. Twin-axis diffraction experiments. J. Non-Cryst. Solids*, 1983. **58**: p. 109-130.
113. Sarnthein, J., A. Pasquarello, and R. Car, *Structural and Electronic Properties of Liquid and Amorphous SiO_2: An Ab initio Molecular Dynamics Study. Phys. Rev. Lett.*, 1995. **74**: p. 4682-4685.
114. Singer, P., *Semocond. Int.* 2005. p. 44.
115. Born, B. and R. Oppenheimer, *On the Quantum Theory of Molecules. Ann. Phys.*, 1927. **84**: p. 457.
116. Rundqvist, S., *Crystal structure of Ni_2B and Co_3B. Acta Chem. Scand.*, 1958. **12**: p. 658.

117. Kiessling, R., *The Borides of some transition elements. J. Electrochem. Soc.*, 1951. **98(4)**: p. 166-170.
118. Nishizawa, T. and K. Ishida, *Properties of Cobalt. Bull. Alloy Phase Diagrams*, 1983. **4(4)**: p. 414-420.
119. Selte, K. and A. Kjekshus, *On phase Transitions Between the MnP and NiAs Type Structures. Acta Chem. Scand.*, 1973. **27**: p. 3195-3206.
120. Rundqvist, S., *The Structures of Co_2P, Ru_2P, and Related Phases. Acta Chem.Scand.*, 1960. **14**: p. 1961-1979.
121. Rundqvist, S. and N. Ersson, *Structure and bonding in Skutterudite-type Phosphides. Ark. Kemi.*, 1968. **30**: p. 103-114.
122. Modak, P., et al., *Ab initio total-energy and phonon calculations of Co at high pressures. Phys. Rev. B*, 2006. **74**: p. 012103.
123. Donahue, J., *The Structures of the Elememts*. 1974, New York: Wiley.
124. Crangle, J., *Philos. Mag.*, 1955. **46**: p. 499.
125. Strauss, B., et al., *Martensitic phase transformation and lattice dynamics of fcc cobalt. Phys. Rev. B*, 1996. **54**: p. 6035.
126. Shin, J., et al., *Chemical routes to ultra thin films for copper barriers and liners. Surf. & Coat. Tech.*, 2007. **201**: p. 9256-9259.
127. Cargill, G.S. and R.W. Cochran, *Amorphous Cobalt-Phosphorus Alloys: Atomic Arrangements and Magnetic Properties. J. Phys. (Paris)*, 1974. **35(C4)**: p. 269-278.
128. Lamparter, P., E. Nold, and H. Rainer, *X-ray and neutron diffraction studies on amorphous transition metal-boron alloys (Fe-B, Co-B, Ni-B). Z. Naturforsch*, 1981. **A36**(2): p. 165-171.
129. Sharma, N.D. and F.A. Kasir, *Energy of Migration of Cation Vacancies in Cesium Chloride Type Crystals. J. Phys. Soc. Jpn.*, 1979. **47**(3): p. 1025-1026.
130. Hatchard, T.D. and J.R. Dahn, *In Situ XRD and Electrochemical Study of the Reaction of Lithium with Amorphous Silicon. J. Electrochem. Soc.*, 2004. **151**: p. A838.

131. Kresse, G. and J. furthmuller, VASP the guide (Vienna University of Technology, Vienna, Austria), 2001.
132. Makov, G. and M.C. Payne, *Periodic boundary conditions in ab initio calculations. Phys. Rev. B*, 1995. **51**: p. 4014.
133. Aggarwal, R.L., et al., *Excitation Spectra of Lithium Donors in Silicon and Germanium. Phys. Rev.*, 1965. **138**: p. A882.
134. Milman, V., et al., *Free energy and entropy of diffusion by ab initio molecular dynamics: Alkali ions in silicon. Phys. Rev. Lett.*, 1993. **70**: p. 2928.
135. Weiser, K., *Theory of Diffusion and Equilibrium Position of Interstitial Impurities in the Diamond Lattice. Phys. Rev.*, 1962. **126**: p. 1427.
136. Harding, J.H., *Computer simulation of defects in ionic solids. Rep. Prog. Phys.*, 1990. **53**: p. 1403.
137. Canham, L.T., *Properties of silicon, Electronic Materials Information Service (EMIS)*, K.V. Ravi, et al., Editors. 1988, INSPEC: London.
138. Ashcroft, N.W. and N.D. Mermin, *Solid State Physics*. 1976, Harcourt: Orlando.
139. Bohm, M.C., et al., *Tight-binding approach to the solid-state structure of the complex Zintl-phase $Li_{12}Si_7$. Phys. Rev. B*, 1984. **30**: p. 4870.
140. Schnering, H.G.v., et al., *$Li_{14}Si_6$. Z. Metallkd*, 1980. **71**: p. 357 (in German).
141. Frank, U., W. Muller, and H. Schafer, *Die Kristallstruktur der Phase Li_7Sn_2. Z. Naturforsch. B*, 1975. **30**: p. 6-9.
142. Nesper, R. and H.G.v. Schnering, *$Li_{21}Si_5$. a Zintl Phase as Well as a Hume-Rothery Phase. J. Solid State Chem.*, 1987. **70**: p. 48-57.
143. Kim, H., et al., *On the Nature of Behavior of Li Atoms in Si: A First Principles Study. J. Phys. Chem. C*, 2010. **114(41)**: p. 17942-17946.
144. Wijs, G.A.d., et al., *First-principles molecular-dynamics simulation of liquid $Li_{12}Si_7$. Phys. Rev. B*, 1993. **48**: p. 13459-13468.
145. Murday, J.S. and R.M. Cotts, *Z. Naturforsch*, 1971. **A26**: p. 85.
146. Sanders, P.G. and M.J. Aziz, *Self-diffusivity of liquid silicon measured by pulsed laser melting. J. Appl. Phys.*, 1999. **86**: p. 4258.

147. Yang, S., et al., *Molecular Dynamics Analysis of Temperature Dependence of Liquid Metal Diffusivity. Metallurgical and mateials transactions A*, 2009. **40A**: p. 3108-3116.

148. Cohen, M.H. and D. Turnbull, *Molecular Transport in Liquids and Glasses. J. Chem. Phys.*, 1959. **31**: p. 1164.

149. Ercolessi, F., E. Tosatti, and M. Parrinello, *Au(100) Surface Reconstruction. Phys. Rev. Lett.*, 1986. **57**: p. 719-722.

150. Lopez, M.J. and J. Jellinek, *Fragmentation of atomic clusters: A theoretical study. Phys. Rev. A*, 1994. **50**: p. 1445-1458.

151. Liu, C.S., et al., *The cooling rate dependence of crystallization for liquid copper: A molecular dynamics study. J. Chem. Phys.*, 2001. **114**: p. 7506.

152. Willaime, F. and C. Massobrio, *Temperature-induced hcp-bcc phase transformation in zirconium: A lattice and molecular-dynamics study based on an N-body potential. Phys. Rev. Lett.*, 1989. **63**: p. 2244-2247.

153. Thompson, M.O., et al., *Melting Temperature and Explosive Crystallization of Amorphous Silicon during Pulsed Laser Irradiation. Phys. Rev. Lett.*, 1984. **52**: p. 2360-2363.

154. *The activated state model[47]: $D \sim \exp(-1/T)$; moving oscillator model[48]: $D \sim T$; density fluctuation model [49]: $D \sim T^2$; free volume model[50]: $D \sim T^{1/2}\exp(-1/T)$. From these models, the Li (Si) self-diffusion coefficients at 1,050K were estimated to be $0.65(4.00) \times 10^{-4}$, $1.45(2.49) \times 10^{-4}$, $3.24(1.55) \times 10^{-4}$ and $0.97(3.15) \times 10^{-4}$ cm^2/sec, respectively..*

155. Kauzlarich, S.M., *Chemistry, Structure, and Bonding of Zintl Phase and Ions*. 1996, New York: Wiley-VCH Publishers.

156. Asher, J., et al., *Kaye & Laby's Tables of Physical and Chemical Consants*. 16 ed. Vol. 45. 1995, Harlow, Essex: Longman.

157. Simmons, G. and H. Wang, *Single Crystal Elastic Constants and Calculated Aggregate Properties: A Handbook*. 1971, Cambridge, MA: MIT Press.

158. Bondi, R.J., S. Lee, and G.S. Hwang, *First-principles study of the mechanical and optical properties of amorphous hydrogenated silicon and silicon-rich silicon oxide. Phys. Rev. B,* 2010. **81**: p. 195207.

159. Hatchard, T.D. and J.R. Dahn, *Study of the Electrochemical Performance of Sputtered $Si_{1-x}Sn_x$ Films. J. Electrochem. Soc.*, 2004. **151(10)**: p. A1628-A1635.

160. Li, J., et al., *In Situ ^{119}Sn Mossbauer Effect Study of the Reaction of Lithium with Si Using a Sn Probe. J. Electrochem. Soc.*, 2009. **156(4)**: p. A283-A288.

161. Baker, J.F.C. and M. Hart, *An absolute measurement of the lattice parameter of germanium using multiple-beam X-ray diffractometry. Acta Cryst.*, 1975. **A31**: p. 364-367.

162. Menges, E., et al., *Die Kristallstruktur von LiGe-einneuartiger, Dreidmensionaler Verband von Element (IV)-atomen. Z. Naturforsch. B,* 1969. **24**: p. 1351-1352.

163. Hopf, V., W. Muller, and H. Schafer, *Die Struktur der Phase Li_7Ge_2. Z. Naturforsch. B,* 1972. **27**: p. 1157-1160.

164. Johnson, Q., G.S. Smith, and D. Wood, *The crystal structure of $Li_{15}Ge_5$. Acta Cryst.*, 1965. **18**: p. 131-132.

165. Goward, G.R., et al., *The true crystal structure of $Li_{17}M_4$(M=Ge, Sn, Pb)-revised from $Li_{22}M_5$. J. Alloys and Compounds,* 2001. **329**: p. 82-91.

166. Muller, W. and H. Schafer, *Die Kristallstruktur der Phase LiSn. Z. Naturforsch. B,* 1973. **25**: p. 2392-2395.

167. Muller, W., *Darstellung und Struktur der Phase Li_7Sn_3. Z. Naturforsch. B,* 1974. **29**: p. 304-307.

168. Frank, U., W. Muller, and H. Schafer, *Darstellung und Strucktur der Phase Li13Sn5 und die strukturelle Verwandtschaft der Phasen in den System Li-Sn und Li-Pb. Z. Naturforsch. B,* 1975. **30**: p. 316-322.

169. Lupu, C., et al., *X-ray and Neutron Diffraction Studies on $Li_{4.4}Sn$. Inorg. Chem.*, 2003. **42**: p. 3765-3771.

170. Tsukeva, E.A., et al., *On the possibility to grow thin tin films with unusual tin structures from the vapor. Z. Kristallorg,* 1989. **187**: p. 63-70.

171. Hansen, D.A. and L.J. Chang, *Crystal Structure of Li_2Sn_5. Acta Cryst.*, 1969. **B25**: p. 2392-2395.

172. Xia, L., et al., *Thermodynamic modeling of glass formation in metallic glasses. Appl. Phys. Lett.*, 2006. **88**: p. 171905.

173. Landau, L.D. and E.M. Lifshitz, *Theory of Elasticity*. 3rd ed. 1999, Oxford: Butterworth Heinemann.

174. Maruyama, T. and H. Akagi, *Thin Films of Amorphous Silicon-Tin alloy Prepared by Radio-Frequency Magnetron Sputtering. J. Electrochem. Soc.*, 1997. **144**: p. 4350.

175. Thrope, M.F. and E.J. Garboczi, *Elastic Properties of Central-Force Networks with Bond-Length Mismatch. Phys. Rev. B*, 1990. **42**: p. 8405-8417.

176. Cai, Y. and M.F. Thrope, *Length mismatch in random semiconductor allyos. I. General theory for quaternaries. Phys. Rev. B*, 1992. **46**: p. 15872.

177. Reimers, J.N. and J.R. Dahn, *Application of ab initio methods for calculations of voltage as a function of composition in electrochemical cells. Phys. Rev. B*, 1993. **47**: p. 2995-3000.

178. Aydinol, M.K., A.F. Kohan, and G. Ceder, *Ab initio study of lithium intercalation in metal oxides and metal dichalcogenides. Phys. Rev. B*, 1997. **56**: p. 1354.

179. Mehl, M.J., B.M. Klein, and D.A. Papaconstantopoulos, *Intermetallic Compounds: Principles and Practice.*
First principles calculations of elastic properties of metals, ed. J.H. Westbrook and R.L. Fleischer. 1993, London: John Wiley and Sons.

180. Inoue, H., et al., *High Capacity Negative Electrode Materials for Nexelion, the new type of Li-ion battery*. ECS 214th meeting, 2008. Abstract #1160.

Vita

Hyun Woo Kim was born to Insub Kim and Minja Choi in Korea in 1970. He received a B.S. degree in Chemical Engineering from Dongguk University, Seoul, Korea. He received a M.S. degree under the supervision of Dr. Chang Kyun Choi in Chemical Engineering from Seoul National University in 1998. His graduate work focused on Modeling Membrane filteration in a Taylor-Vortex flow. From 1998-2005, he worked at KCC, Korea, developing Direct Synthesis for Methylchlorosilanes. In 2006, he began his graduate studies under the fellowship from KCC at the University of Texas at Austin, with Dr. John G. Ekerdt and Dr. Gyeong S. Hwang.

Permanent address (email): 134-782, Samic APT 501-1507, Myeongil-dong, Gangdong-gu, Seoul, South Korea (khwoolms@gmail.com)

This dissertation was typed by Hyun Woo Kim.